

COMPUTATIONALLY PROBING THE CYBOTACTIC REGION IN GAS-
EXPANDED LIQUIDS

A Thesis
Presented To
The Academic Faculty

By

Charu Lata Shukla

In Partial Fulfillment
Of the Requirements for the Degree
Doctor of Philosophy in Chemical Engineering

Georgia Institute of Technology
May 2007

COMPUTATIONALLY PROBING THE CYBOTACTIC REGION IN GAS-
EXPANDED LIQUIDS

Approved by:

Dr. Charles A. Eckert
School of Chemical and Biomolecular
Engineering
Georgia Institute of Technology

Dr. Charles L. Liotta
School of Chemistry and Biochemistry
Georgia Institute of Technology

Dr. Rigoberto Hernandez
School of Chemistry and Biochemistry
Georgia Institute of Technology

Dr. Martha Gallivan
School of Chemical and Biomolecular
Engineering
Georgia Institute of Technology

Dr. Carson Meredith
School of Chemical and Biomolecular
Engineering
Georgia Institute of Technology

Date Approved: December 11, 2006

For my late grandfather, whom I never met

Satisfaction of one's curiosity is one of the greatest sources of happiness in life.

- Linus Pauling

ACKNOWLEDGEMENTS

I first wish to thank Dr. Eckert for his guidance and support. What I appreciate most about him is his kindness and compassion towards his students - myself included. I have learned a great deal about engineering, chemistry, politics, leadership, etc. etc. under him. I hold a great deal of respect for him, and I will always strive to be like him.

I'd like to thank Dr. Rigoberto Hernandez for his guidance and support. What I appreciate most about him is his innovation and drive. He always looks forward for the next best thing, and his enthusiasm is infectious. I'd like to thank Dr. Liotta, a walking chemistry encyclopedia. I am amazed how he can be a vice-provost and then immediately switch hats to become a synthetic chemist or an engineer. His presence of mind is formidable, and he is one of the most charming people I've ever met.

I'd like to thank my committee members Dr. Carson Meredith and Dr. Martha Gallivan for helpful and informative discussions. From Dr. Hernandez's lab, I'd like to thank Jeremy Moix, who has helped me tremendously over the last four years, but particularly in the time-dependent sections of Chapter 2 and 4. I'd like to thank Dr. Alexander Popov, whom I admire greatly, for his guidance on Chapter 2. He is a true scientist. All of the members of Dr. Hernandez's lab – Yanping, Jeremy, Ashley, and Gungor – have been very helpful and fun to be around. I'd also like to thank Ashley Ringer for supplying some Q-Chem DFT results.

I have been blessed with the best office-mates throughout the years: first with Josh Aronson and Don Taylor, who amused me greatly with their clever repartee. My current office-mates, Hillary Huttenhower and Kristen Kitagawa, are such a joy to be around, that they make me look forward to coming to work – even on Monday mornings.

I'd like to thank the whole of the Eckert/Liotta group, some of the best people I have ever met. I'd especially like to thank Jason Hallett for his guidance, patience, and friendship. I'd like to thank Pamela Pollet for answering all of my chemistry-related questions and in particular, performing the SPARTAN calculations in Chapter 3. I'd also like to thank Julie Xie for guiding me in the pyrene chapter, trying to bridge the synergy of theory and experiment. I'd like to thank Liz Hill, Malina Janakat, and Johnny Gohres, all of whom helped me in times of need.

There have been several outside friends I'd like to thank: Vivek Kaul, Anuradha Kaanan, and Vidasara Roy for showing me a higher path in life and introducing me to the beauty of yoga. I'd like to thank Suchitra Konduri and Hema Patel for their support and friendship. Though seemingly strange, I'd like to thank Madonna Louise Veronica Ciccone, the musician. I have spent many-a-sleepless night with her music playing, and she has always been an inspiration to me. She fuels my desire to learn, grow, and work hard.

I'd like to thank my father, mother, and my brother, Siddhartha, without whom none of this would've have been possible. They have always believed in me, and I have no way to repay them for their love. I'd finally like to thank my husband, Pavan, for his love, support, and kindness towards me. He has been very patient with me and has proofread this entire thesis. He, too, has always believed in me.

TABLE OF CONTENTS

ACKNOWLEDGEMENTS	iv
LIST OF TABLES	viii
LIST OF FIGURES	ix
LIST OF ABBREVIATIONS	xiii
SUMMARY	xv
CHAPTER I.	INTRODUCTION: GAS-EXPANDED LIQUIDS AND MOLECULAR DYNAMICS SIMULATIONS
	Introduction 1
	Gas-Expanded Liquids 3
	The Cybotactic Region 7
	Phenanthrene solubility in GXLs “catalyzes” MD studies 9
	Experimental Probes of the Cybotactic Region 11
	Computer Simulations as a Probe 15
	Conclusions 22
	References 24
CHAPTER II.	MOLECULAR-DYNAMICS SIMULATIONS OF CO ₂ -EXPANDED METHANOL AND CO ₂ -EXPANDED ACETONE
	Introduction 27
	Choosing a Suitable Force Field
	TrAPPE Potential for CO ₂ 33
	J2 Potential for Methanol 33
	OPLS Potential for Acetone 34
	Justification for Choice of Force 35
	Cross-Interaction terms 35
	Simulation Details 37
	Testing the Force Field and Stability of the System
	Testing for Convergence in NVT 41
	Pressure Studies 44
	Flexible model simulations 46
	Structural Results
	CO ₂ -CO ₂ interactions 48
	MeOH-MeOH interactions 49
	Acetone-acetone interactions 50
	Carbon Dioxide Interactions with Solvent 58

	Local Number Density Calculations	60
	Time-Dependent Results	
	Diffusion coefficients	63
	Local Density Autocorrelation Functions	67
	Conclusions	71
	References	72
CHAPTER III.	MOLECULAR DYNAMICS SIMULATIONS OF PYRENE IN CO ₂ -EXPANDED METHANOL AND CO ₂ -EXPANDED ACETONE	
	Introduction	74
	Pyrene Simulations in the Literature	75
	Force Fields	76
	Simulation Details	82
	Results	
	Experimental Results	84
	Simulation results in supercritical CO ₂	88
	Simulation results in pyrene-CO ₂ -MeOH	90
	Simulation results in pyrene-CO ₂ -Acetone	101
	Discussion	107
	Conclusions	111
	References	113
CHAPTER IV.	DIFFUSION COEFFICIENTS OF HETEROCYCLIC COMPOUNDS IN CO ₂ -EXPANDED METHANOL: SYNERGY OF THEORY AND EXPERIMENT	
	Introduction	115
	Description of the Taylor-Aris Dispersion Technique	117
	Simulation Details	119
	Results	
	Diffusion coefficients	122
	Local structure	127
	Conclusions	133
	References	134
CHAPTER V.	RECOMMENDATIONS	136
APPENDIX A		148
APPENDIX B		162
VITA		171

LIST OF TABLES

Table 2-1. Kamlet-Taft parameters of methanol, acetone, and CO ₂	29
Table 2-2. Carbon dioxide parameters from TrAPPE potential	32
Table 2-3. Methanol parameters from J2 potential	32
Table 2-4. Acetone parameters from OPLS-derived potential	32
Table 2-5. Solvent conditions used for simulations	39
Table 2-6. Convergence of simulated pressures for CO ₂ -MeOH simulations	45
Table 2-7. Convergence of simulated pressures for CO ₂ -Acetone simulations	45
Table 2-8. Simulated system pressures of pure methanol	45
Table 2-9. Local Number Density Enhancements in CO ₂ -expanded methanol	62
Table 2-10. Local Number Density Enhancements in CO ₂ -expanded acetone	62
Table 2-11. Instantaneous and steady state time constants from correlation functions	70
Table 3-1. Results of ab initio calculations performed on pyrene	81
Table 3-2. GXL conditions used for simulations at T=313 K	83
Table 4-1. Solvent conditions used for simulations	121
Table 4-2. Experimental and simulated diffusion coefficients of pyridine in CO ₂ -expanded methanol	124
Table 4-3. Experimental and simulated diffusion coefficients of pyrimidine in CO ₂ -expanded methanol	124
Table 4-4. Experimental and simulated diffusion coefficients of pyrazine in CO ₂ -expanded methanol	125
Table 4-5. Experimental and simulated diffusion coefficients of benzene in CO ₂ -expanded methanol	125

LIST OF FIGURES

Figure 1-1. Schematic representation of a gas-expanded liquid	4
Figure 1-2. Cartoon representing the cybotactic region around a probe molecule	8
Figure 1-3. Solubility of phenanthrene in CO ₂ -expanded toluene, acetone, and THF	10
Figure 1-4. Bulk mole fraction vs. local mole fraction of methanol around five different solvatochromic dyes	14
Figure 1-5. Simulation ranges of literature work plotted alongside the P-x diagram predicted by the Peng-Robinson equation of state at 298 K and 323 K.	23
Figure 2-1. Radial distribution function in CO ₂ -expanded methanol at 200, 400 and 800ps and 0.130 mole fraction CO ₂	42
Figure 2-2. Radial distribution function in CO ₂ -expanded methanol at 200, 400 and 800ps and 0.884 mole fraction CO ₂	43
Figure 2-3. Radial distribution functions for C _g -C _g interactions in CO ₂ -expanded Methanol and CO ₂ -expanded acetone	52
Figure 2-4. Orientational distribution function of C _g -C _g interactions in CO ₂ -expanded Methanol	53
Figure 2-5. Radial distribution function of O _m -H _m interactions in CO ₂ -expanded methanol and C _a -O _a interactions in CO ₂ -expanded	54
Figure 2-6. Snapshot of CO ₂ -expanded methanol simulation at 0.884 CO ₂ mole fraction	55
Figure 2-7. Orientational distribution function of O _m -H _m interactions in CO ₂ -expanded Methanol	56
Figure 2-8. Orientational distribution function of C _a -O _a interactions in CO ₂ -expanded Acetone	57
Figure 2-9. Radial distribution function of C _g -O _m interactions in CO ₂ -expanded methanol and C _g -O _a interactions in CO ₂ -expanded acetone	59

Figure 2-10 (a) Simulated self-diffusion coefficients of methanol in CO ₂ -expanded methanol vs. mole fraction carbon dioxide at 323 K (b) Simulated self-diffusion coefficients of methanol in CO ₂ -expanded methanol and Acetone in CO ₂ -expanded acetone at 298 K	66
Figure 2-11. Local number density autocorrelation functions in CO ₂ -expanded methanol	68
Figure 3-1. Molecular structure of pyrene	75
Figure 3-2. HAT5 molecule	78
Figure 3-3. Pyrene partial charges and number of carbon types from ab initio calculations.	81
Figure 3-4. Lamda (peak position) of pyrene absorbance versus mole fraction CO ₂ in CO ₂ -expanded methanol	85
Figure 3-5. Py scale ratio vs. mole fraction CO ₂ for CO ₂ -methanol, CO ₂ -acetone, and CO ₂ -acetonitrile	87
Figure 3-6. Ratio of local density to bulk density of supercritical CO ₂ around pyrene versus reduced density	80
Figure 3-7. C4s carbons on simulated pyrene molecule.	90
Figure 3-8. Radial distribution functions for C4s-C _g in CO ₂ -expanded methanol	92
Figure 3-9. Contour plot of C4s-C _g two-dimensional radial distribution function or $g(r,\theta)$ in CO ₂ -expanded methanol at $x(\text{CO}_2)=0.8$ and $P=63$ bar	93
Figure 3-10. Most probable orientation of C _g atoms around the C4s atoms of pyrene based on Figure 3-8	94
Figure 3-11. Radial distribution functions for C4s-H _m interactions in CO ₂ -expanded methanol	97
Figure 3-12. Contour plot of C4s-O _m two-dimensional radial distribution function or $g(r,\theta)$ in CO ₂ -expanded methanol at $x(\text{CO}_2)=0.8$ and $P=63$ bar	98
Figure 3-13. Most probable orientation of O _m atoms around the C4s atoms of pyrene based on Figure 3-12	99
Figure 3-14. Most probable orientation of O _m and C _g atoms around the C4s carbons of pyrene based on a combination of Figures 3-10 and 3-13	100

Figure 3-15. Radial distribution functions for C4s-C _a interactions in CO ₂ -expanded acetone	102
Figure 3-16. Simulated local composition of methanol around pyrene vs. bulk CO ₂ mole fraction in CO ₂ -expanded methanol	104
Figure 3-17. Simulated local composition of acetone around pyrene vs. bulk CO ₂ mole fraction in CO ₂ -expanded acetone	104
Figure 3-18. Simulated local composition of methanol around pyrene vs. bulk composition of methanol in CO ₂ -expanded methanol.	106
Figure 3-19 Simulated local composition of acetone around pyrene vs. bulk composition of acetone in CO ₂ -expanded acetone.	106
Figure 4-1. Solutes under investigation	116
Figure 4-2. Schematic of the Taylor-Aris dispersion technique.	117
Figure 4-3. Experimental diffusion coefficients of benzene, pyridine, pyrimidine, pyrazine and 1,3,5-triazine in CO ₂ -expanded methanol as a function of volume fraction CO ₂ .	123
Figure 4-4. Radial distribution function between nitrogen of pyridine (N _s) and the protic hydrogen of methanol (H _m) versus radius in Angstroms at 0, 0.195, and 0.686 mole fraction CO ₂	129
Figure 4-5. Radial distribution function between nitrogen of pyrimidine (N _s) and the protic hydrogen of methanol (H _m) versus radius in Angstroms at 0, 0.195, and 0.686 mole fraction CO ₂	130
Figure 4-6. Radial distribution function between nitrogen of pyrazine (N _s) and the protic hydrogen of methanol (H _m) versus radius in Angstroms at 0, 0.195, and 0.686 mole fraction CO ₂	131
Figure 4-7. Radial distribution function between carbon in benzene (C3 _s) and the protic hydrogen of methanol (H _m) versus radius in Angstroms at 0, 0.195, and 0.686 mole fraction CO ₂	132
Figure 5-1. Bulk mole fraction vs. local mole fraction of methanol around five different solvatochromic dyes at 40°C	142
Figure 5-2. Solvatochromic indicators for Kamlet-Taft solvent parameters	143
Figure 5-3. Cis-trans isomerization of azobenzenes	144

LIST OF ABBREVIATIONS

α	Kamlet-Taft hydrogen-bonding donating parameter
β	Kamlet-Taft hydrogen-bonding accepting parameter
π^*	Kamlet-Taft polarity parameter
GXL	Gas-Expanded Liquid
sc	Supercritical fluid
MD	Molecular dynamics imulations
MC	Monte Carlo simulations
C_g	Carbon in carbon dioxide
O_g	Oxygen in carbon dioxide
O_m	Oxygen in methanol
H_m	Protic hydrogen in methanol
C_a	Carbon in acetone bonded to acetone
O_a	Oxygen in acetone
$g(r)$	Radial distribution function
$g(r,\theta)$	Orientational distribution function
LNDE	Local number density enhancement
LDAC	Local density autocorrelation function
x	Mole fraction
P	pressure
T	temperature
THF	Tetrahydrofuran

MeOH Methanol

IR Infrared Spectroscopy

D Diffusion coefficient

OPLS Optimized Potential for Liquid Simulations

J2 Jorgensen Potential for Methanol

TrAPPE Transferrable Potential for Phase Equilibria

SUMMARY

Gas-expanded liquids (GXLs) are a novel and environmentally benign class of solvent systems with applications in reactions, separations, nanotechnology, drug delivery, and microelectronics. GXLs are liquid mixtures consisting of an organic solvent combined with a benign gas, such as CO₂, in the nearcritical regime. In general, liquid CO₂ is a poor solvent whereas typical organics such as acetone and methanol are good solvents. The high compressibility of GXLs enables tunability of physicochemical properties of the liquid solvent, most notably gas solubility, polarity, and dielectric constant. To summarize, GXLs combine the excellent transport properties of supercritical fluids with the high solvation power of organic liquids.

Computer simulations are valuable tools for designing and optimizing environmentally-benign and cost-effective GXLs. Computer simulations can be used in tandem with experimental techniques to elucidate the local chemistry in a system. Knowledge of the local chemistry can then be used to manipulate bulk attributes such as reaction rates. In this work, simulations yielded relevant structural information in CO₂-expanded methanol and CO₂-expanded acetone. The simulations demonstrated that addition of CO₂ resulted in clustering of methanol molecules in CO₂-expanded methanol. Furthermore, Chapter 4 of this work shows that methanol molecules form hydrogen bonds with nitrogen-containing compounds, and these hydrogen-bonding interactions increase with CO₂ pressure. Thus, the local solvation around molecules in CO₂-expanded methanol can be manipulated with CO₂ pressure. Likewise, Chapter 3 presents local compositions of organic around pyrene in CO₂-expanded organic, and these local compositions are compared to the bulk compositions. Computer simulations can predict

local compositions around a solute molecule needed to achieve a certain bulk reaction rate. Finally, Chapter 4 presents diffusion coefficients of nitrogen-containing compounds in CO₂-expanded methanol obtained by both experiments and simulations. The diffusion coefficients increase with CO₂ addition, demonstrating the enhanced transport in CO₂-expanded media.

CHAPTER I

INTRODUCTION

The primary goal of green chemistry is to develop solvents and processing methods that are environmentally benign, cost-competitive, and easily adaptable by the chemical process industry. As stated in Chemical and Engineering News¹, the goal of green chemistry is to “find ways to develop chemical products and processes that require fewer reagents, less solvent, and less energy while being safer, generating less waste, **and being profitable.**” The focus of this work is to combine computer simulations and experimental techniques for developing greener solvents. The most important challenge for scientists and engineers is to demonstrate to industry that greener solvents are just as effective in performing reactions and separations as existing, lucrative processes.

The importance of green chemistry and its development has been recognized by the U. S. Environmental Protection Agency (EPA). The EPA gave the Presidential Green Chemistry award to Eckert and Liotta² at the Georgia Institute of Technology for two decades of research in environmentally benign solvents such as near-critical water, supercritical CO₂, and gas-expanded liquids. Gas-expanded liquids are liquid mixtures consisting of an organic solvent such as acetone combined with nearcritical CO₂, which is at significantly lower process pressures than supercritical CO₂. The simplest form of a gas-expanded liquid is obtained by mixing one organic solvent with nearcritical CO₂. However, CO₂ can also induce miscibility of two immiscible organic solvents. Thus, carbon dioxide can act as a reversible miscibility switch³, facilitating downstream

separation. The solvent's physicochemical properties such as dielectric constant and viscosity can be adjusted by changes in CO₂ pressure. Furthermore, CO₂ increases diffusion, and thus reduces mass-transfer limitations.

Gas-expanded liquids are classified as greener solvents because of carbon dioxide's role as a reversible miscibility switch, and because it is environmentally benign. As an example of carbon dioxide's recent industrial use, perchloroethylene, the traditional dry-cleaning solvent, is now being replaced by supercritical CO₂. The German chemical company, Linde, has already established a chain of dry cleaners in the environmentally-conscious state of California using supercritical CO₂.⁴

The primary objective of this work is to use computer simulations to design and optimize gas-expanded liquids useful in reactions and separations. The development of these novel solvents requires an understanding of their physicochemical properties. The objective of this work is to develop computational tools for understanding physicochemical properties which would supplement experimental results. For example, one can estimate the local composition of the microenvironment from UV-vis spectroscopy. Yet the properties of this system can also be understood by computer simulations which can determine local compositions, structure, and transport.

Ganapathy, et. al.⁵ combined electron paramagnetic spectroscopy (EPR) experiments with computer simulations to study the Heisenburg spin exchange reaction between di-tert-butyl nitroxide free radicals in supercritical CO₂. The EPR experiments yielded local density augmentations, while the computer simulations calculated the reaction rates. The maximum in the rate constants corresponded to a maximum in the local density augmentation of CO₂ around di-tert-butyl nitroxide. This suggests that the

local environment around di-tert-butyl nitroxide (caused by local density augmentation of CO₂) effects the spin-exchange rate constants, a bulk observable.

The primary objective of this work is achieved by conducting the following specific tasks: a) Chapter 2 simulates the local structure and transport in gas-expanded liquids. This structural information is not easily attainable by experiment b) Chapter 3 simulates local structure and local compositions around a solute molecule in gas-expanded liquids c) Chapter 4 demonstrates the predictive capability of molecular dynamics by simulating diffusion coefficients of solutes in gas-expanded liquids and comparing to experimental results. The detailed background of gas-expanded liquids, the molecular dynamics computational tool, and technical terms used in this work are described next.

1.1 Gas-Expanded Liquids

Gas-expanded liquids are a novel and more environmentally benign class of solvent systems useful in reactions^{6,7} and separations⁸⁻¹⁰. As shown in Figure 1-1, GXLS are liquid mixtures consisting of an organic solvent combined with nearcritical CO₂, the latter being at significantly lower process pressures than supercritical CO₂. Furthermore, carbon dioxide can replace toxic organic solvents upto 80% by volume. The high compressibility of GXLS enables tunability of physicochemical properties of the liquid solvent, most notably gas solubility, polarity, and dielectric constant. To summarize, GXLS combine the excellent transport properties of supercritical fluids with the high solvation power of organic liquids.

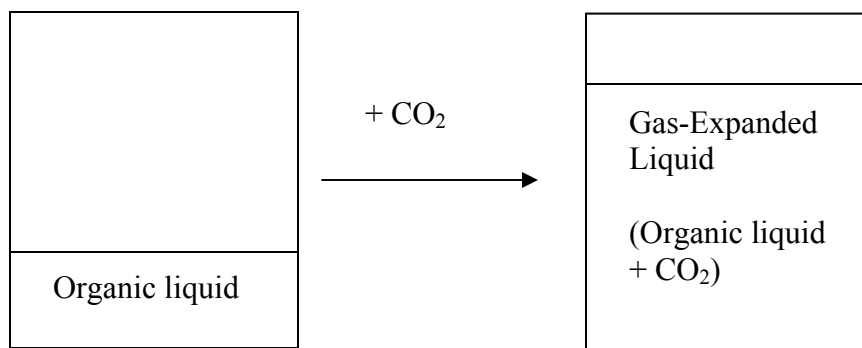


Figure 1-1. Schematic representation of a gas-expanded liquid (GXL).

Supercritical CO₂ has been widely researched as an alternative solvent, because of its non-flammable and nontoxic nature as well as being inexpensive. Carbon dioxide is nonpolar, and thus can be soluble in many organic solvents. However, its large quadrupole moment makes it soluble in more polar solvents as well. In addition to its nonpolarity, the low surface tension of CO₂ can be used to induce miscibility of two phases. Supercritical CO₂ has been shown to safely remove etch residues from silicon wafers due to its low surface tension.^{11,12} Furthermore, German chemical company, Linde, has just replaced perchloroethylene with supercritical CO₂ as a more environmentally benign dry-cleaning agent in its new chain of dry cleaners.⁴

The addition of a cosolvent to CO₂, however, enhances solubility of catalysts, ligands, highly polar reactants, and charged species. The cosolvent increases the dielectric constant and thus polarity of the overall solvent. In light of reactions, the solubility of substrates and catalysts is imperative for increased reaction rates. Musie, et. al.¹³ performed oxidations of 2,6-di-*tert*-butylphenol by cobalt Schiff base, or Co(salen*), catalyst in CO₂-expanded dichloromethane. The conversion was five times greater in the GXL than in the neat dichloromethane and still 1.25 times greater than in supercritical

CO₂. Furthermore, the turnover frequency (moles product * (catalytic site)⁻¹ * time⁻¹) was approximately forty times higher in the GXL than in supercritical CO₂. The higher turnover numbers in the GXL suggest enhanced solubility and stabilization of the catalyst in this media, which occurs in the cybotactic region of the Co(salen*) catalyst.

Other reactions investigated in CO₂-expanded media include acetal formation reactions of cyclohexanone in CO₂-expanded methanol¹⁴, acid-catalyzed reactions of diazodiphenylmethane in CO₂-expanded methanol¹⁵, and nitrile and imine hydrogenations in both CO₂-expanded methanol and CO₂-expanded THF.¹⁶ All of the above reactions make use of the fact that CO₂ reacts with water, alcohols, and amines to produce carbonic acids, alkylcarbonic acids, and carbamic acids, uniformly. Actually, the former two reactions mentioned use carbonic and alkylcarbonic acids to catalyze the reaction. Upon depressurization, the acid is automatically converted back to CO₂ + water/organic, minimizing corrosive acid waste-handling.

The present work is the first attempt at using molecular dynamics simulations to obtain local structural information and bulk transport properties in a lower-pressure GXL. These lower pressure GXLs are at temperatures ranging from 298 K-313K and pressures between 10-90 bars and are of interest to the pharmaceutical industry. Enzymes are generally very sensitive to environmental conditions, and can denature at excessive temperatures, pressures, and pH. One pharmaceutical application of GXLs is in gas-antisolvent recrystallization (GAS), a method used to precipitate out substrates by using a gas anti-solvent.^{17,18} The GAS process has been used to precipitate pharmaceutical compounds and proteins. Trypsin, lysozyme, and insulin were dissolved in neat dimethyl sulfoxide at approximately 300 K and pressures starting at 90 bars.¹⁹ Supercritical CO₂

was gradually injected until precipitation of protein powders (1-5 micrometers in diameter) occurred. The tunability of GXLs can be exploited to yield smaller particulates with narrow particle size distributions, suitable for drug delivery. A knowledge of the cybotactic region or local environment at various CO₂ pressures could assist the prediction of particle sizes and the optimization of specific GXL conditions such as solvent choice, temperature, and pressure.

GXLs are highly attractive as solvent media for five main reasons: 1) the cosolvent enhances solubilities of catalysts and reactants 2) CO₂ can enhance miscibility of two phases, which can be used to perform a reaction homogeneously. Catalyst and product recovery can then be facilitated by depressurization (to recover two immiscible phases again). This technique has been used in fluorous biphasic chemistry^{3,20} and organic-aqueous tunable solvents²¹ for enzyme reactions. 3) Carbon dioxide behaves as a high-fluidity gas and enhances transport properties 4) CO₂ in a GXL is nearcritical, at significantly lower process pressures than supercritical CO₂ 5) CO₂ is inexpensive and abundant.

1.2 The Cybotactic Region

According to the IUPAC Compendium of Chemical Technology, the cybotactic region is defined as “that part of a solution in the vicinity of a solute molecule in which the ordering of the solvent molecules is modified by the presence of the solute molecule.”²² Figure 1-2 is a schematic representation of the cybotactic region in a fluid. The largest, center circle represents a solute molecule, and the first solvation shell around the solute molecule consists of solvent and cosolvent molecules. This area around the solute molecule is the cybotactic region. If one imagines the solute to be a reactant molecule, probing the cybotactic region around this reactant molecule could enable us to manipulate the local solubility or angle of approach of a catalyst, all critical in optimizing reaction rates.

Elucidating the cybotactic region in GXLs is no trivial task. As synthetic chemists use a combination of NMR, mass spectrometry, and infrared spectrometry to determine the molecular structure of an unknown compound, similarly, several different approaches are necessary to probe the local environment. Section 1.4 details experimental techniques used in the literature for probing the cybotactic region in both supercritical fluids and gas-expanded liquids. Section 1.5 introduces molecular dynamics simulations (MD) as another solvent probe to be used in conjunction with experiments.

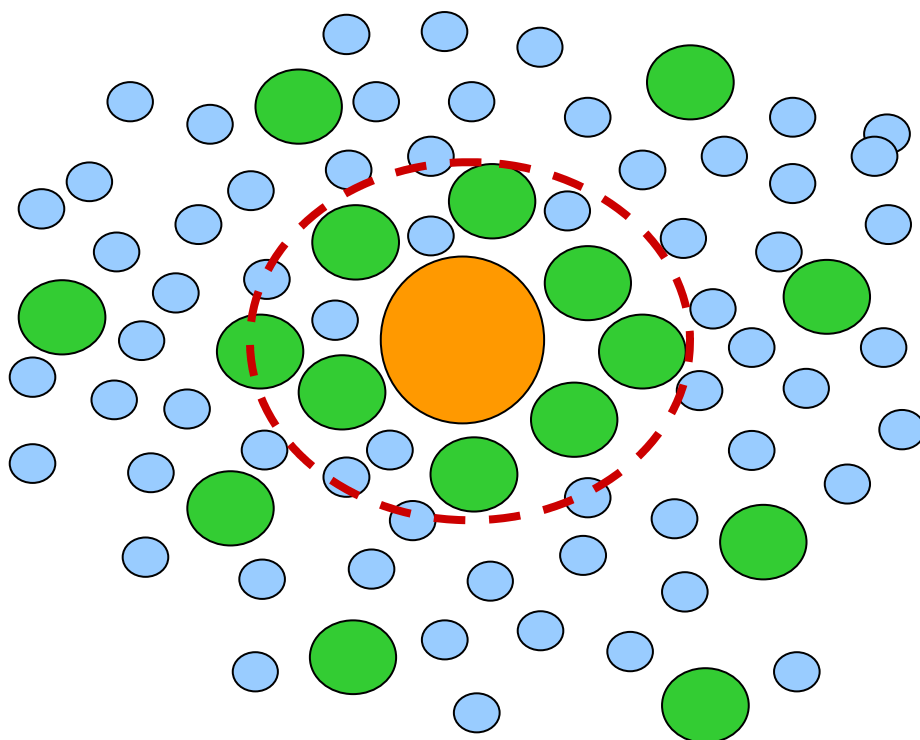


Figure 1-2. Cartoon representing the cybotactic region around a probe molecule (center circle). The solvent and cosolvent molecules comprise the first solvent shell (dotted line).

1.3 Phenanthrene solubility in GXLs “catalyzes” MD studies

The solubility of phenanthrene, a pharmaceutical intermediate, was investigated in CO₂-expanded toluene, acetone, and tetrahydrofuran at 298 K and pressures up to 60 bars.²³ The purpose of this study was two-fold: 1) to investigate the effects of cosolvent on the precipitation of phenanthrene 2) to shed light on phenanthrene solubility in CO₂-expanded organic versus the pure organic. Again, if CO₂-expanded organics are to be applied for improved separation of catalysts and products, the solvation power should remain comparable to that of the pure organic.

Figure 1-3 displays the ratio of mass-fraction of phenanthrene in CO₂-expanded toluene, acetone, and tetrahydrofuran (THF) to phenanthrene in pure organic versus the mass fraction of CO₂. In all three cases, the phenanthrene solubility slowly decreases with added CO₂ pressure. However, the solubility in acetone decreases the fastest for mass fractions less than 0.6. This suggests that the cybotactic region around phenanthrene is comprised more of the organic solvent in CO₂-expanded toluene and THF than in CO₂-expanded acetone for lower mass fraction CO₂. Furthermore, at higher CO₂ mass fractions, the cybotactic region may consist of mostly carbon dioxide for all three GXLs. Phenanthrene precipitates out of solution (as shown by a ratio that approaches zero), as CO₂ begins to penetrate the cybotactic region even more, affecting the local solubility.

Figure 1-3 gave impetus to the MD studies. Though the phenanthrene solute was not simulated, the vapor-liquid equilibria corresponding to three solubility points from Figure 1-3 were chosen as inputs to the simulation. As detailed in Chapter 2, these three points were selected to represent the full metamorphosis of the cybotactic region – from low to high CO₂ mole fraction.

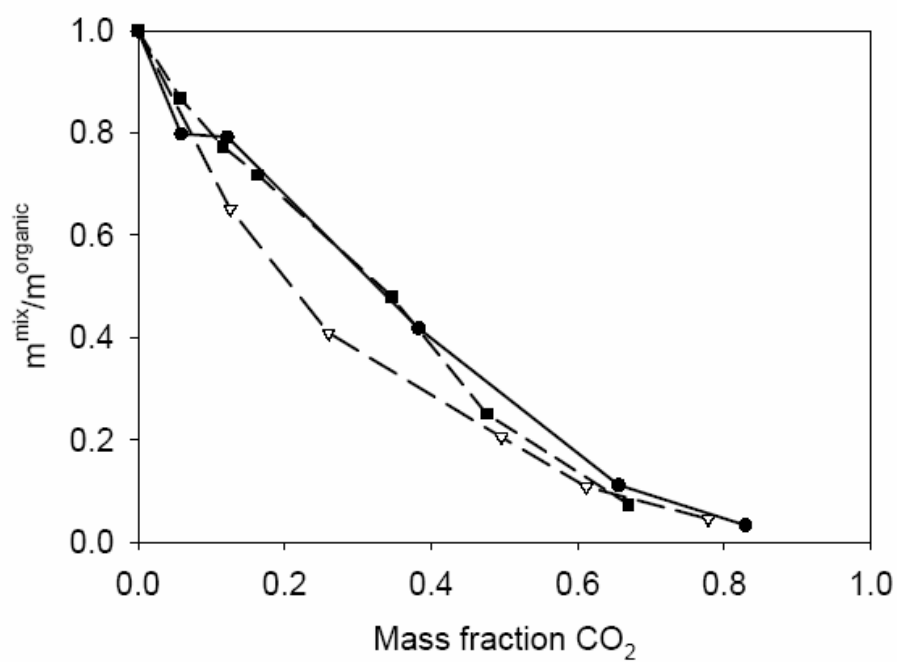


Figure 1-3. The ratio of mass fraction of phenanthrene in CO₂ + organic mixtures to phenanthrene in pure organic versus the mass fraction of CO₂ taken from Ref.23. (●) toluene, (Δ) acetone, and (■) tetrahydrofuran.

1.4 Experimental probes of the cybotactic region in supercritical fluids and GXLs.

Experimental methods are invaluable tools for elucidating the cybotactic region in both supercritical fluids and GXLs. Local densities 2-5 times greater than the bulk density were observed in supercritical CO₂ through solvatochromic shifts^{24,25}, fluorescence spectroscopy²⁶⁻²⁸, electron paramagnetic resonance spectroscopy^{29,30} and UV-vis spectroscopy³¹. Evidence of local clustering was observed by Eckert and coworkers, who confirmed the existence of large, negative partial molar volumes at solute infinite dilution in attractive mixtures near the critical point.³² Solvatochromism, infrared spectroscopy, and reactions are just three of the many informative experimental probes used in the cybotactic region of supercritical fluids and gas-expanded liquids.

Solvatochromism is a pronounced change in the position and/or intensity of an electronic emission or absorption band due to properties of the solvent. These properties include the polarity of the solvent, hydrogen-bond donating ability, and hydrogen-bond accepting ability of the solvent. The cybotactic region around a solvatochromic dye consists of solvent molecules which stabilize the ground/excited state of the dye, accordingly. Kelley and Lambert³³ used a solvatochromic dye, phenol blue, to probe the cybotactic region in various GXL systems, including CO₂-expanded methanol, acetone, and cyclohexane at 308 K and 328 K and pressures up to 70 bar. The maximum wavelength in CO₂-expanded acetone and CO₂-expanded cyclohexane decreased with increasing CO₂ pressure.

Through the use of the data obtained by Wyatt et. al.²⁴, the excess local mole fraction of methanol around several solvatochromic dyes in CO₂- expanded MeOH at 313

K and various pressures were calculated. Figure 1-4 displays the bulk mole fraction of methanol versus the local mole fraction of methanol around five different solvatochromic probes. The local mole fractions were determined by calculating the deviation of the spectral shifts in the GXLs from a linear combination of the values in the pure solvents. The data illustrate the variation of the local mole fraction of methanol up to 60% over the bulk mole fraction, with the maximum typically occurring at about 75% CO₂ in the mixture. This evidence of local composition enhancement in GXLs is similar to that observed in supercritical CO₂-cosolvent systems, but reduced in intensity.

Lalanne, et. al.³⁴ used infrared spectroscopy (IR) to investigate the stretching vibration between ethanol and CO₂ in supercritical CO₂. A strong redshift of the band center, the intensity enhancement, and distortion in the band shape all revealed an attractive interaction between CO₂ and ethanol. Furthermore, differences between the theoretical and experimental spectral shifts suggested the existence of local density enhancements. Sala et. al.³⁵ used IR to study the cybotactic region about a solute, hexamethylenetetramine, in CO₂-expanded ethanol at 313 K and 10 MPa. They observed an enhancement in solute solubility relative to that in either neat ethanol or pure CO₂. Through IR techniques, the authors proposed a local structure of ethanol and CO₂ molecules about hexyamethylenetetramine.

Reactions are also informative probes of the cybotactic region. The cis-trans isomerization of 4-4'-disubstituted azobenzenes was investigated in supercritical CO₂ at 308 K and 155 bar.³⁶ The rate constant varied with CO₂ density, demonstrating the control of reaction rates by small changes in pressure in supercritical fluids. With 0.5 mol% cosolvent, however, the reaction rate was shown to vary more than 15-fold,

suggesting strong local composition enhancements about the azobenzenes. Thompson, et. al.³⁷ performed a Diels-Alder reaction of anthracene and excess 4-phenyl-1,2,4-triazoline-3,5-dione (PTAD) in supercritical CO₂ at 313 K and pressures between 75 and 216 bar. By following the decrease in anthracene concentration, the authors determined that the reaction rate increases in the vicinity of the critical point. This increase suggests local composition enhancements of supercritical CO₂ about the cybotactic region of the transition state. The author of this work hypothesizes that the local composition enhancement is due to a combination of interaction of CO₂ with the transition state and the compressibility of the system.

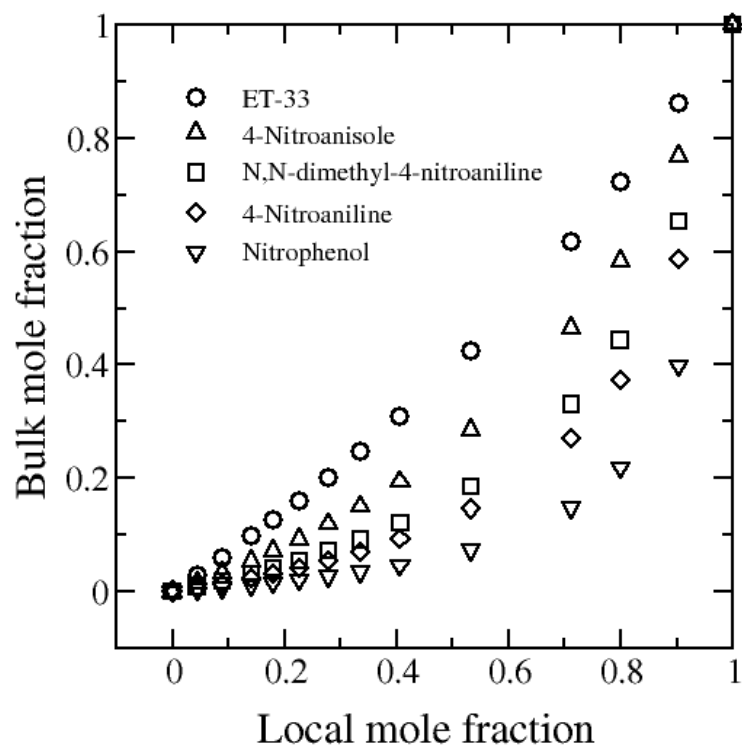


Figure 1-4. Bulk mole fraction vs. local mole fraction of methanol around five different solvatochromic dyes at 313 K: (○) ET-33 (△) 4-Nitroanisole (□) N,N-dimethyl-4-nitroaniline (◇) 4-Nitroaniline (▽) Nitrophenol. Data extracted from ref. 24.

1.5 Computer simulations as a Probe

There exist two main types of computer simulations³⁸: molecular dynamics (MD) and Monte Carlo simulations (MC). Molecular dynamics simulations yield structural information and time-dependent information. Monte Carlo yields structural information, and is most widely used to simulate vapor-liquid properties such as pressure and volume. While molecular dynamics is a deterministic approach in sampling the configurational space, Monte Carlo is a stochastic technique based on the use of random numbers and probability/statistics. MC simulations use random moves to explore the search space to determine a system property such as pressure. In a simple Monte Carlo simulation, random moves are accepted such that different regions of the configurational space are sampled at each “Monte-Carlo” step. This work, however, focuses on MD simulations, and the technical details of MD are discussed in Section 1.4.1.

Section 1.4.1 Molecular Dynamics Simulations - Background

In molecular dynamics simulations, Newton’s equations of motion are integrated to obtain the position, velocity, and force at each time step for each particle. This integration is done through finite-differencing methods. The Verlet integration algorithms – developed by French physicist Loup Verlet in 1967 – are the most commonly used integrators for MD. Among the Verlet integrators, the Velocity-Verlet algorithm³⁸ is most prevalent in the literature. During the course of an MD simulation, fixed properties such as energy (in the NVE) can drift, and this error is compounded with each time step. These property drifts are caused by large time steps and/or inaccuracies in the atomic positions at a time step, which ultimately result in inaccuracies of statistically-averaged values such

as temperature. The Velocity-Verlet algorithm addresses this problem by calculating velocities at both half-time steps and full-time steps. The general procedure of a Velocity-Verlet algorithm can be described as follows:

1) Calculate the force. The force in each direction is calculated through the following equations:

$$\begin{aligned} F_x(t) &= -\frac{dU}{dx} \\ F_y(t) &= -\frac{dU}{dy} \\ F_z(t) &= -\frac{dU}{dz} \end{aligned} \quad \text{Equation 1-1}$$

Here, U is the potential energy of the system. As detailed in Section 2.2 of Chapter 2, the potential energy of the system is represented by a combination of the Lennard-Jones and Coulomb terms. More specifically, molecules have been modeled as rigid collections of atomic sites with specified fixed charges interacting through pairwise-additive, site-site Lennard Jones and Coulomb forces. Chapter 2 details the nontrivial search in finding a suitable force field for the system. The following equation is the potential employed in the MD simulations:

$$U_{ij} = 4\varepsilon_{ij} \left\{ \left(\frac{\sigma_{ij}}{r_{ij}} \right)^{12} - \left(\frac{\sigma_{ij}}{r_{ij}} \right)^6 \right\} + \frac{q_i q_j}{r_{ij}} \quad \text{Equation 1-2}$$

where ε and σ are the Lennard-Jones energy and distance parameters, respectively. The radial distances can be converted to rectangular coordinates.

2) Calculate the half-step velocity. The following set of equations represent the Velocity-Verlet algorithm used to calculate the velocities of each particle in the system. The velocities are evaluated at half-integer time steps:

$$v\left(t + \frac{\Delta t}{2}\right) = v(t) + \frac{1}{2} \Delta t \frac{f(t)}{m} \quad \text{Equation 1-3}$$

where r is the position and Δt is the time step. The timestep generally used in MD simulations is of the order of femtoseconds. The temperature T can be calculated by equating the average kinetic energy of the particles to $3/2 k_B T$:

$$T = \frac{\sum_{i=1}^N m v_i^2}{N k_B} \quad \text{Equation 1-4}$$

where N is the total number of particles, v is the velocity, and k_B is the Boltzmann's constant.

3) Update positions. The positions of each particle in the system are then updated according to the following:

$$r(t + \Delta t) = v\left(t + \frac{\Delta t}{2}\right) \Delta t + r(t) \quad \text{Equation 1-5}$$

4) Calculate force. The force on a particle is calculated by finite-differencing the most fundamental of Newton's equations or $F=ma$:

$$F(t + \Delta t) = m \left[\frac{v(t + \frac{\Delta t}{2}) - v(t)}{\Delta t} \right] \quad \text{Equation 1-6}$$

5) Calculate the full-step velocity.

$$v(t + \Delta t) = v(t + \frac{\Delta t}{2}) + \frac{1}{2} \Delta t \frac{f(t + \Delta t)}{m} \quad \text{Equation 1-7}$$

Steps 1-5 are then repeated for the next time step t .

It is important to understand that each step is performed for each particle in the system. Periodic boundary conditions replicate the simulated box several times to produce an infinite bulk surrounding. A given particle now interacts with all other particles in the same box and all other boxes as well. The periodic boundary conditions are necessary for obtaining the best statistics of a bulk fluid; they also precludes any wall effects.

Initial positions (at time = 0) are assigned to all particles in the simulation cell. Because the equilibrium properties of a system do not depend on the initial conditions, the choice of initial configuration should not matter. To reach a sufficient equilibrium system, the simulation is generally equilibrated for 50 to 100 femtoseconds to dissipate energy and preclude any steric effects which may abort the simulation.

Section 1.4.2 Other simulation techniques

The parameters used in MD simulations are obtained from rough Hartree-Fock or Density Functional theory calculations followed by an optimization to fit experimental values. This semiempirical approach is sufficient for predicting local structure and bulk

diffusion coefficients, but it cannot treat the formation and breakage of chemical bonds necessary in simulating reactions.

Ab initio (first principles) molecular dynamics programs - such as Car-Parrinello³⁹ techniques- combine electronic structure theory with MD. The most widely used theory for studying the quantum mechanical electronic structure problem is Density Functional Theory (DFT). The electron dynamics are calculated together with the actual molecular dynamics and are fully equilibrated at each time step. The advantage of the Car-Parrinello technique is that no force-field parameters are needed.

Section 1.4.3 Simulations of tunable solvents in the literature

Petsche and coworkers⁴⁰ in their landmark paper investigated the environment surrounding infinitely dilute xenon in supercritical neon and infinitely dilute neon in supercritical xenon using molecular dynamics simulation. They observed local clustering about the former mixture and local depletion about the latter mixture through analysis of solute-solvent radial distribution functions.

Patel et al.⁴¹ performed molecular dynamics simulation of the solutes diphenylbutadiene (DPB) and hydroxymethylstilbene (HMS) in supercritical carbon dioxide to obtain rotational correlation times. The theory behind calculating rotation times is that as the local density or local composition around the solute probe increases, the friction and thus the rotational correlation time should increase. The simulated results did not agree with experiment, with simulated rotation times of DPB being 30% larger than experiment. It was suggested that the discrepancy was due to the fact that the

simulation was performed on the ground-state, whereas rotation times measured in experiment applied to the excited-state solute.

Randolph et al.^{42,43} carried out molecular dynamics simulations of reactions and collisions for nearcritical, pure Lennard-Jones molecules and observed that solute-solute correlations contribute directly to reaction rates at low density. At high densities, the authors observed that the peaks in solute-solute interactions disappear. In a subsequent paper⁵, the same authors used a combination of spectroscopic and theoretical methods to probe the effect of local solvent structure on the reaction rate for Heisenberg spin exchange. They concluded that the locally high solvent densities around solutes do indeed enhance the reaction rate of the Heisenberg spin exchange.

Tucker, et. al.^{44,45} performed molecular dynamics simulations on a two-dimensional supercritical Lennard-Jonesian fluid. The distribution of local densities around an atom was investigated as the critical point was approached. The authors were the first to suggest a long-range correlational component to the local density inhomogeneities.

Integral equation theories have also proved useful in probing the cybotactic region in supercritical fluids. For example, Debenedetti⁴⁶ employed fluctuation theory to calculate carbon dioxide excesses of over 100 molecules around naphthalene, using partial molar volume data. Wu, et al.⁴⁷ also calculated similar excesses from integral equations for dilute neon in xenon. Moreover, Chialvo and Cummings⁴⁸ used integral equation theories in supercritical dilute pyrene-carbon dioxide and dilute neon-xenon systems. They confirmed the existence of large, negative partial molar volumes at infinite

dilution of solute in attractive mixtures near the critical point, as was first shown by Eckert, et al.³²

Chatzis and Samios⁴⁹ carried out MD simulations on CO₂-methanol supercritical mixtures with methanol mole fractions < 0.12 at 323 K and pressures between 9-12 MPa. The simulated pVT (constant pressure, constant volume, and constant temperature ensemble) phase diagram at these ranges was in good agreement with experiment. Methanol clusters were observed; the radial distribution function between oxygen in methanol and the non-bonded, protic hydrogen (g_{Om-Hm}) reached a peak of 25 at around 2 Angstroms. These radial distribution functions did not vary with pressure. Furthermore, the authors plot the self-diffusion coefficient of both methanol and CO₂ in the mixture. They observe a *decrease* in the self-diffusion coefficient of both compounds with added CO₂ pressure.

Aida and Inomata⁵⁰ also carried out MD simulations on CO₂-methanol supercritical mixtures at 323 K, 11 MPa, and varying CO₂ mole fractions. Once again, methanol clusters were observed, as the g_{Om-Hm} reached a peak of 20 at around 2 Angstroms and 0.8 CO₂ mole fraction. The radial distribution functions varied with mole fraction. The authors also calculated the self-diffusion coefficient of methanol and carbon dioxide with varying methanol concentrations. The self-diffusion coefficient of methanol increased steadily upto 0.5 mole fraction CO₂, after which the self-diffusion coefficient increased rapidly.

Stubbs and Siepmann⁵¹ performed Monte Carlo simulations of aggregation studies in CO₂-expanded methanol at temperature ranges between 303.15 K and 324.9 K and 40 MPa, and 6.4 mol % methanol. Binary phase diagrams at 333 K and 353 K and pressures

between 2-15 MPa showed good agreement with experiments. However, the structural results were obtained at 303K, 313K, and 324K and 20 MPa. Again, the authors observed methanol clustering at all three temperatures with a $g_{\text{Om-Hm}}$ peak of around 40 at 20 MPa. Furthermore, the authors calculated the enthalpy of hydrogen bonding to be approximately 15 kJ/mol.

Figure 1-5 shows the simulation ranges of CO₂-methanol MD and MC simulations in the literature plotted alongside the P-x diagram of CO₂-methanol at 323 K and 298 K. The plot attempts to assist the reader in showing where the CO₂-methanol simulations of this work exist in relation to CO₂-methanol simulations from other work. The plot shows that the simulations from this work sit close to the bubble curve at 298 K. The other simulations are clearly above the critical loci of the mixture, and are hence in a single phase region.

Conclusion

Gas-Expanded Liquids (GXLs) are more environmentally benign and cost-effective solvent systems. Recent interest in GXLs as reaction media stems from enhanced solubilities and transport properties of reactants, catalysts, and ligands. By probing the cybotactic region or local environment, GXLs can be better designed and optimized for reactions and separations. Molecular dynamics (MD) simulations can yield valuable information about both the cybotactic region as well as bulk properties of a system not easily attainable by experiments. Furthermore, molecular dynamics simulations can be used in conjunction with experiments as powerful and insightful predictive tools.

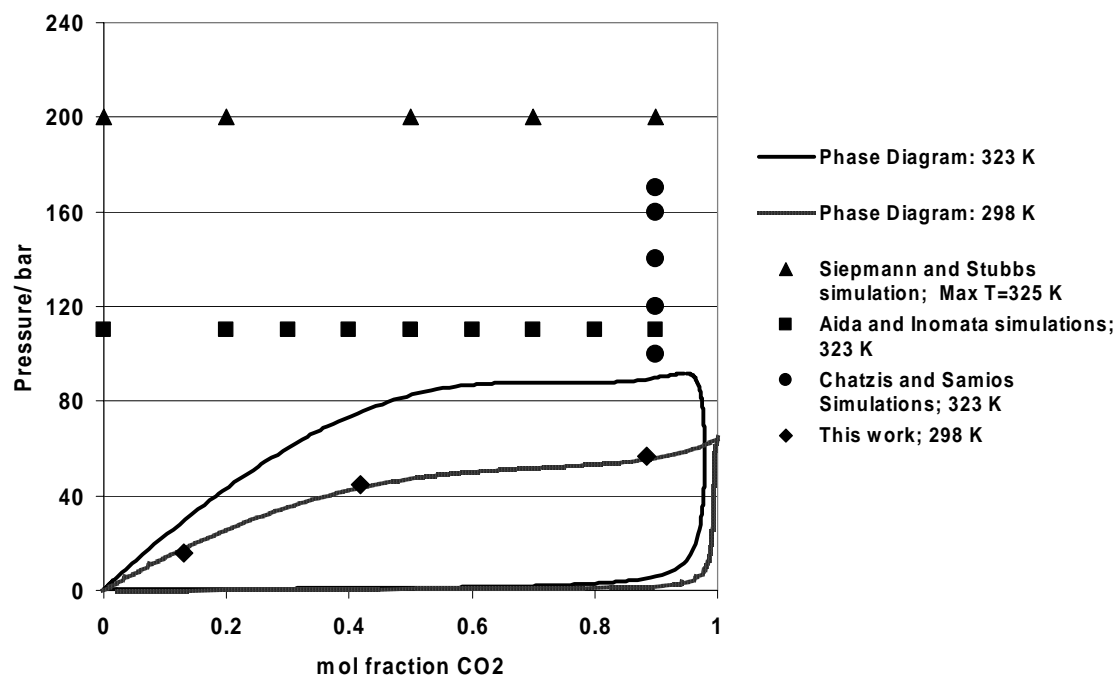


Figure 1-5. Simulation ranges of literature work plotted alongside the P-x diagram predicted by the Peng-Robinson equation of state at 298 K and 323 K.

1.6 References

- (1) Ritter, S. *Chem. and Eng. News* **2006**, 84, 7.
- (2) Ritter, S. *Chem. and Eng. News* **2004**, 82, 4.
- (3) West, K., Hallett, J., Jones, R., Bush, D., Liotta, C., Eckert, C. *Ind. Eng. Chem. Res.* **2004**, 43, 4827.
- (4) McCoy, M. *Chem. and Eng. News* **2006**, 84, 7.
- (5) Ganapathy, S., Carlier, C., Randolph, T., O'Brien, J. *Ind. Eng. Chem. Res.* **1996**, 35, 19.
- (6) Xie, X., Brown, J. S., Joseph, P. J., Liotta, C. L., Eckert, C. *Chem. Comm.* **2002**, 1156.
- (7) Jessop, P., Olmstead, M.; Ablan, C., Grabenauer, M.; Sheppard, D., Eckert, C., Liotta, C. *Inorg. Chem.* **2002**, 41, 3463.
- (8) Shishikura, A., Kanamori, K., Kinbara, H. T. *J. Agr. Food Chem.* **1994**, 42, 1993.
- (9) Chang, C., Randolph, A. *Biotechnology Progress* **1991**, 7, 275.
- (10) Sun, Q., Olesik, S. *Anal. Chem.* **1999**, 71, 2139.
- (11) Levitin, G., Myneni, S., Hess, D. *J. Electrochem. Soc.* **2004**, 151, G380.
- (12) Myneni, S., Hess, D. *J. Electrochem. Soc.* **2003**, 150, G744.
- (13) Musie, G., Wei, M., Subramaniam, B., Busch, D. *Coord. Chem. Rev.* **2001**, 219-221, 789.
- (14) Xie, X., Liotta, C.L., Eckert, C.A. *Ind. Eng. Chem. Res.* **2004**, 43, 2605.
- (15) Weikel, R. R., Hallett, J.P., Liotta, C.L., Eckert, C.A. *Topic in Catalysis* **2006**, 37, 75.
- (16) Xie, X., Liotta, C.L., Eckert, C.A. *Ind. Eng. Chem. Res.* **2004**, 43, 7907.
- (17) Owens, J., Anseth, S., Randolph, T. *Langmuir* **2003**, 19, 3926.
- (18) Matson, D., Fulton, J., Petersen, R., Smith, R. *Ind. Eng. Chem. Res.* **1987**, 26, 2298.

- (19) Winters, M. A., Knutson, B. L., Debenedetti, P. G., Sparks, H. G., Przybycien, T., Stevenson, C., Prestelski, S. *J. Pharm. Sci.* **1996**, 85, 586.
- (20) Ablan, C., Hallett, J., West, K., Jones, R., Eckert, C., Liotta, C., Jessop, P. *Chem. Comm.* **2003**, 2972.
- (21) Broering, J., Hill, E., Hallett, J., Liotta, C., Eckert, C.A, Bommarius, A. *Angew. Chem.* **2006**, 118, 4786.
- (22) McNaught, A., Wilkinson, A. *IUPAC Compendium of Chemical Technology*, 2nd ed., 1997; Vol. 66.
- (23) Lazzaroni, M., Georgia Institute of Technology, 2004.
- (24) Wyatt, V., Bush, D., Lu, J; Hallett, J., Liotta, C., Eckert, C. *J. Supercrit Fluid* **2005**, 36, 16.
- (25) Kim, S., Johnston, K. *Ind. Eng. Chem. Res.* **1987**, 26, 1206.
- (26) Betts, T., Zagrobelny, J., Bright, F. *ACS Symp. Proc.* **1992**, 488, 48.
- (27) Zagrobelny, J., Betts, T., Bright, F. *J. Am. Chem. Soc.* **1992**, 114, 5249.
- (28) Betts, T., Zagrobelny, J., Bright, F. *J. Am. Chem. Soc.* **1992**, 114, 8163.
- (29) Carlier, C., Randolph, T. *AIChE J.* **1993**, 39, 4995.
- (30) deGrazia, J., Randolph, T., O'Brien, J. *J. Phys. Chem. A* **1998**, 102, 1674.
- (31) Rice, J., Niemeyer, E., Dunbar, R., Bright, F. *J. Am. Chem. Soc.* **1995**, 117, 5832.
- (32) Eckert, C., Ziger, D., Johnston, K., Kim, S. *J. Phys. Chem.* **1986**, 90, 2738.
- (33) Kelley, S., Lemert, R. *AIChE J.* **1996**, 42, 2047.
- (34) Lalanne, P., Tassaing, T., Dante, Y., Cansell, F., Tucker, S., Besnard, M. *J. Phys. Chem. A* **2004**, 108, 2617.
- (35) Sala, S., Ventosa, N., Tassaing, T., Cano, M., Danten, Y., Besnard, M., Veciana, J. *ChemPhysChem.* **2005**, 6, 587.
- (36) Dillow, A., Brown, J., Liotta, C., Eckert, C. *J. Phys. Chem. A.* **1998**, 102, 7609.

- (37) Thompson, R., Glaser, R., Bush, D., Liotta, C.L., Eckert, C.A. *Ind. Eng. Chem. Res.* **1999**, 38, 4220.
- (38) Frenkel, D., Smit, B. *Understanding Molecular Simulation: From Algorithms to Applications*; Academic Press: San Diego, California, 2002; Vol. 1.
- (39) Car, R., Parrinello, M. *Phys. Rev. Lett.* **1985**, 55, 2471.
- (40) Petsche, I., Debenedetti, P. *J. Chem. Phys.* **1989**, 91, 7075.
- (41) Patel, N., Biswas, R., Maroncelli, M. *J. Phys. Chem. B.* **2002**, 106, 7096.
- (42) Randolph, T., Carlier, C. *J. Phys. Chem.* **1992**, 96, 5146.
- (43) Randolph, T., O'Brien, J., Ganapathy, S. *J. Phys. Chem.* **1994**, 98, 4173.
- (44) Maddox, M., Goodyear, G., Tucker, S. *J. Phys. Chem. B.* **2000**, 104, 6248.
- (45) Tucker, S., Maddox, M. *J. Phys. Chem. B.* **1998**, 102, 2437.
- (46) Debenedetti, P. *Chem.Eng.Sci.* **1987**, 42, 2203.
- (47) Wu, R., Lee, L., Cochran, H. *Ind. Eng. Chem. Res.* **1990**, 29, 977.
- (48) Chialvo, A., Cummings, P. *AIChE J.* **1994**, 40, 1558.
- (49) Chatzis, G., Samios, J. *Chem. Phys. Lett.* **2003**, 374, 187.
- (50) Aida, T., Inomata, H. *Molecular Simulations* **2004**, 30, 407.
- (51) Stubbs, J., Siepmann, I. *J. Chem. Phys.* **2004**, 121, 1525.

CHAPTER 2

MOLECULAR-DYNAMICS SIMULATIONS OF CO₂-EXPANDED METHANOL AND CO₂-EXPANDED ACETONE

2.1 Introduction

The cybotactic region is the cornerstone of most chemical engineering problems today. From the solubility and partitioning of solutes to the turnover number (moles product * (catalytic site)⁻¹ * time⁻¹) of catalysts, the local chemistry affects bulk phenomena. Therefore, an understanding of the local chemistry is invaluable for designing and optimizing gas-expanded liquids (GXLs). Simulations are advantageous because an experiment can easily be replicated on a computer. Once a computer simulation is optimized to model a relevant (and lucrative) system, it can be used as a prediction tool, saving valuable company time and money. Finally, computer simulations are useful in probing the local environment in systems, assisting the experimentalists in answering questions such as “why?” and “how?”

The work reported here investigates the synergy of molecular dynamics simulations with experiments to elucidate the cybotactic region in CO₂-expanded methanol and CO₂-expanded acetone. This synergy is optimal, as data from the experimental system is used as input into the computer simulation to create a GXL. This synergy serves two main functions: 1) The computer simulations become easier to do, because only the liquid phase is of interest with regards to reactions and simulations. Furthermore, the synergy actually becomes necessary for pure molecular dynamics simulations. The grand canonical ensemble (constant chemical potential, constant

volume, and constant temperature ensemble) necessary for phase equilibria simulations can only be done accurately using Monte-Carlo techniques.¹ 2) The simulation results can help design experiments.

Methanol is a protic solvent, whereas acetone is an aprotic solvent. Thus, different local structures in the cybotactic region of CO₂-methanol and CO₂-acetone are expected. Table 2-1 experimentally confirms this hypothesis by presenting the Kamlet-Taft parameters²⁻⁴ of methanol, acetone, and carbon-dioxide. The Kamlet-Taft parameters are α , β , and π^* , and represent the hydrogen bond donating ability, hydrogen bond accepting ability, and polarizability parameters of the solvents, uniformly. The hydrogen bond donating parameter - or α - of acetone (0.08) is similar to that of carbon dioxide (0). Thus, self-assembly of the polar species in CO₂-expanded acetone will result in limited free energy benefit. However, the alpha and beta in methanol (0.98 and 0.62) are much greater than CO₂. Based on the Kamlet-Taft values, it can be predicted that the methanol molecules – in order to minimize the system Gibbs free energy – will form clusters with each other in CO₂-expanded media.

Table 2-1. Kamlet-Taft parameters of methanol, acetone, and CO₂. The parameters for CO₂ vary with temperature and pressure, so approximate values are given based on the available literature.²⁻⁴

Solvent	α	β	π^*
Methanol	0.98	0.62	0.59
Acetone	0.08	0.51	0.68
CO ₂	0	~0	~0

2.2 Choosing a suitable force field

The most important thing in a computer simulation is the accuracy of the force field describing the molecular interactions. In theory, if an accurate force field is available, the bulk properties such as heat of vaporization of the solvent can also be accurately calculated. Finding a suitable force field for a solvent system requires some thoughtful considerations. The most important consideration is how to represent the different forces of the system. The different forces found in the CO₂-expanded methanol real system are the following:

- Forces Between Permanent Dipoles (Keesom forces)
- Forces Between a Permanent Dipole and an Induced Dipole (Debye forces)
- Forces Between Two Induced Dipoles (London-dispersion forces)
- Chemical forces (Hydrogen bonding)

Although carbon dioxide has no dipole moment⁵, it does have two individual bond dipoles. These dipoles interact with the dipole of the hydroxyl bond in the methanol

molecule, and these are known as Keesom forces. Similarly, a bond dipole of carbon dioxide can induce a charge separation in a methanol molecule, and these are known as Debye forces. Furthermore, hydrogen bonding between methanol molecules is a special chemical force.

Previous simulation work for both CO₂-expanded solvents^{6,7} and supercritical CO₂⁸⁻¹⁰ use the following intermolecular potential for simulations:

$$u_{ij} = 4\varepsilon_{ij} \left\{ \left(\frac{\sigma_{ij}}{r_{ij}} \right)^{12} - \left(\frac{\sigma_{ij}}{r_{ij}} \right)^6 \right\} + \frac{q_i q_j}{r_{ij}} \quad \text{Equation 2-1}$$

which is a combination of a Lennard Jones (first term) and Coulombic or electrostatic (second term) component. More specifically, each molecule is modeled as a rigid collection of atomic sites with specified fixed charges interacting through pairwise-additive, site-site Lennard Jones and Coulomb forces. Upon comparison with the list of forces discussed above, it is observed that the London dispersion force is properly represented. By treating the atoms as charged sites, the Coulombic force is also incorporated. In summary, the different forces found in the CO₂-expanded methanol simulated system are the following:

- Forces Between Two Induced Dipoles (London-dispersion forces)
- Electrostatic Forces between atomic sites (Coulombic)

Because Keesom and Debye forces are small compared to electrostatic and chemical forces, the question shifts to whether the hydrogen bonding force is correctly represented.

In conclusion, the simulated system includes the Van-der Waals or London dispersion term as well as the Coulombic or electrostatic term, both present in the real system. The Keesom and Debye forces are smaller compared to the Van-der Waals force,

and thus are not explicitly treated. The polarizability of the electrons are also not explicitly treated in the force field but are averaged into the Coulombic term. The next section gives more specific details about the force fields of CO₂, methanol, and acetone.

Table 2-2. Carbon dioxide parameters from TrAPPE potential.¹¹

	σ in Å	ϵ kJ/mol	q (Mulliken charge)
Cg	2.8000	0.2244	0.7
Og	3.0500	0.6565	-0.35

Table 2-3. Methanol parameters from J2 potential.¹²

	σ in Å	ϵ kJ/mol	q (Mulliken charge)
Om	3.0710	0.7110	-0.7
Hm	3.7750	0.000	0.435
CH ₃	3.4049	0.8660	0.265

Table 2-4. Acetone parameters from OPLS-derived potential.¹³

	σ in Å	ϵ kJ/mol	q (Mulliken charge)
Ca	3.7500	0.4393	0.3
Oa	2.9600	0.8786	-0.424
CH ₃	3.9100	0.6694	0.062

2.2.1 TrAPPE Potential for CO₂

The TrAPPE potential¹¹ (Transferrable Potential for Phase Equilibria) is a three-site, completely rigid model for carbon dioxide. The TrAPPE potential has been tested relative to both the vapor-liquid coexistence curve of CO₂ and vapor pressure, both with good accuracy. The parameters of the TrAPPE potential are shown in Table 2-2. In this table, the Lennard-Jones distance (σ) and energy (ϵ) parameter alongside the charge (q) of CO₂ are presented. The most interesting thing about this table is the charge of the carbon in carbon dioxide (0.7). This is of the same magnitude as the charge on the oxygen in methanol, except that it's positive, and it shows just how formidable a Lewis-Acid carbon dioxide is. In fact, alkylcarbonic acids form in CO₂-expanded alcohols because of this property.¹⁴

2.2.2 J2 Potential for Methanol

In this work, the methanol molecules are modeled using the J2¹² Potential. This potential falls under the set of OPLS (Optimized Potential for Liquid Simulations) developed by William Jorgensen in the early 1990s. The OPLS potentials were first developed through high quality ab initio techniques like density functional theory and then optimized to fit experimental properties. The J2 model is a completely rigid, united-atom model with three “sites” : Om (the oxygen in the methanol), Hm (the protic hydrogen in the methanol), and CH₃ (the methyl group). A united-atom model is a force field which treats a group (such as the methyl group) as one entity. The potential was originally tested relative to the following experimental properties:

- 1) Molecular volume (Å³)

- 2) Liquid density (g/cc)
- 3) Heat of vaporization (kcal/mol)
- 4) Heat capacity (cal/mol deg)

The coexistence curve for methanol using the J2 model was later simulated using the Gibbs Ensemble Monte Carlo method^{15,16}, and the simulated critical point corresponded to the experimental value with reasonable accuracy.

Table 2-3 shows the Lennard Jones distance (σ) and energy (ϵ) parameter alongside the charge (q), all taken from the J2 potential. The protic hydrogen (H_m) has a considerable Mulliken charge (0.435) but no Lennard Jones energy parameter, and so the hydrogen bond chemical force is represented by this point charge. Methanol molecules have been shown to exist as dimers and trimers in solution^{17,18}. However, the J2 potential treats each methanol molecule individually.

2.2.3 OPLS Potential for Acetone

The OPLS-derived potential for acetone¹³ is a completely rigid, united-atom model with 4 “sites”: Ca (central carbon of the acetone), Oa (oxygen of the acetone, attached to central carbon), and two separate CH₃ (methyl sites). Once again, the hydrogens in the methyl group are not treated explicitly. This potential was tested relative to the following experimental properties:

- 1) Experimental dipole moment
- 2) Liquid density (g/cc)
- 3) Differences in free energies of solvation (kcal/mol) in H₂O and Chloroform
- 4) Partition coefficients in H₂O/Chloroform

Table 2.4 shows the Lennard-Jones distance (σ) and energy (ϵ) parameter alongside the charge (q) of acetone. From the acetone parameters displayed in Table 2.4, one can see that the carbon of the carbonyl bond is less of a Lewis acid than carbon dioxide.

2.2.4 Justification for Choice of Force Field for the mixture

The above three force fields were chosen for simulating the GXL mixture because of logistics. Chatzis and Samios⁶ simulated methanol in supercritical CO₂ with methanol mole fractions < 0.12 at 323 K and 10-17 MPa pressure. They employed the EPM2 model¹⁹ for CO₂ and the J2 potential for methanol. The EPM2 model is also a 3-site model for CO₂, but with an added bending motion about the central carbon – an added intramolecular component. This potential was optimized for vapor-liquid equilibria calculations, and it was widely cited in the literature. When simulating the EPM2 model with the J2 potential, however, the simulations were not stable. One hypothesis could be the allotted spacing in the initial configuration. Thus, for simplicity, a rigid force field for CO₂ was actively sought, and the TrAPPE potential¹¹ was chosen. As shown in Section I of the Appendix A, Siepmann and coworkers⁷ modelled CO₂-methanol mixtures with the EPM2 potential for CO₂ alongside the TrAPPE potential. They obtained nearly exact vapor-liquid equilibria results. Thus, the TrAPPE potential was employed under the assumption that it could be used interchangeably with the EPM2 potential.

2.2.5 Cross-Interaction terms

Cross term interactions between different types of atomic sites are necessary for determining effective collision diameters and energy parameters of an interaction. The

current work employs two standard mixing rules for Lennard-Jones cross-term interactions: the Lorentz-Berthelot mixing rule and the Lorentz rule.

In the Lorentz-Berthelot mixing rule, the cross-term energy parameter is calculated by a geometric mean, and the cross-term distance parameter is calculated by an arithmetic mean:

$$\begin{aligned}\varepsilon_{12} &= \sqrt{\varepsilon_1 \varepsilon_2} \\ \sigma_{12} &= \frac{\sigma_1 + \sigma_2}{2}\end{aligned}\tag{Equation 2-2}$$

In the Lorentz mixing rule, both the cross-term energy and distance parameters are calculated by a geometric mean:

$$\begin{aligned}\varepsilon_{12} &= \sqrt{\varepsilon_1 \varepsilon_2} \\ \sigma_{12} &= \sqrt{\sigma_1 \sigma_2}\end{aligned}\tag{Equation 2-3}$$

The TrAPPE potential¹¹ for CO₂ stipulates that the CO₂-CO₂ cross terms (i.e. Cg-Og) should be calculated using the Lorentz-Berthelot mixing rules. The J2 potential¹² for methanol, however, stipulates that the methanol-methanol cross terms (i.e. Om-CH₃) be calculated using the Lorentz rule. The OPLS-derived force field for acetone¹³ also stipulates that the acetone-acetone cross terms interactions (i.e. Ca-O_g) be calculated by the Lorentz rule. For each of these cases, the mixing rule was used in this work to describe interactions between different atomic sites.

The MeOH-CO₂ and acetone-CO₂ cross terms, however, are not specified by the Trappe or J2 potentials. A consistent and verified mixing rule must therefore be established for the heterogeneous molecular-level interactions. Tables A1 and A2 of Appendix A list both the geometric (Lorentz) and arithmetic (Lorentz-Berthelot) means for the cross-term distance parameter. In almost every case, the values are the same within the error bars of these numbers, and consequently the choice of mixing rule should not affect the structural or time-dependent results significantly. For example, the largest difference between the mixing rules is seen in the cross-term distance parameter for CO₂-CO₂ cross terms (i.e. Cg-Og).

2.3 Simulation Details

In what follows, representative conditions from each of these regimes have been selected and used to conduct detailed and extensive MD simulations. Table 2-5 presents the respective saturated liquid densities and compositions taken from Chiehming et. al³⁵ selected for the simulations. The simulation system represents a single liquid phase with the density and composition determined by these experiments.

The mole fractions, densities, and temperature for the acetone-CO₂ and methanol-CO₂ GXL systems investigated here are reported in Table 2-5. Three types of low-pressure GXLs were selected for simulation: At low CO₂ mole fractions (0.10-0.35) the properties of GXLs resemble that of the pure liquid. This region is consequently called the “normal” liquid region in this work. At medium (0.36-0.75) to high (0.8-0.95) CO₂ mole fractions, the properties of GXLs resemble those of an expanded liquid in which

compressibilities increase. These regions are called the “transition” and “dilated” liquid regions, respectively.

Table 2-5. Solvent conditions used for simulations²⁰; T=298 K

Solvent	x_{CO_2}	P(bar)	$\rho^L(\text{kg/m}^3)$
Methanol (Normal Liquid Region)	0.130	16	810.3
Methanol (Transient Liquid Region)	0.418	45	846.4
Methanol (Dilated Liquid Region)	0.884	57	861.8
Acetone (Normal Liquid Region)	0.313	16	810.0
Acetone (Transient Liquid Region)	0.770	45	860.7
Acetone (Dilated Liquid Region)	0.920	57	868.5

Molecular dynamics (MD) simulations were carried out using the DL_POLY Software package²¹. Regardless of the relative composition, each simulated system box is populated by a total of 1000 molecules. Cubic periodic boundary conditions (PBCs) are used throughout, but the length of the system box is scaled to preserve the specified density as per Table 2-5. Typical box lengths are on the order of 20-50 Å, and more specifically 40-50 Å for the GXL systems simulated. Because of the PBC, the potential interactions must necessarily be cut off to less than or equal to half the box length. Coulombic interactions are handled by the Ewald summation method with automatic parameter optimization (by DL_POLY). The equations of motion were integrated using the Velocity verlet algorithm as implemented by DL_POLY using a time step of 1.0 femtosecond. Structural information (at equilibrium) has been obtained using the NVT (constant moles, constant volume, constant temperature) ensemble with a Nose-Hoover thermostat in which the relaxation constant is set to 0.3. Initial configurations of the system box are generated using a random packing of the molecules in the periodic box followed by a 50 picoseconds MD simulation at NVT conditions.

When performing preliminary simulations, initial configurations in which CO₂ molecules were placed separately from methanol (or acetone) molecules are created, occupying different parts of the simulation box. This two-phase structure was stable during the simulation time and didn't show mixing. The initial conditions for subsequent simulations, however, placed all the molecules in random positions, assuming that the CO₂ and methanol (or acetone) molecules were in a mixed, near-equilibrium state. Again, the bulk structure did not change substantially during the simulation. Thus, within the

time and length scales of our simulations, the system remains at least in a metastable state.

Statistics are collected during a 200 picoseconds MD simulation at NVT thereafter. The final equilibrium statistics are averaged over ten trajectories derived from ten different initial configuration files. The final configurations of each of the NVT runs are subsequently used as initial configurations for 300 picoseconds MD simulation runs under NVE conditions for collecting time-dependent statistics.

2.4 Testing the Force Fields and Stability of the System

2.4.1 Testing for Convergence in NVT

When performing a simulation, one assumes that the system is ergodic. This means that if a molecule were to march ahead in time and visit all of the states accessible, this time average will equal the ensemble average of the system¹. Convergence studies on the local structure are presented to indeed demonstrate the ergodicity of the system. Figures 2-1 and 2-2 present the radial distribution function or $g(r)$ of Om-Hm interactions after 200ps, 400ps, and 800ps simulations at $x_{CO_2} = 0.13$ and $x_{CO_2}=0.884$, respectively. The simulations are run in the canonical or NVT ensemble. The $g(r)$ at all three times are nearly identical, which suggests that the system is at dynamic equilibrium. Therefore, further production runs to obtain local structure in the NVT ensemble are carried out for 200 ps only.

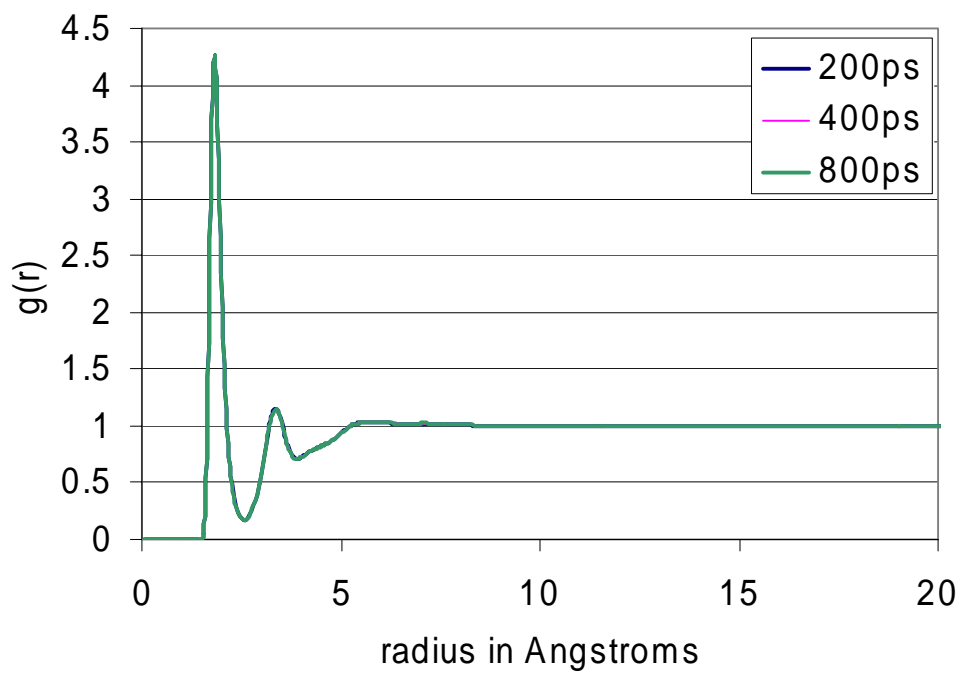


Figure 2-1. Radial distribution function or $g(r)$ of Om-Hm interaction in CO₂-expanded methanol. T=298 K, $x(\text{CO}_2) = 0.130$ after 200, 400, and 800ps simulation.

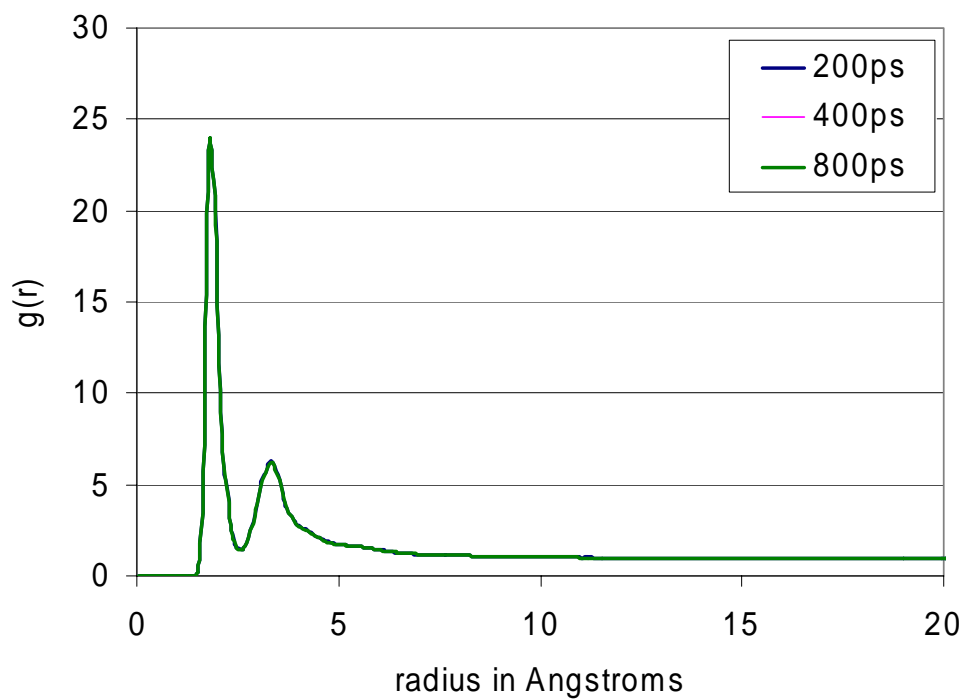


Figure 2-2. Radial distribution function or $g(r)$ of Om-Hm interaction in CO₂-expanded methanol. T=298 K, $x(\text{CO}_2) = 0.884$ after 200, 400, and 800ps simulation.

2.4.2 Pressure studies

Another method for checking system stability is to simulate the system pressure. At equilibrium, the liquid phase pressure is equal to the vapor phase pressure. Simulating the system pressure would further demonstrate the validity of our synergistic approach. In molecular dynamics, the most common method to calculate pressure is through the virial method:

$$P = \frac{2(KE) - C}{3V} \quad \text{Equation 2-4}$$

Where P = pressure

KE = kinetic energy

V = system volume

C = total configurational contribution to the virial = vdW virial + electrostatic virial + bond virial + constraint virial +

The configurational virial¹ can also be expressed as $\left\langle \sum_{i < j} f(r_{ij}) \cdot r_{ij} \right\rangle$ where $f(r_{ij})$ is the force between particles i and j at a distance r_{ij} .

Tables 2-5 and 2-6 present the simulated pressures after 200, 400, and 800ps for CO₂-methanol and CO₂-acetone simulations, respectively. The pressure for the lowest mole fraction carbon dioxide is aberrantly high in both cases. The middle mole fractions show a drop in pressure, and in the CO₂-acetone case, the pressure goes below the experimental value. Our hypothesis is that the rigidity of the system is producing high pressures.

Table 2-6. Convergence of simulated pressures for CO₂-MeOH simulations; T = 298 K; NVT Ensemble

Mole fraction CO ₂	Experimental Pressure (bar)	Simulate pressure after 200ps (bar)	Simulated pressure after 400ps (bar)	Simulated pressure after 800ps (bar)
0.130	16	175	173	177
0.418	45	46	45	44
0.884	57	99	100	100

Table 2-7. Convergence of simulated pressures for CO₂-Acetone simulations; T = 298 K; NVT Ensemble

Mole fraction CO ₂	Experimental Pressure	Simulate pressure after 200ps	Simulated pressure after 400ps	Simulated pressure after 800ps
0.330	16	77	75	75
0.770	45	26	24	25
0.920	57	102	101	90

Table 2-8. Simulated system pressures of pure methanol. T=298 K

System	Ensemble	Simulation time	Pressure (bar)
Pure methanol	NVT	400 ps	135

2.4.3 Flexible model simulations and its effects on pressure

Flexible CO₂ is simulated to ascertain the effect of flexibility on pressure. The EPM2 model¹⁹ – a widely-used potential for CO₂ – contains a bending mode about the central carbon. The Lennard Jones parameters were fit to obtain the correct internal energy and pressure at 293 K. Furthermore, the point charges were fit to reproduce the gas phase quadrupole moment; the model predicted the liquid-vapor coexistence densities including critical point very well.

Pure CO₂ at 313 K and 421 kg/m³ is simulated in the NVT ensemble with three different initial trajectories for 200 ps. The simulated average pressure is 232 bars, while the experimental value is 87 bars. The simulated pressures are highly inaccurate. This suggests that the virial equation and/or molecular dynamics techniques are insufficient to reproduce reasonable simulated pressures.

2.5 Structural Results

Local structural results are shown through radial distribution functions or $g(r)$ and orientational distribution functions or $g(r, \theta)$. The radial distribution function in plain words is the probability of finding one particle a distance r away from another particle.

Mathematically, the radial distribution function is expressed as the following:

$$g_{\alpha-\beta}(r) = \frac{\rho_{local}^{\beta}}{\rho_{bulk}^{\beta} * N_{\alpha} V} \quad \text{Equation 2-5}$$

where ρ_{local}^{β} = the average local density of β around α within a given volume shell

ρ_{bulk}^{β} = the bulk density of β

$N_{\alpha} V$ = the number of α particles

The orientational distribution function, on the other hand, is a more resolved structure than the $g(r)$, because it gives the probability of finding a particular particle a distance r and an angle θ from another molecule or probe molecule. After a probe molecule is assigned its local coordinate system (say, r , θ and φ), a number $\Delta N(r, \theta)$ of atoms of a particular type (say, A) is counted in the finite element with coordinates (r, θ) within the volume

$$\Delta V(r, \theta) = 2\pi \int_{\theta-\Delta\theta/2}^{\theta+\Delta\theta/2} \int_{r-\Delta r/2}^{r+\Delta r/2} r'^2 \sin \theta' dr' d\theta' =$$

$$2\pi \left(r^2 \Delta r + \frac{\Delta r^3}{12} \right) \left(\cos \left(\theta - \frac{\Delta\theta}{2} \right) - \cos \left(\theta + \frac{\Delta\theta}{2} \right) \right) \quad \text{Equation 2-6}$$

$\Delta N(r, \theta)$ can be found from the equation

$$\Delta N(r, \theta) = [A] \int_{\theta-\Delta\theta/2}^{\theta+\Delta\theta/2} \int_{r-\Delta r/2}^{r+\Delta r/2} g(r', \theta') \cdot 2\pi r'^2 \sin \theta' dr' d\theta', \quad \text{Equation 2-7}$$

which is the definition of $g(r, \theta)$ (here $[A]$ is the bulk number density of atoms A, or equivalently the ratio of the number of those atoms in the entire simulation box to the volume of the box).

Given $\Delta V(r, \theta)$ small enough (Δr is equal to 0.05 Å, $\Delta \theta$ is 6°), Eq. (6) becomes

$$\Delta N(r, \theta) \approx [A] g(r, \theta) \Delta V(r, \theta). \quad \text{Equation 2-8}$$

This formula is used for calculating the orientational distribution function $g(r, \theta)$.

The radial distribution function $g(r)$ is defined analogously,

$$\Delta N(r) \approx [A] g(r) \Delta V(r), \quad \text{Equation 2-9}$$

but the number $\Delta N(r)$ of atoms A is counted within a thin spherical layer

$$\Delta V(r) = 4\pi \int_{r-\Delta r/2}^{r+\Delta r/2} r'^2 dr' = 4\pi \left(r^2 \Delta r + \frac{\Delta r^3}{12} \right). \quad \text{Equation 2-10}$$

2.5.1. CO₂-CO₂ interactions

Figure 2-3 shows the $g(r)$ of C_g-C_g interactions from both (a) CO₂-expanded methanol and (b) CO₂-expanded acetone at 16, 45, and 57 bars. The $g(r)$ in both of the systems display two peaks, the first peak having a value of around 2. Again, this means that the probability of finding a C_g atom in contact with another C_g atom is 2 times greater than random. In the methanol solvent, the C_g-C_g $g(r)$ does not change significantly with addition of CO₂ pressure. In the acetone solvent, however, the addition of CO₂ decreases the first peak in $g(r)$ from 2.1 to 1.75, disrupting the CO₂-CO₂ interactions.

Figure 2-4 displays the orientational distribution function —or $g(r, \theta)$ — for C_g-C_g interactions in CO₂-expanded methanol (mole fraction CO₂=0.88, P=57 bars). (As

illustrated in Fig. 2-4b, θ is defined as the angle between the symmetry axis of the probe CO₂ and the vector from the probe C_g atom to a given C_g in the cybotactic region.) Three broad peaks in the $g(r, \theta)$ are immediately observed with θ values equal to 21, 90, and 165 degrees at 4.23, 4.03 and 4.23 Å, respectively. The existence of three peaks in C_g-C_g $g(r, \theta)$ is consistent with the results obtained by Cipriani et.al.²² However, the latter obtained peaks at 30°, 90°, and 150° in pure, saturated liquid carbon dioxide at $\rho=0.0149$ molec/Å³ and $T=240$ K. The similarity between their results and the results of the present work suggests that the local structure of CO₂ in GXLs more closely resembles a condensed liquid than a dissolved gas.

Furthermore, these $g(r, \theta)$ distributions suggest near T-shape like structures between CO₂ molecules; a finding also consistent with other simulations in the literature.²²⁻²⁵ The cartoon in Figure 2-4b shows the most probable local structure between C_g-C_g atoms situated at 21, 90, and 165 degrees with respect to a central C_g atom on a carbon dioxide molecule.

2.5.2. MeOH-MeOH interactions

Figure 2-5a displays the O_m-H_m $g(r)$ at 16, 45, and 57 bars and 298K. With added CO₂ pressure, the $g(r)$ increases and reaches a value of 23 at an r/σ ratio of 1.25 or roughly 2 Å, the length of a hydrogen bond. This means that the probability of finding an H_m atom in contact with an O_m atom is 23 times greater than random. This is a significant result. Figure 2-6 is a snapshot of the simulation at $x(\text{CO}_2)=0.884$, $P=57$ bars. Methanol molecules are shown in blue and clearly seem to form clusters within the CO₂-rich

environment. This result is corroborated by the comparison of Kamlet-Taft values in Section 2.1 and is consistent with other simulation work in the literature.^{6,7}

Figure 2-7a displays the $g(r, \theta)$ between oxygen in methanol and the nonbonded, protic hydrogen (O_m-H_m interactions) obtained in CO_2 -expanded methanol simulations: mole fraction $CO_2=0.88$, $P=57$ bar. (As illustrated in Fig. 2-7b, θ is defined as the angle between the vector formed by connecting O_m on the probe methanol to its center of mass and the vector from the O_m probe atom to any H_m in the cybotactic region.) Again a large peak at 150° and 2 \AA is observable, suggesting that methanol molecules orient themselves in a very specific manner. The most probable local structure between O_m-H_m atoms is shown by the cartoon in Figure 2-7b.

2.5.3 Acetone-Acetone interactions

Figure 2-5b shows the acetone-acetone $g(r)$ in CO_2 -expanded acetone at 16, 45, and 57 bars. Immediately, one notices that the $g(r)$ does not increase with CO_2 addition, as it did with the O_m-H_m $g(r)$. This suggests that acetone molecules do not cluster with CO_2 addition, a result also corroborated by the comparison of Kamlet-Taft values from Section 2.1. Furthermore, the peaks do not go above 1.4, which suggests weak interactions between acetone molecules. In fact, the interactions between CO_2 molecules at an r/σ ratio of 1.5 in CO_2 -expanded acetone (as shown in Figure 2-3b) are greater than the interactions between acetone molecules at the same effective radius. Intuitively, this result may not make a great deal of sense, since one may think that the carbon in acetone is a better Lewis acid. However as noted in Tables 2-2 to 2-4, the charge on the carbon in

CO₂ is 0.7, and the charge on the carbon in acetone is 0.3, while the respective oxygen charges are -0.35 and -0.424. So there is a weak interaction between acetone molecules.

The other interesting feature about Figure 2-5b is that the C_a-O_a $g(r)$ shows two peaks at an r/σ of 1.4 and 2.0. This corresponds to radii of 4.69 Å and 6.7 Å, respectively. The presence of the two simultaneous peaks in the C_a-O_a radial distribution function is consistent with simulations of pure acetone in the literature.²⁶ The orientational distribution function shown in Figure 2-8 also displays the presence of two peaks at 0° and $r=4.7$ Å and $r=6.7$ Å. The peaks are only about 2 Å apart. The authors suspect that the two simultaneous peaks are really at different ϕ angles, but projected on a two-dimensional surface. For this case, the $g(r,\theta,\phi)$ with the additional ϕ angle may be helpful in better resolving the local structure derived from the two simultaneous peaks. Also, an additional peak is observed at approximately 100° and 5 Å.

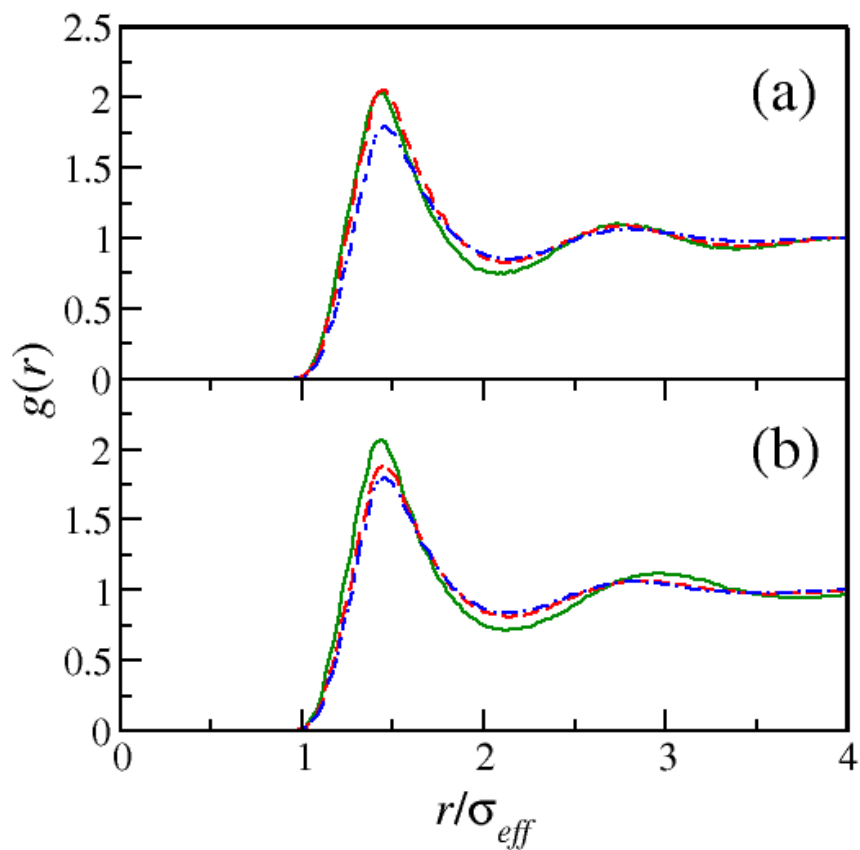
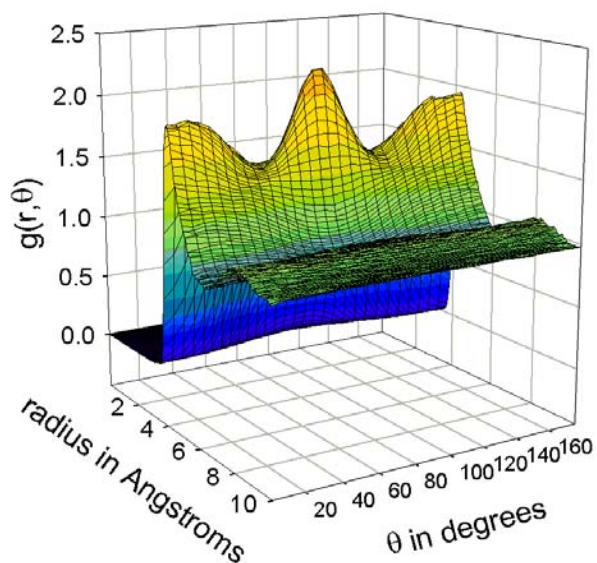
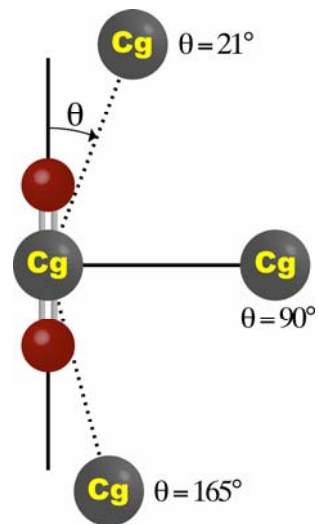


Figure 2-3. Radial distribution functions for C_g - C_g interactions between carbon dioxide molecules (a) obtained in methanol-carbon dioxide simulations at 16 (solid line), 45 (dashed line), and 57 bars (dot-dashed line), and (b) in acetone-carbon dioxide simulations at 16 (solid line), 45 (dashed line), and 57 bars (dot-dashed line). The σ of a C_g atom is 2.8 Å, and therefore the effective σ or σ_{eff} is the vdW radius of the C_g - C_g bond, again 2.8 Å. Because the intermolecular potential consists of both Coulombic and LJ interactions, the term “ σ_{eff} ” is used here.



(a)



(b)

Figure 2-4. (a) Orientational distribution function of C_g - C_g interactions in CO_2 -expanded methanol: mole fraction $CO_2 = 0.88$, $P=57$ bars. (b) Most probable orientation of C_g atoms based on Figure 2-4a.

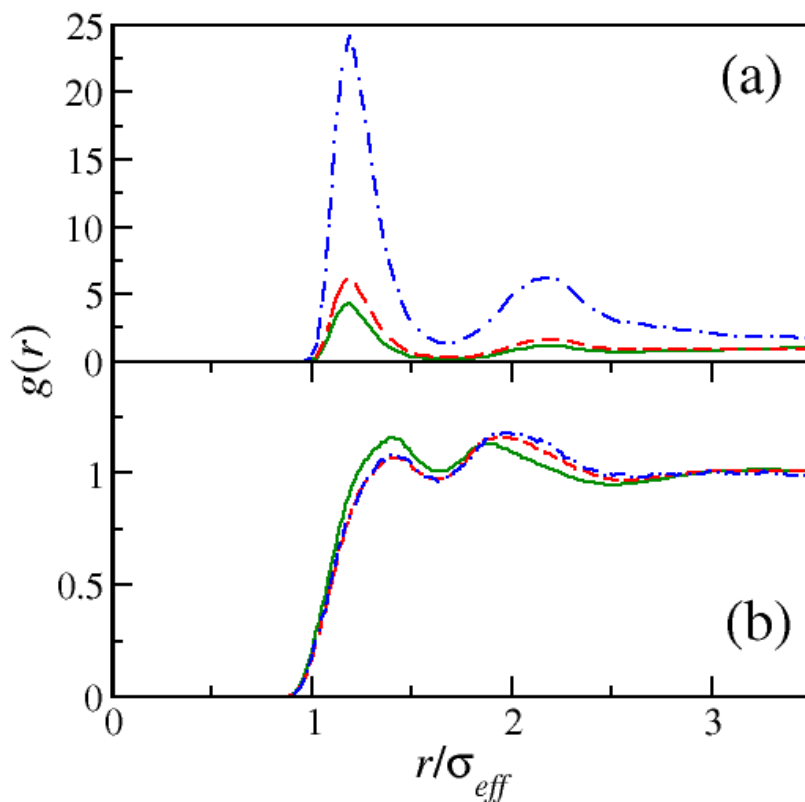


Figure 2-5. **(a)** Radial distribution function between oxygen in methanol and the nonbonded, protic hydrogen (O_m-H_m) from CO_2 -expanded methanol simulations at 16 (solid line), 45 (dashed), and 57 (dot-dashed) bars. Because the O_m-H_m interactions are being specified by LJ and Coulombic interactions, there's no specified σ . In the model, the LJ σ is 3.071 Å and 0 Å for methanol and hydrogen, respectively. Therefore, the effective sigma is the average of the O_m and H_m sigmas, or $3.071/2 = 1.535$ Å **(b)** Radial distribution function between the aprotic carbon in acetone and the aprotic oxygen in acetone (C_a-O_a) from CO_2 -expanded acetone simulations at 16 (solid), 45 (dashed), and 57 (dot-dashed) bars. The σ for C_a and O_a are 3.75 and 2.96 Å, respectively. Therefore, the effective sigma or σ_{eff} is 3.35 Å.

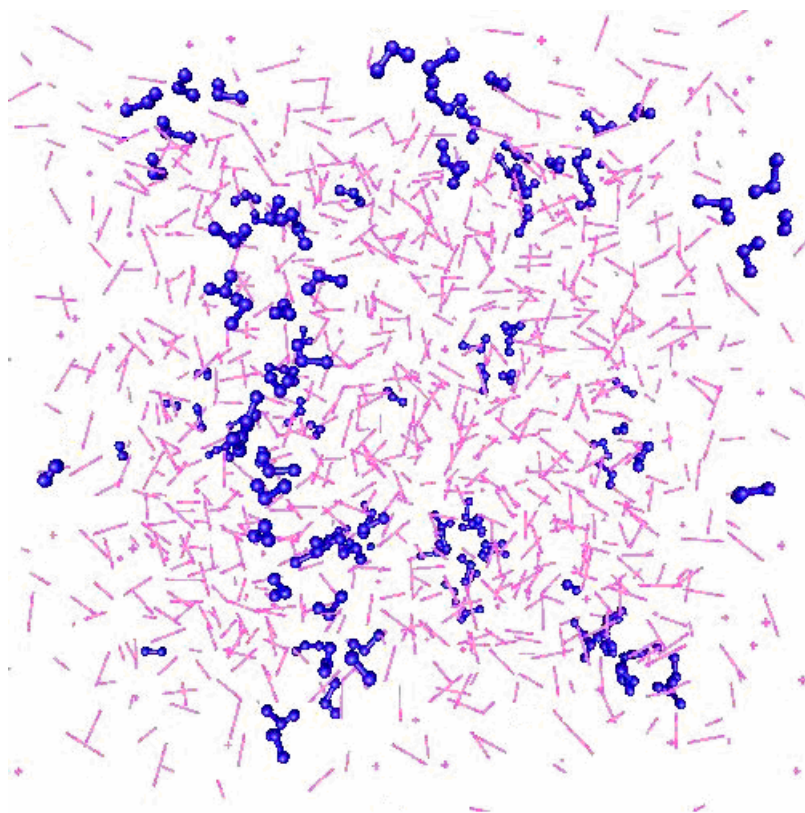
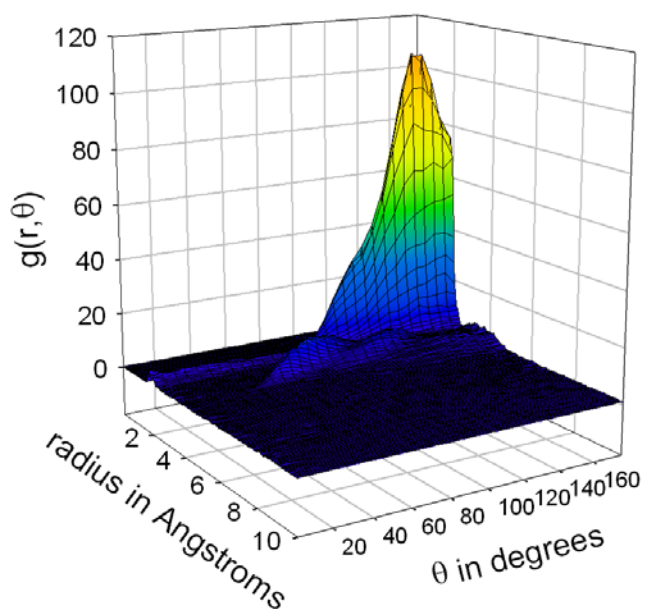
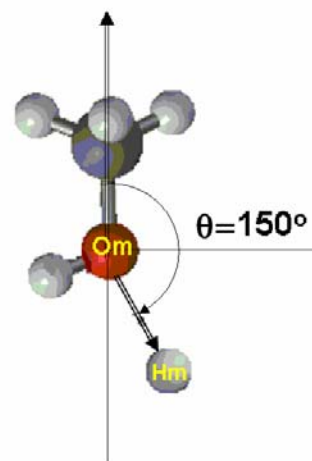


Figure 2-6 Diminishing perspective plot of a snapshot of a simulated trajectory in CO₂-expanded methanol at mole fraction CO₂=0.88, and P=57 bar. Methanol molecules (in blue) represent the larger structures consisting of 3 effective atoms: oxygen (O_m), protic hydrogen (H_m), and the methyl group (CH₃). Because of the diminishing perspective, some of the methanol molecules appear to have only 2 atoms; the third atom is in the linear plane of the molecule. The long, pink sticks represent carbon dioxide molecules.



(a)



(b)

Figure 2-7 (a) Orientational distribution function of oxygen in methanol and the nonbonded, protic hydrogen (O_m - H_m interactions) from CO_2 -expanded methanol: mole fraction $CO_2=0.88$, $P=57$ bars. (b) Most probable orientation between O_m - H_m atoms based on Figure 6a.

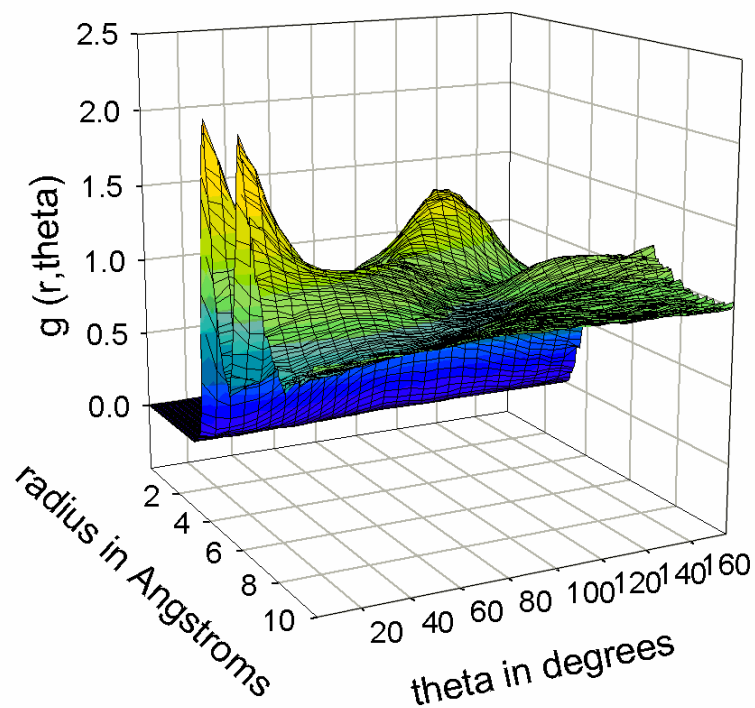


Figure 2-8. Orientational Distribution Function of carbon in acetone and nonbonded oxygen in acetone (C_a-O_a) interactions from CO_2 -expanded acetone simulations: mole fraction $CO_2 = 0.313$, $\rho=810.0 \text{ kg/m}^3$

2.5.4. Carbon Dioxide Interactions with Solvent

Radial distribution functions for interactions between carbon dioxide and methanol and carbon dioxide and acetone are presented in Figure 2-9. For CO₂-expanded methanol simulations, CO₂-methanol interactions are represented by the carbon in CO₂ and oxygen in methanol (C_g-O_m) $g(r)$. Likewise, the CO₂-acetone structure is obtained by analyzing the carbon in CO₂ and oxygen in acetone (C_g-O_a) $g(r)$.

There are two salient points that can be derived from this figure: 1) the first peak in the C_g-O_a $g(r)$ is greater than the first peak in the C_g-O_m $g(r)$, with an additional second peak. This figure is included to show that formation of clusters between methanol molecules in CO₂-expanded methanol produces decreased CO₂-MeOH correlations. The absence of significant clustering of acetone molecules in CO₂-expanded acetone, however, leaves acetone molecules relatively more available to interact with CO₂. This suggests that CO₂-acetone molecules are more structured in the GXL than CO₂-MeOH molecules. 2) At first glance, one would expect more interaction between C_g-O_m, because the magnitude of both of their charges is equal and negative to each other. However, the O_m chooses to interact with the protic hydrogen instead.

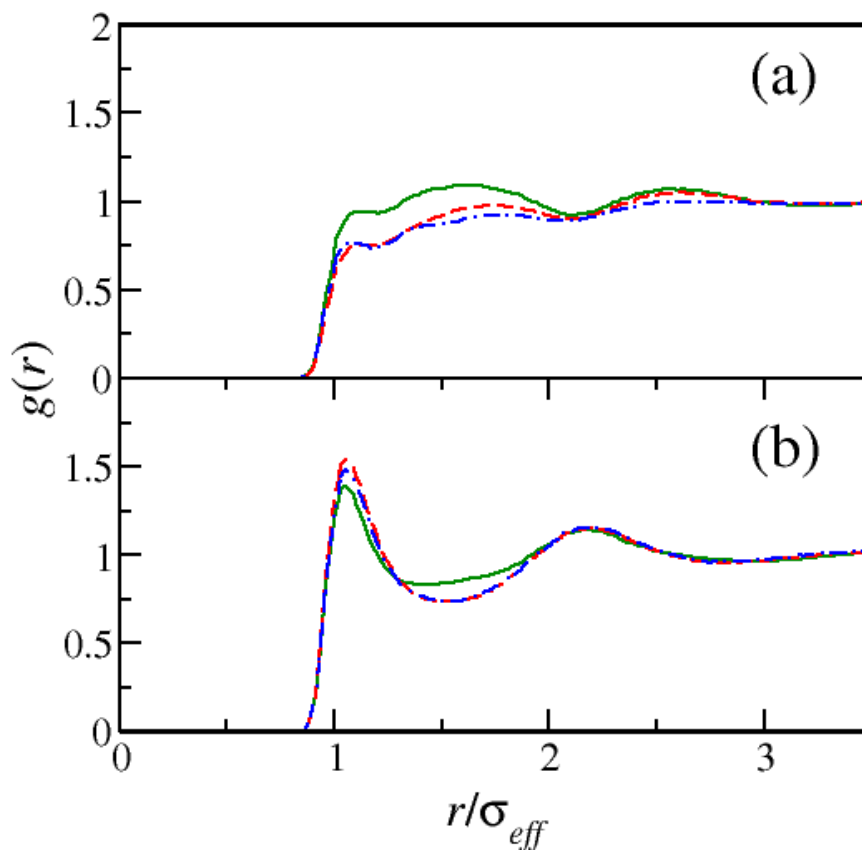


Figure 2-9 a) Radial distribution function between carbon in carbon dioxide and the oxygen in methanol (C_g-O_m) from CO_2 -expanded methanol simulations at 16 (solid line), 45 (dashed), and 57 (dot-dashed) bars. Because the C_g-O_m interactions are being specified by LJ and Coulombic interactions, there's no specified σ . In the model, the LJ σ is 2.8 Å and 3.071 Å for carbon and oxygen, respectively. Therefore, the effective sigma is the average of the O_m and H_m sigmas, or $(2.8+3.071)/2 = 2.932$ Å **(b)** Radial distribution function between the carbon in carbon dioxide and the aprotic oxygen in acetone (C_g-O_a) from CO_2 -expanded acetone simulations at 16 (solid), 45 (dashed), and 57 (dot-dashed) bars. The σ for C_g and O_a are 2.8 and 2.96 Å, respectively. Therefore, the effective sigma or σ_{eff} is 2.88 Å.

2.5.5. Local Number Density Calculations

The local number density is an informative way of converting the radial distribution function into a more physically intuitive form. The local number density is defined by the following:

$$\rho_{local} = \frac{\bar{N}(R_{cut})}{\frac{4\pi}{3}(R_{cut}^3 - \sigma_{exc}^3)} \quad \text{Equation 2-11}$$

where $\bar{N}(R_{cut})$ is the average number of particles of a particular atom type within the solvent sphere of radius R_{cut} about the probe and given by the following:

$$\bar{N}(R_{cut}) = 4\pi \frac{N_{bulk}}{V} \int_{\sigma_{exc}}^{R_{cut}} g(r) r^2 dr \quad \text{Equation 2-12}$$

Here N_{bulk} is the total number of bulk particles and V is the volume of the simulation box, and σ_{exc} is the excluded radius as defined by the impenetrable volume of the probe molecule. The local number density enhancement is the ratio of the local number density to the bulk number density where $\rho_{bulk} = N_{bulk}/V$.

Tables 2-9 and 2-10 present local number density enhancements for four targeted interactions from CO₂-expanded methanol and acetone simulations, respectively. (Here C_g-C_g interactions characterize the local density of C_g atoms around a probe C_g.) While negligible enhancements exist for C_g-C_g interactions, the number density enhancement between O_m-H_m interactions increases six-fold in the dilated liquid region. However, no significant local number density enhancement for C_a-O_a interactions from CO₂-expanded acetone simulations is observed.

The presence of carbon dioxide is far more effective in inducing clustering of methanol molecules than acetone molecules. This conclusion can be deduced by

analyzing local number density values with CO₂ addition. The absolute values of the local number densities of H_m around O_m are 0.0141 and 0.0094 molecules/Å³ in the normal and dilated liquid regions, respectively. With a nine-fold decrease in the *bulk number density* of methanol, relatively little change (~30%) in the *local number density* (of H_m around O_m) is observed. Because these values do not change significantly (despite significant dilution), it is confirmed that methanol forms clusters and remains in clusters in a CO₂ environment. However, the absolute values of the local number densities of O_a around C_a are 0.0069 and 0.00104 molecules/Å³ in the normal and dilated liquid regions, respectively. With a 6.7-fold decrease in the *bulk number density* of acetone, a comparable 6.6-fold decrease in the *local number density* of (O_a around C_a) is observed. In other words, the number of acetone molecules in the first shell is diluted by CO₂ molecules in proportion to the mole fraction of CO₂. Thus, there is practically no influence due to specific nonideal interactions between the molecules (in contrast to the methanol mixture in which hydrogen bonding strongly distorts the structure).

Table 2-9. Local Number Density Enhancements (LNDE) for C_g-C_g interactions and O_m-H_m interactions from CO₂-expanded methanol simulations.

Interaction	$x(\text{CO}_2)$	$R_{\text{cut}}(\text{\AA})$	ρ_{local} (Molecules/ \AA^3)	ρ_{bulk} (Molecules/ \AA^3)	LNDE ($\rho_{\text{local}}/\rho_{\text{bulk}}$)
C _g -C _g (Normal liquid region)	0.130	5.975	0.0020	0.0019	1.08
C _g -C _g (Dilated liquid region)	0.884	5.975	0.0113	0.0107	1.05
O _m -H _m (Normal liquid region)	0.130	2.675	0.0141	0.0126	1.11
O _m -H _m (Dilated liquid region)	0.884	2.675	0.0094	0.0014	6.81

Table 2-10. Local Number Density Enhancements (LNDE) for C_g-C_g interactions and C_a-O_a interactions from CO₂-expanded acetone simulations.

Interaction	$x(\text{CO}_2)$	$R_{\text{cut}}(\text{\AA})$	ρ_{local} (Molecules/ \AA^3)	ρ_{bulk} (Molecules/ \AA^3)	LNDE ($\rho_{\text{local}}/\rho_{\text{bulk}}$)
C _g -C _g (Normal liquid region)	0.313	5.975	0.0029	0.0028	1.03
C _g -C _g (Dilated liquid region)	0.920	5.975	0.0118	0.0106	1.05
C _a -O _a (Normal liquid region)	0.313	5.425	0.0025	0.0062	0.89
C _a -O _a (Dilated liquid region)	0.920	5.425	0.00947	0.0106	0.89

2.6 Time-Dependent Results

2.6.1. Diffusion Coefficients

Diffusion coefficients of both methanol in CO₂-expanded methanol and acetone in CO₂-expanded acetone are simulated with added CO₂. Self diffusion coefficients are calculated using the Einstein relation¹:

$$D = \lim_{t \rightarrow \infty} \frac{1}{6t} \langle [\vec{r}(t) - \vec{r}(0)]^2 \rangle \quad \text{Equation 2-13}$$

The simulated self-diffusion coefficients of methanol in CO₂-expanded methanol at 323 K are displayed in Figure 2-9a alongside those obtained by Aida and Inomata.²⁷ Aida and Inomata employ a three-site, flexible model for both methanol and carbon dioxide and incorporate ionization potentials in the mixing rules. Both the J2 potential for methanol used in this work and the flexible potential used in Aida and Inomata's work were fit to the experimental, saturated liquid density of methanol at ambient temperature and pressure. The subsequent optimized potential was used to simulate the methanol coexistence curve. Coexistence curves obtained using the methanol potential of Aida and Inomata's are better correlated to those obtained by experiment²⁸ than the J2 potential.

The purpose of Figure 2-10a was to determine how accurate the J2 model of methanol is in relation to other literature potentials. As shown in Figure 2-10a the simulated self-diffusion coefficients of methanol in CO₂-expanded methanol obtained in this work are in reasonable agreement to those obtained by Aida and Inomata at very low and high mole fraction CO₂. At less than 50 mole% carbon dioxide, however, the self-diffusion coefficients of Aida and Inomata remain constant with mole% CO₂, whereas in the present work the values steadily increase. For reference, Figure 2-10a also includes an

experimental data point for benzene diffusion in GX-methanol at 313 K that has been adjusted to an approximate value for methanol using the Wilke-Chang equation.²⁹ An explanation of the Wilke-Chang ratio is included in section IV of Appendix A.

The self-diffusion coefficient of pure methanol at 323 K determined in this work ($2.85 \times 10^{-9} \text{ m}^2/\text{s}$) is about 40% of that obtained by Taylor-Aris dispersion techniques³⁰ ($6.9 \times 10^{-9} \text{ m}^2/\text{s}$), which is approximately the uncertainty in Aida and Inomata's results. This suggests that methanol force fields optimized to fit the saturated liquid density may not be optimal for transport values. However, the significance of our models is that they reproduce accurately the trends experimentally observed: that CO_2 enhances transport properties (namely diffusion) in the GXL systems investigated.

Figure 2-10b displays the simulated self-diffusion coefficients of i) methanol in CO_2 -expanded methanol and ii) acetone in CO_2 -expanded acetone. Once again, the results correctly predict an increase in diffusion upon addition of CO_2 . Peculiarly, the acetone diffusion in the GXL is greater than methanol diffusion at all CO_2 concentrations. One expects the converse, as the methanol molecules are smaller both in size and weight compared to the acetone molecules. Again, experimental NMR points obtained by McCall et. al.³¹ are included for reference. While the simulated self-diffusion coefficient for pure methanol at 298 K remains smaller than its experimental point, the simulated pure acetone diffusion is greater. Although our values for diffusion coefficients are not in exact agreement with experimental values, the models reproduce the general trend of enhanced solvent diffusivity with CO_2 addition.

Further, one may expect that the acetone diffusion rate (MW 58) is less than that of methanol (MW 32) because of the lower molecular weight of acetone. However,

because of the extent of hydrogen bonding of alcohols in solution,^{17,18} the “effective” molecular weight of the methanol moieties diffusing may be substantially greater than 58. An alternate explanation, though not explored here, is that the strong hydrogen bonding forces may reduce the effective diffusivity of one methanol molecule.

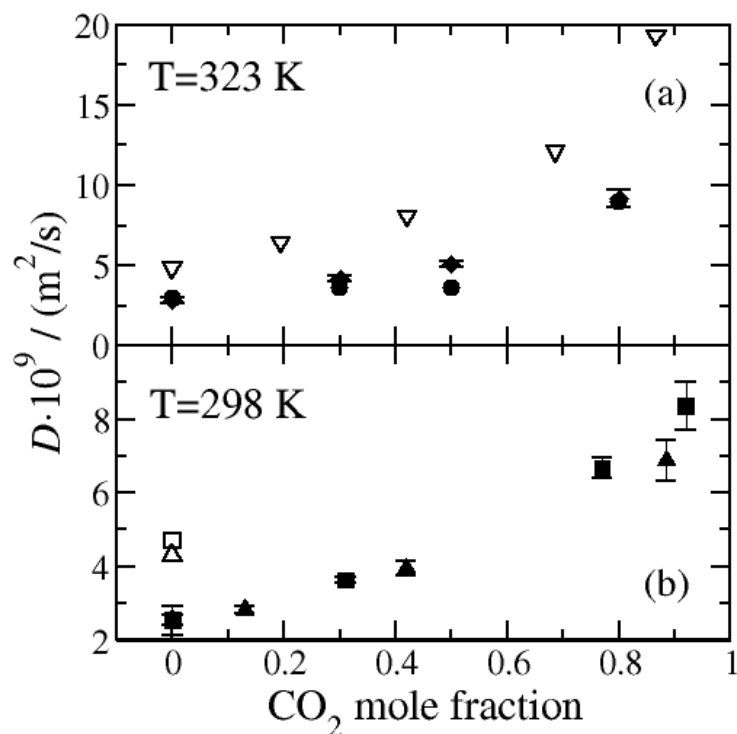


Figure 2-10. (a) Simulated self-diffusion coefficients of methanol in CO_2 -expanded methanol vs. mole fraction carbon dioxide at 323 K: (\blacklozenge) this work, (\bullet) simulated values from Aida and Inomata⁴⁵ obtained through visual interpolation, and (∇) values at 313 K approximated using Wilke-Chang equation with parameters fit from experimental values of Sassi et al.⁴⁷ (b) Simulated self-diffusion coefficients of (\blacktriangle) methanol in CO_2 -expanded methanol and (\blacksquare) Acetone in CO_2 -expanded acetone at 298 K. Self-diffusion coefficients determined experimentally by NMR⁴⁸ for (\square) pure acetone and (\triangle) pure methanol are included. Error bars in the diffusion coefficients were determined by root-mean-square deviations from the average value.

2.6.2. Local Density Autocorrelation Functions

The local density autocorrelation function (LDAC) is a collective diffusion event which gives an indication of persistence of cluster times. Two time constants are determined from the local density autocorrelation function: the instantaneous (τ_i) and steady state (τ_s). These are necessary to distinguish between the ballistic regime or transient regime and the steady state regime. The former possesses nonlinear behavior in the mean-squared displacement with respect to time, whereas the latter regime displays linear behavior. The analysis of the time constants will be done for the steady state regime only, because the latter is for much longer time scales and is most indicative of the persisting molecular phenomena. The local number density autocorrelation function is given by the following:

$$C(t) = \frac{\langle \delta\rho(0)\delta\rho(t) \rangle}{\langle \delta\rho(0)^2 \rangle} \quad \delta\rho(t) = \rho(t) - \bar{\rho}, \quad \text{Equation 2-14}$$

where $\rho(t)$ is the local number density at time t and $\bar{\rho}$ is the ensemble average local number density. The cutoff radius for density determination was taken to be the minimum in the first peak of the radial distribution function, as was employed by Tucker and coworkers^{8,32}. Equation 2-14 can then be discretized to a numerically tractable expression,

$$C(t) = \frac{\sum_{i=1}^{N_{tot}} (N_i(R_{cut}, t) - \bar{N}(R_{cut})) (N_i(R_{cut}, 0) - \bar{N}(R_{cut}))}{\sum_{i=1}^{N_{tot}} (N_i(R_{cut}, 0) - \bar{N}(R_{cut})) (N_i(R_{cut}, 0) - \bar{N}(R_{cut}))}, \quad \text{Equation 2-15}$$

where $N_i(R_{cut}, t)$ is the local number of neighbor atoms within the cutoff radius at time t , $\bar{N}(R_{cut})$ is defined in Equation 2-12.

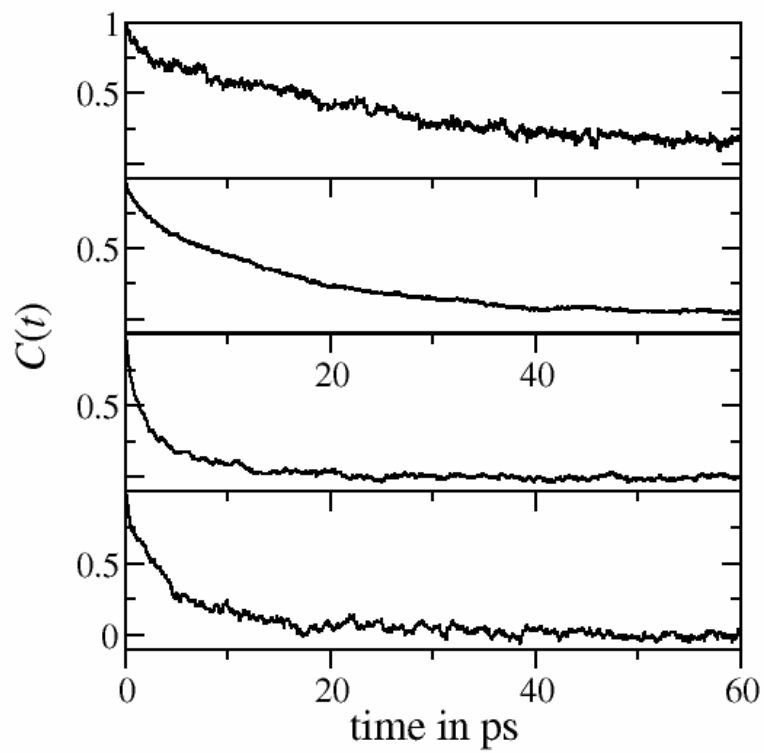


Figure 2-11. Local number density autocorrelation functions of: **(a)** O_m-H_m interactions from CO_2 -expanded methanol simulations at the dilated liquid region: $x_{CO_2}=0.884$; $\rho=864.8 \text{ kg/m}^3$ **(b)** O_m-H_m interactions from CO_2 -expanded methanol simulations at the normal liquid region: $x_{CO_2}=0.130$; $\rho=810.3 \text{ kg/m}^3$; **(c)** C_g-C_g interactions from CO_2 -expanded methanol simulations at the dilated liquid region; and **(d)** C_g-C_g interactions from CO_2 -expanded methanol simulations at the normal liquid region.

Figure 2-11 displays the local number density autocorrelation functions of both C_g-C_g interactions for a cutoff radius of 5.975 Å in CO₂-expanded methanol and O_m-H_m interactions for a cutoff radius of 2.675 Å. The time constants can be determined from the slope of a semilog plot of the local density autocorrelation function vs. time. Section VI of Appendix A presents the semilog plots of both the instantaneous regime and steady state regime from the corresponding LDACs shown in Figure 2-11.

Both time constants are catalogued in Table 2-11, and three salient conclusions can be drawn: 1) the O_m-H_m correlations in both the instantaneous and steady state regimes persist longer than the C_g-C_g correlations 2) the C_g-C_g correlations in the dilated liquid region are around 25% less than those in the normal liquid region 3) most importantly, the steady state time constants are 54.2 ps and 79.3 ps for O_m-H_m interactions in the normal and diluted liquid regions, respectively. Steady state time constants obtained from local number density autocorrelation functions show that O_m-H_m interactions between methanol molecules persist about 50% longer in the dilated liquid region than in the normal liquid region. Thus CO₂ increases the persistence time of methanol interactions, a result which can be explained by the higher α and β Kamlet-Taft parameters of methanol when compared to acetone or CO₂. The methanol molecules decrease their Gibbs excess energy in a CO₂ environment by interacting with like-like hydrogen bonding forces.

Table 2-11. Instantaneous (τ_i) and steady state (τ_s) time constants in ps from correlation functions plotted in Table 2-10.

Interaction	τ_i (ps)	τ_s (ps)
C _g -C _g Correlations (Normal liquid region)	11.5	20.4
C _g -C _g Correlations (Dilated liquid region)	7.2	14.9
O _m -H _m Correlations (Normal liquid region)	23.5	54.2
O _m -H _m Correlations (Dilated liquid region)	22.2	79.3

Conclusions

The cybotactic region of CO₂-expanded methanol and CO₂-expanded acetone is probed using molecular dynamics simulations. The systems are simulated at 298 K and several representative densities corresponding to available experimental data. This corresponds to pressures between 16-57 MPa. Comparison between simulated diffusion coefficients from this work and experimental values suggests that GXL models work reasonably well in predicting general trends such as local structure and diffusion coefficients. The results are qualitatively consistent at the macroscopic level with those found using solvatochromic Kamlet-Taft parameters.

2.7 References

- (1) Frenkel, D., Smit, B. *Understanding Molecular Simulation: From Algorithms to Applications*; Academic Press: San Diego, California, 2002; Vol. 1.
- (2) Kamlet, J., Taft, R. *J. Am. Chem. Soc.* **1976**, 98, 2866.
- (3) Kamlet, M., Taft, R. *J. Am. Chem. Soc.* **1976**, 98, 377.
- (4) Kamlet, M., Abboud, J., Taft, R. *J. Am. Chem. Soc.* **1977**, 99, 6027.
- (5) Raveendran, P., Ikushima, Y., Wallen, S. . *Acct. Chem. Res.*, A.
- (6) Chatzis, G., Samios, J. *Chem. Phys. Lett.* **2003**, 374, 187.
- (7) Stubbs, J., Siepmann, I.,. *J. Chem. Phys.* **2004**, 121, 1525.
- (8) Tucker, S., Maddox, M. . *J. Phys. Chem. B.* **1998**, 102, 2437.
- (9) Biswas, R., Lewis, J., Maroncelli, M. . *Chem. Phys. Lett.* **1999**, 310, 485.
- (10) Patel, N., Biswas, R., Maroncelli, M. . *J. Phys. Chem. B.* **2002**, 106, 7096.
- (11) Potoff, J., Siepmann, I. *AIChE J.* **2001**, 47, 167.
- (12) Jorgensen, W. *J. Phys. Chem.* **1986**, 90, 1276.
- (13) Jorgensen, W., Briggs, J., Contreras, M. *J. Phys. Chem.* **1990**, 94, 1683.
- (14) West, K., Wheeler, C.. *J. Phys. Chem. A.* **2001**, 105, 3947.
- (15) Mezei, M. *Mol. Simul.* **1992**, 9, 257.
- (16) Leeuwen, M., Smit, B. *J. Phys. Chem.* **1995**, 99, 1831.
- (17) Karachewski, A., McNeil, M., Eckert, C. **1989**, 28, 315.
- (18) Karachewski, A., Howell, W., Eckert, C. *AIChE J.* **1991**, 37, 65.
- (19) Harris, J., Young, K. *J. Phys. Chem.* **1995**, 99, 12021.
- (20) Chiehming, C., Kou-Lung, C., Chang-Yih, D. *J. Supercrit Fluid* **1998**, 12, 223.
- (21) Smith, W., Forester, T.R., 1996.

- (22) Cipriani, P., Nardone, N., Ricci, F.P., Ricci, M.A. *Mol. Phys.* **2001**, *99*, 301.
- (23) Fedchenia, I., Schroder, J., *J. Chem. Phys.* **1997**, *106*, 7749.
- (24) Ishli, R., Okazaki, S., Okada, I., Furusaka, M., Watanabe, N., Misawa, M., Fukunaga, T. *J. Chem. Phys.* **1996**, *105*, 7011.
- (25) Zhang, Y., Yang, J., Yu, Y. *J. Phys. Chem. B.* **2005**, *109*, 13375.
- (26) Kolafa, J., Nezbeda, I., Lisal, M. *Mol. Phys.* **2001**, *99*, 1751.
- (27) Aida, T., Inomata, H. *Molecular Simulations* **2004**, *30*, 407.
- (28) Honma, T., Liew, C., Inomata, H., Arai, K. *J. Phys. Chem. A.* **2003**, *107*, 3960.
- (29) Sassiat, P., Mourier, P., Caude, M., Rossiet, R. *Anal. Chem.* **1987**, *59*, 1164.
- (30) Frank, M. J. W., Kuipers, J.A.M., Swaaij, W.P.M. *J. Chem. Eng. Data* **1996**, *41*, 297.
- (31) McCall, D., Douglass, D., Anderson, E. *J. Chem. Phys.* **1959**, *31*, 1555.
- (32) Maddox, M., Goodyear, G., Tucker, S. *J. Phys. Chem. B.* **2000**, *104*, 6248.

CHAPTER 3

MOLECULAR DYNAMICS SIMULATIONS OF PYRENE IN CO₂-EXPANDED METHANOL AND CO₂-EXPANDED ACETONE

3.1 Introduction

Addition of a solvatochromic probe is one method of determining the local molecular environment in gas-expanded liquids (GXLs).^{1,2} Solvatochromism is a pronounced change in the position and/or intensity of an electronic emission or absorption band due to properties of the solvent. Some of the properties determined from solvatochromic shifts of dyes are hydrogen-bonding donating ability, hydrogen bonding accepting ability, polarizability, and local polarity.

Pyrene is a well-known solvatochromic indicator for probing local polarity in the cybotactic region or local environment in solvent systems. Figure 3-1 presents the structure of a pyrene molecule. It is strongly fluorescent, and its emission spectra is sensitive to the local environment. Pyrene emissions have previously been used to study local heterogeneities in near-critical water³, room-temperature ionic liquids⁴, ethylene-co-(Vinyl Acetate) films⁵, micellular environments^{6,7}, and supercritical fluids.⁸⁻¹¹ Pyrene has even been tagged onto the ends of peptide molecules^{12,13} to study end-folding behaviors as well as local environments in aqueous solution and microfibriles.

In this work, UV-vis spectroscopy experiments are combined with molecular dynamics simulations to elucidate the cybotactic region about ground state pyrene in gas-expanded liquids. This is the first attempt at simulating pyrene in gas-expanded liquids, and this is also the first instance of using pyrene as an experimental probe in GXLs.

Pyrene experiments in supercritical fluids have demonstrated heterogeneities in the cybotactic region. Brennecke and Eckert¹⁰ performed fluorescence spectroscopy measurements of dilute pyrene in supercritical CO₂, ethylene, and fluoroform. Local solvent densities around pyrene showed enhancement with respect to the bulk as the critical point was approached. More specifically, Rice, et. al.⁹ have observed local density enhancements 2 to 3 times the bulk density in supercritical CO₂. As the bulk density increased towards liquid-like values, the local density enhancement in the cybotactic region about pyrene decreased.

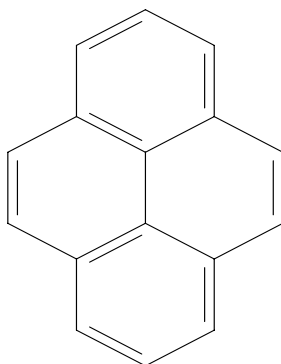


Figure 3-1. Pyrene.

3.2 Pyrene simulations in the literature

Knutson, et. al.¹⁴ were the first to propose a synergy of fluorescence experiments and molecular dynamics simulations to study local density augmentations in supercritical CO₂. Fluorescence experiments at 310.4 K and pyrene concentrations of $x_p=3.2 \times 10^{-8}$ in supercritical CO₂ showed local density enhancements of upto 2.05, and these enhancements are augmented as the bulk density decreases. For the MD simulations, both

pyrene and CO₂ were treated as spherical Lennard-Jonesian particles. The results indeed exhibited density enhancements at 310.4 K of upto 1.8 as the bulk density decreased.

Chialvo and Debenedetti¹⁵ performed molecular dynamics simulations of pyrene-CO₂ and neon-xenon mixtures at approximately 323 K and $\rho_r=0.8$. All molecules were again treated as spherical Lennard-Jonesian particles. The radial distribution function or $g(r)$ (defined in Section 2.5 of Chapter 2) of pyrene-CO₂ interactions showed a broad peak at approximately 6.5 Angstroms. The $g(r)$ peak reached a value of about 2.8, indicating significant pyrene-CO₂ interactions. In order to simulate the cybotactic region around pyrene, however, adequate force fields of pyrene are needed. The development of an all-atom force field for pyrene is described in the next section.

3.3 Force Fields

Carbon dioxide, methanol, and acetone molecules have been modeled as rigid collections of atomic sites with specified fixed charges interacting through pairwise-additive, site-site Lennard Jones and Coulomb forces. Pyrene solute, however, contains an additional intramolecular component, namely valence angle constraints. Equation 3-1 represents the force field in CO₂-methanol-pyrene and CO₂-acetone-pyrene. The first two terms represent the Van der Waals and electrostatic interactions, respectively, while the last term represents the intramolecular valence angle component. The bond angle force constant is noted as K_θ , and θ_0 is the equilibrium angle. The values of these constants were taken from Reference 19.

$$u_{ij} = \sum_i \sum_{j>i} \left[4\epsilon_{ij} \left\{ \left(\frac{\sigma_{ij}}{r_{ij}} \right)^{12} - \left(\frac{\sigma_{ij}}{r_{ij}} \right)^6 \right\} + \frac{q_i q_j}{r_{ij}} \right] + \sum_{angles} \frac{K_\theta}{2} (\theta - \theta_0)^2 \quad \text{Equation 3-1}$$

Carbon dioxide pair interactions have been modeled using the Transferrable Potential for Phase Equilibria or TrAPPE potential.¹⁶ The J2¹⁷ and OPLS-derived potentials¹⁸ have been used for methanol and acetone pair interactions, respectively. Section 2.2 of Chapter 2 presents detailed information about these three potentials. Each of the pairwise potentials specifies a representation for the fixed point charges and these are assumed to remain fixed in the heterogeneous pairwise Coulomb interactions.

An all-atom force field is one where each atom in the molecule is treated explicitly. A united-atom force field is one where certain groups (such as a methyl group) are treated as one entity. Both the J2 and OPLS-derived potentials are united-atom potentials, and the methyl groups are regarded as one entity. United-atom, and especially all-atom, force fields of ground-state pyrene in the literature are very sparse. To the best of the author's knowledge, no united-atom or all-atom excited state force field for pyrene has been published. Sun¹⁹ performed ab initio calculations on alkane and aromatic compounds and optimized the potentials for condensed-phase applications. Explicit pyrene site-charges were not provided. Furthermore, the van-der Waals interactions were treated with a 9-6 rather than a 12-6 potential. A 9-6 potential is one where the repulsion and attraction terms of the Van der Waal equation are raised to the power of 9 and 6, respectively. Even if a 12-6 potential were fitted to the 9-6 potential to obtain Lennard – Jones parameters, the absence of site charges on pyrene would not yield optimal results in a solvent consisting of both Coulombic and Lennard-Jonesian components. Also, Hoff, et.

al.²⁰ simulated pyrene in a lipid membrane using GROMACS software. Their pyrene force field, however, has not yet been published.

Duffy, et. al.²¹ published an OPLS force field for benzene and naphthalene, which specified two different types of carbon atoms: the sp² and sp carbons. All of the hydrogens were treated the same, giving this force-field three different types of atoms for benzene and naphthalene. Cinacchi, et. al.²² then performed simulations of hexakis(pentyloxy)triphenylene or HAT5, a four-ring structure like pyrene with attached *R*-groups. Figure 3-2 shows the HAT5 molecule. The OPLS potential was applied for the aromatic carbons not bonded to the *R*-groups in the HAT5 molecule. Once again, all of the aromatic hydrogens were treated the same.

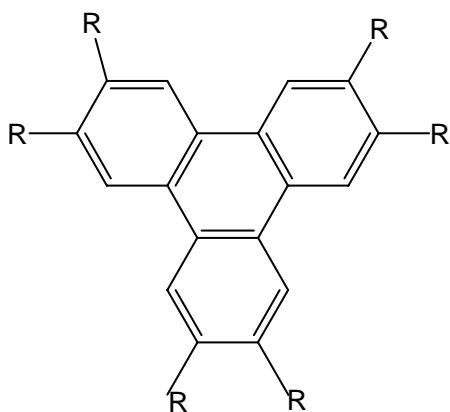


Figure 3-2. HAT5 molecule

In this work, the Optimized Potential for Liquid Simulations or OPLS force field²¹ was employed for the partial charges and Lennard-Jones parameters in pyrene. However, unlike the OPLS force field for aromatics, the potential used in this work specifies five different types of carbons. As shown in Figure 3-3 and Table 3-1, all of the sp² carbons

have a charge of -0.115, while the sp carbons have a charge of zero. The Lennard Jones parameters for all the carbons are the same. Furthermore, there are three types of hydrogens in this pyrene force field, one for each sp² carbon specified. All the hydrogens have a charge of 0.115.

Ab initio calculations using the SPARTAN software package²³ on ground-state pyrene were conducted. The purpose of the ab initio calculations was two-fold: a) to determine the number of different carbons in pyrene b) to compare the resulting atomic site charges from the ab initio calculations to the charges from the OPLS potential of aromatics.¹⁹ Density functional theory with B3LYP functional and 6.31 G* basis set was employed for the ab initio calculations; the calculations were performed in a vacuum. Table 3-1 presents both the number of carbons and charges obtained by the ab initio calculations of ground state pyrene. The charges from the OPLS potential are also tabulated. Figure 3-3 is a cartoon of the different types of carbons, corresponding to the symbols in Table 3-1.

The ab initio calculations produced five different types of carbons: three sp² carbons and two sp carbons. The hydrogens bonded to the sp² carbons are also different from each other, corresponding to the carbon name. For example, the H1s hydrogens are bonded to the C1s carbons. However, all of the hydrogens possessed a partial charge of 0.130, regardless of the carbon it was bonded to. In other words, the H1s hydrogen and the H2s hydrogens all have a charge of 0.130.

The carbon partial charges obtained by density functional theory calculations are relatively close to the -0.115 charge from OPLS potentials. The advantage of using the OPLS potential, however, is that it was optimized to reproduce experimental

thermodynamic properties such as heats of vaporizations and densities. The number of charges ultimately used in the calculations was 4. For simplicity, the C5s carbon obtained through the ab initio calculations was treated as a C3s carbon in the MD simulations.

The Lennard-Jones cross-term parameters for MeOH-MeOH and acetone-acetone interactions are handled by the mixing rule specified by the respective potentials. The Lennard-Jones cross-term parameters for MeOH-CO₂, acetone-CO₂, and CO₂-CO₂, pyrene-CO₂, pyrene-acetone, and pyrene-methanol interactions, however, are handled by the Lorentz-Berthelot mixing rule, uniformly. Tables B1 and B4 of Appendix B provide tables of force field parameters for both pyrene-CO₂-methanol and pyrene-CO₂-acetone simulations. Furthermore, Section II of Appendix B provides partial charges of the excited-state of pyrene from preliminary Q-Chem calculations.²⁴

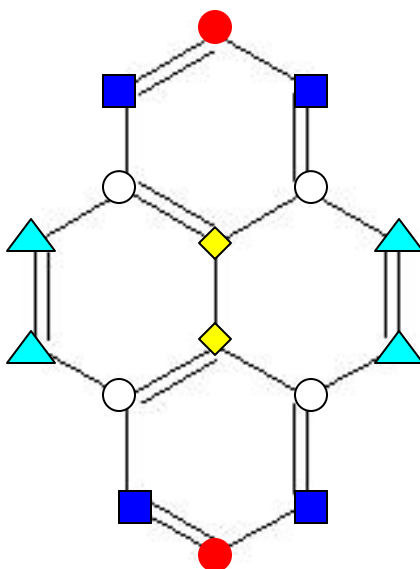







Figure 3-3. Pyrene partial charges and number of carbon types from ab initio calculations.

Table 3-1. Results of the ab initio calculations performed on pyrene. The first column displays the symbol of the specific carbon atom. The symbols in this table correspond to the symbols in Figure 3-3. The second column presents the name of the specific carbon atom. The third column displays the charges produced by the ab initio calculations, while the fourth column displays the charges taken from the Optimized Potential for Liquid Simulations or OPLS potential.²¹

Symbol	Carbon name	q (e) from ab initio calculations	q (e) from OPLS Potential
	C1s	-0.122	-0.115
	C2s	-0.226	-0.115
	C3s	0.164	0
	C4s	-0.195	-0.115
	C5s	-0.012	Is a C3s Carbon q=0

3.4 Simulation Details

The mole fractions, densities, and temperature for the pyrene-acetone-CO₂ and pyrene-methanol-CO₂ GXL systems investigated here are reported in Table 3-2. Molecular dynamics (MD) simulations were carried out using the DL_POLY Software package.²⁵ Regardless of the relative composition, each simulated system box is populated by a total of 1001 molecules (i.e. one pyrene solute molecule is simulated in 1000 solvent/cosolvent molecules). Cubic periodic boundary conditions are used throughout, but the length of the system box is scaled to preserve the specified density as per Table 3-2. Typical box lengths are on the order of 20-50 Å, and more specifically 40-50 Å for the GXL systems simulated. Because of the cubic boundary conditions, the potential interactions must necessarily be cut off to less than or equal to half the box length. Coulombic interactions are handled by the Ewald summation method with automatic parameter optimization (by DL_POLY). The equations of motion were integrated using the velocity verlet algorithm as implemented by DL_POLY using time steps of 1.0 femtosecond. Structural information (at equilibrium) has been obtained using the NVT (constant moles, constant volume, and constant temperature) ensemble with a Nose-Hoover thermostat in which the relaxation constant is set to 0.3.

Equilibrium averages have been obtained as follows: Initial configurations are equilibrated for 50 picoseconds of NVT simulation during which statistics are not collected. This is immediately followed by a 300 picoseconds NVT simulation during which statistics are obtained to determine equilibrium structural information.

Table 3-2. GXL conditions used for simulations at T=313 K. CO₂-Methanol liquid densities are predicted from the Peng-Robinson equation of state. CO₂-Acetone values are measured from experiment.²⁶

GXL	x _{CO2}	P(bar)	ρ^L (kg/m ³)
CO ₂ -Methanol	0.2	36	851.4
CO ₂ -Methanol	0.5	66	920
CO ₂ -Methanol	0.8	72	857
CO ₂ -Methanol	0.9	75	739.1
CO ₂ -Acetone	0.2	15	789.5
CO ₂ -Acetone	0.5	35	812.4
CO ₂ -Acetone	0.8	63	830.0
CO ₂ -Acetone	0.9	73	828.7

3.5 Results

3.5.1. Experimental background : CO₂-Methanol-Pyrene

UV-vis spectroscopy was performed with a Hewlett-Packard 8453 spectrophotometer. The measurements were performed using a high-pressure 10 mL cylindrical cell with quartz windows set to a pathlength of 1 cm. The cell was jacketed with a heating block and equipped with a pressure gauge, thermocouple, and magnetic stir bar. Pyrene (Aldrich) was first dissolved in methanol (Aldrich) to get the desired concentration of 10^{-5} mol/L. Carbon dioxide was introduced into the temperature-controlled cell (set at 313 K) to a desired pressure via an Isco 260 Syringe Pump.

By noting the difference in volume of the pump combined with determining the density of CO₂ from the Span-Wagner equation of state²⁷, the amount of CO₂ added is calculated. Both vapor and liquid phases were present and the meniscus was above the cell window. It was assumed that the dilute concentration of pyrene solute had no effect on the CO₂-methanol phase behavior. Liquid phase concentrations were fit to published literature data.

The absorbance spectra of pyrene shows two peaks: one peak at around 311 nm and another peak at around 325 nm. The shift in peak position is a solvatochromic phenomenon dependent on solvent. Figure 3-4 displays the maximum wavelength or lamda of pyrene absorption in CO₂-expanded methanol versus mole fraction CO₂. Lamda decreases slowly until 0.4 CO₂ mole fraction, after which it decreases rapidly. The figure suggests that CO₂ penetrates the cybotactic region of pyrene with CO₂ addition. In other words, the local environment around the pyrene molecule looks more and more like CO₂ as CO₂ is added.

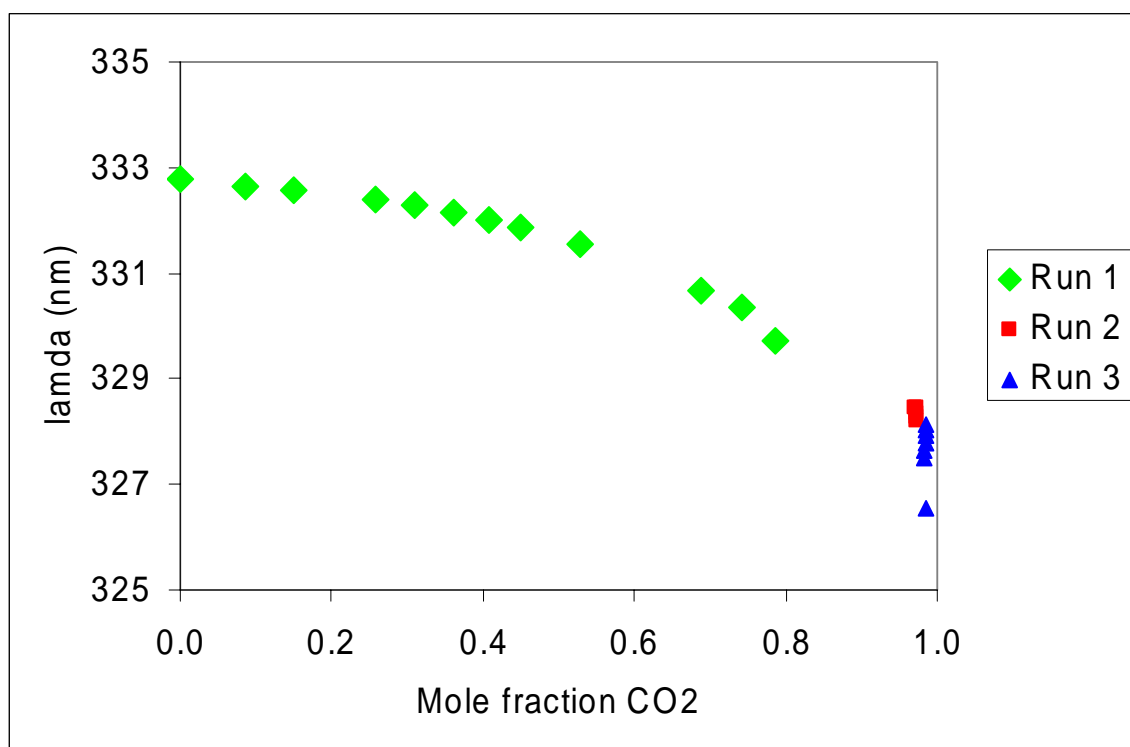


Figure 3-4. Lambda (peak position) of pyrene absorbance versus mole fraction CO₂ in CO₂-expanded methanol; T=313 K.

For comparison, Figure 3-5 shows excited state fluorescence data of pyrene in CO₂-expanded methanol, acetone, and acetonitrile. Pyrene has a total of 5 characteristic vibronic bands in its emission spectrum. The intensity of the first band is strongly dependent on solvent polarity, while that of the third band is insensitive to the local solvent polarity.²⁸ The ratio of the first to the third band ($Py = I_1/I_3$) or the Py scale ratio thus changes with solvent polarity, becoming a tool to probe the polarity of the immediate environment around a pyrene molecule.

As shown in Figure 3-5, the Py scale value decreases steadily in CO₂-methanol upto 0.6 CO₂ mole fraction, after which it decreases rapidly. The Py scale value in CO₂-expanded methanol starts at around 1.05 in pure methanol and steadily decreases to around 0.7 in pure CO₂. This indicates that the local polarity around pyrene decreases about 30% from pure methanol to pure CO₂. The result of this decrease in local polarity is most likely due to CO₂ molecules penetrating the cybotactic region of pyrene. If methanol molecules clustered around pyrene with added CO₂ pressure, this would result in an increase in the Py scale ratio. Methanol molecules contain a dipole moment, while CO₂ molecules do not contain an overall dipole moment. Hence, an increase in the local polarity can only be due to the local presence of methanol molecules. Furthermore, Figure 3-5 indicates that the local polarity around excited state pyrene decreases with added CO₂ for all three gas-expanded liquids – CO₂ methanol, CO₂ – acetonitrile, and CO₂-acetone..

To summarize, Figure 3-4 shows UV-vis absorbance data of ground state pyrene, while Figure 3-5 shows fluorescence spectroscopy data of excited state pyrene. Both

Figure 3-4 and Figure 3-5 indicate that the cybotactic region around pyrene in CO₂-expanded methanol looks more and more like CO₂ as CO₂ is added.

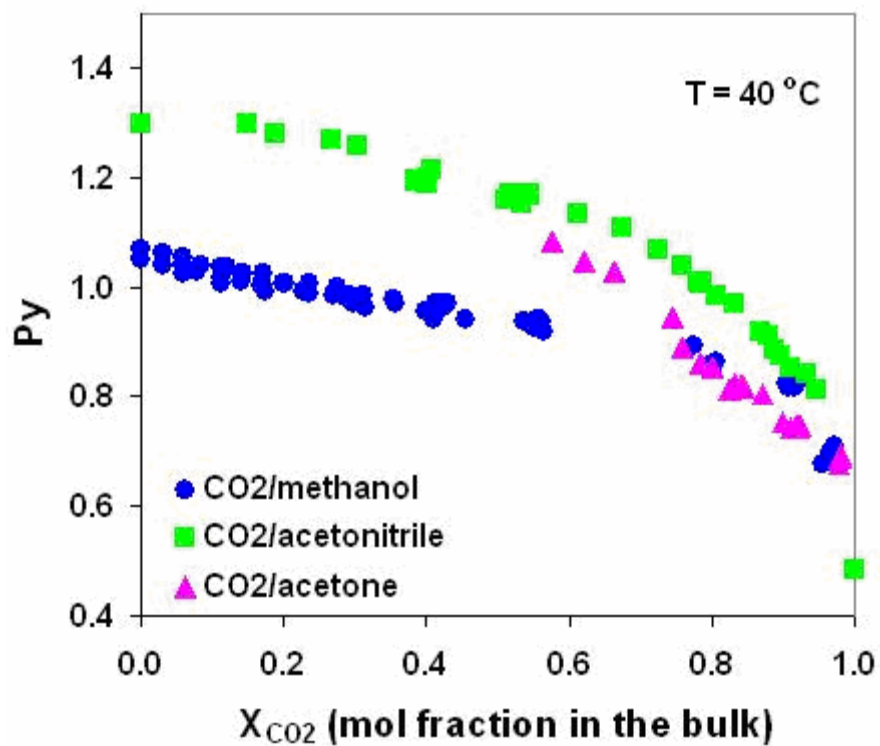


Figure 3-5. Py scale ratio vs. mole fraction CO₂ for CO₂-methanol, CO₂-acetone, and CO₂-acetonitrile; T=313 K.

3.5.2. *Simulation results in supercritical CO₂*

Pyrene is simulated in pure CO₂ at 313 K to assess the accuracy of the force field. Figure 3-6 displays the ratio of the local density to bulk density (or local density enhancement) around pyrene versus the reduced density of supercritical CO₂. Above a reduced density of 0.7, the simulations agree well with experiments. However, the simulations display a maximum at a reduced density of 0.5, a result consistent with UV-vis spectroscopy data obtained by Bright and coworkers.⁹ At high reduced densities, carbon dioxide is liquid-like, so the local density looks like the bulk density. As the reduced density decreases beyond the critical density, the density fluctuations persist for longer and longer time. At one point the persistence time of the density fluctuations reach a maximum, and this is where one sees the greatest local density enhancement. Reducing the density even further basically creates an ideal CO₂ gas. The density is very low, persistence times of the density fluctuations decrease rapidly, and thus the local density enhancement also decreases.

Because the simulations show good agreement with experiments, the pyrene force field was applied in simulations of pyrene in CO₂-expanded methanol and pyrene in CO₂-expanded acetone systems.

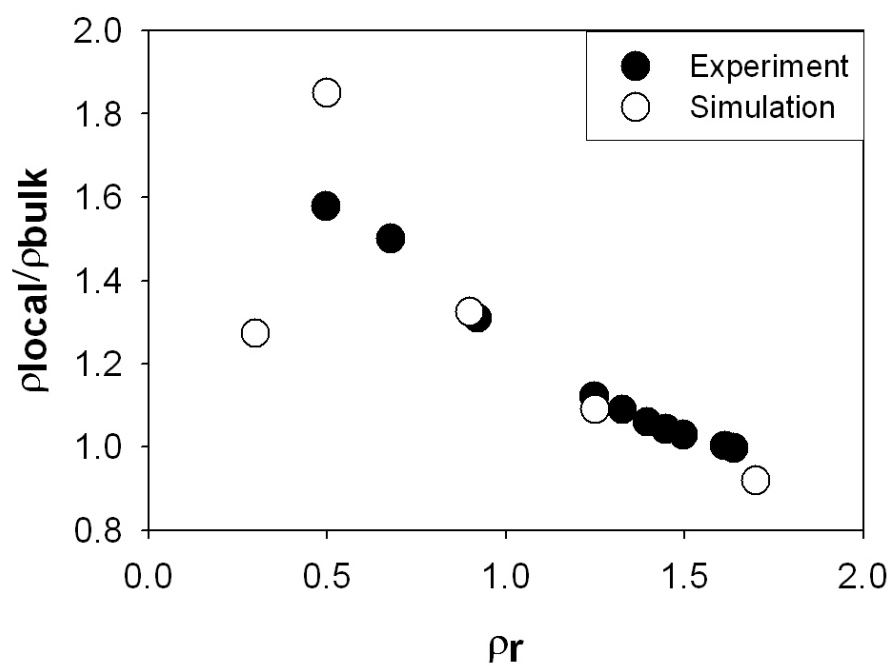


Figure 3-6. Ratio of local density to bulk density of supercritical CO₂ around pyrene versus reduced density. T=313 K

3.5.3 Simulation results in pyrene- CO_2 -MeOH

3.5.3.1. Carbon dioxide-pyrene interactions

Carbon dioxide structure in the vicinity of pyrene is characterized in this work by the C4s-C_g radial distribution function. As shown in Figure 3-7, the C4s carbons of pyrene are the four sp^2 carbons on the side of the molecule. The C4s-C_g radial distribution function was chosen because of better statistics due to averaging over four carbons.

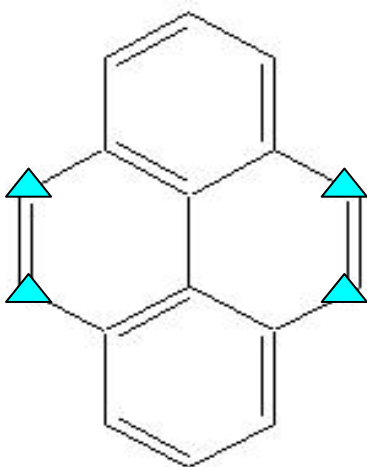


Figure 3-7. C4s carbons on simulated pyrene molecule.

Figure 3-8 presents the C4s-C_g radial distribution function or $g(r)$ in CO_2 -expanded methanol at 15, 35, 63, and 73 bars. The $g(r)$ shows two broad peaks at 4.5 Å and 8 Å with peak heights of approximately 1.2 and 1.1, respectively. The first peak means that the probability of finding a C_g atom 4.5 Å from the C4s atom-probe is 1.2 times greater than random. The peak heights do not change significantly with added CO_2 pressure. Figure 3-9 is a contour plot of the C4s-C_g two-dimensional radial distribution function or $g(r,\theta)$ at $x(\text{CO}_2)=0.8$ and $P=63$ bar. Section 2.5 of Chapter 2 rigorously defines $g(r,\theta)$.

Here, the angle θ is defined as the angle between the C4s atom to the center of mass and the vector from the probe C4s atom to a given C_g in the cybotactic region. Regions of highest probability are at around 4.5 Å and 70° as well as 4.5 Å and 150°.

Figure 3-10 is a schematic of the most probable orientation of C_g atoms around the C4s carbons of pyrene based on the C4s-C_g orientational distribution function shown in Figure 3-9. This cartoon is very approximate, and shows the structure around only one of the C4s atoms. First, the coordinate axis is redefined. The y-axis is the vector from the chosen C4s atom to the center of mass of pyrene, and the x-axis is perpendicular to the y-axis. The angle θ is the angle beginning from the y-axis, and this angle can attain a maximum of 180°. As detailed in Section 2.5, the positions are averaged over the ϕ angle around the y-axis. As shown in Figure 3-10, C_g atoms are placed at $\theta = 70^\circ$ and $\theta = 150^\circ$ with respect to the coordinate system in the cybotactic region defined by a radius of 4.5 Å. It is important to mention here that the figure is plotted on a two-dimensional surface; the actual positions of the C_g atoms are not necessarily in the same plane of the pyrene molecule.

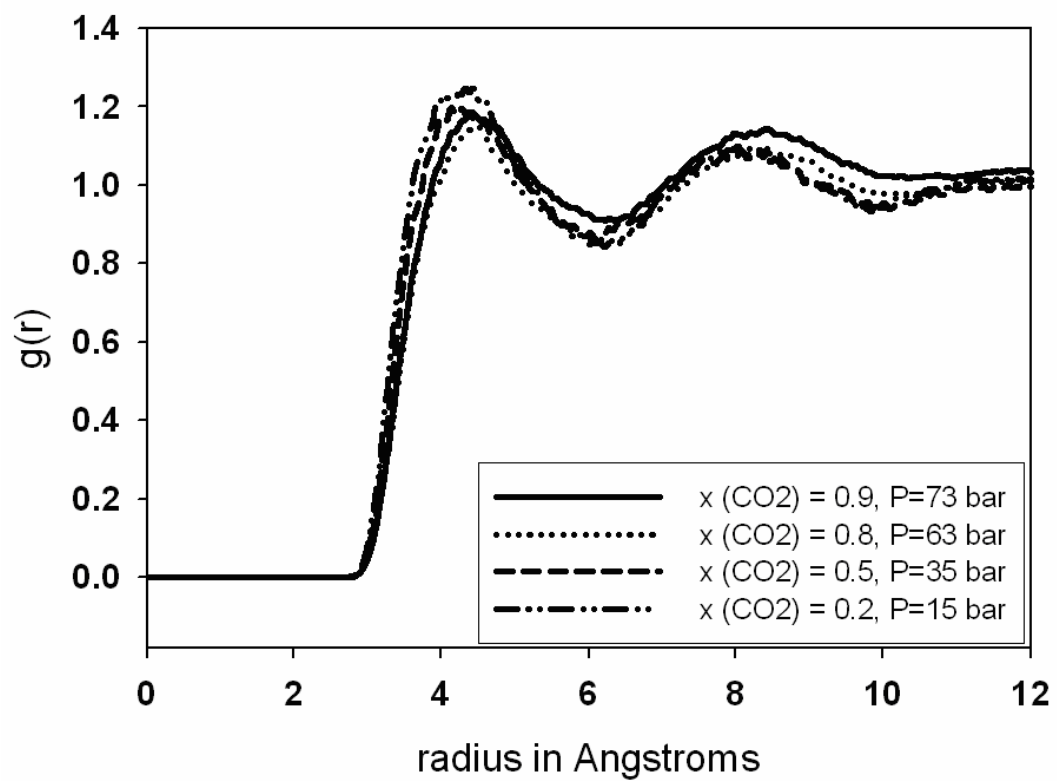


Figure 3-8. Radial distribution functions for C4s-C_g in CO₂-expanded methanol; T=313 K.

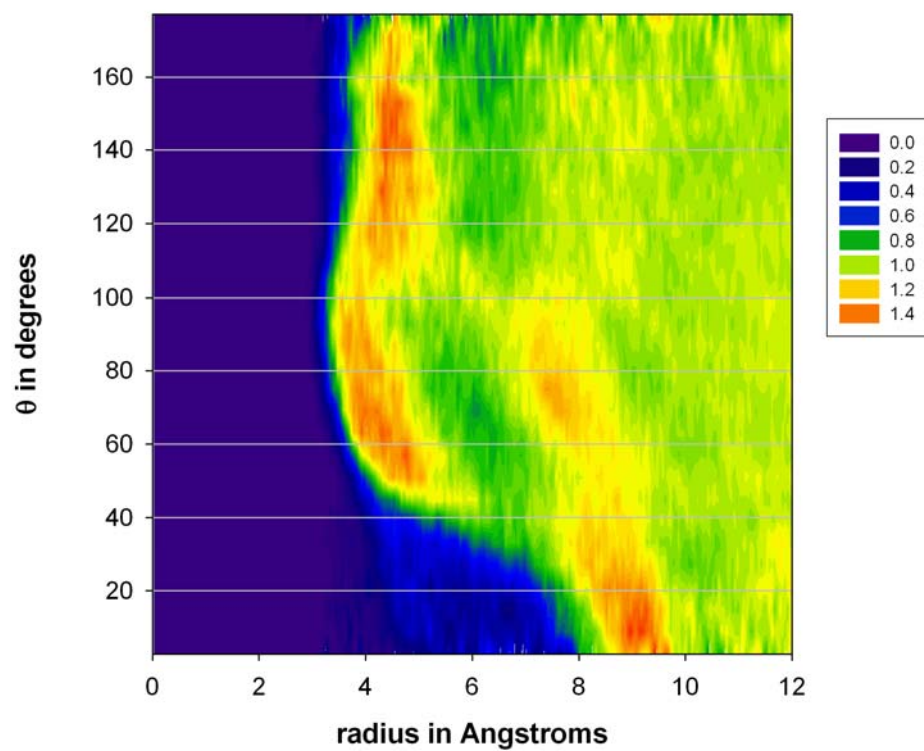


Figure 3-9. Contour plot of C4s-C_g two-dimensional radial distribution function or $g(r, \theta)$ in CO₂-expanded methanol at $x(\text{CO}_2)=0.8$ and $P=63$ bar. The legend shows gradations of $g(r, \theta)$. $T=313$ K.

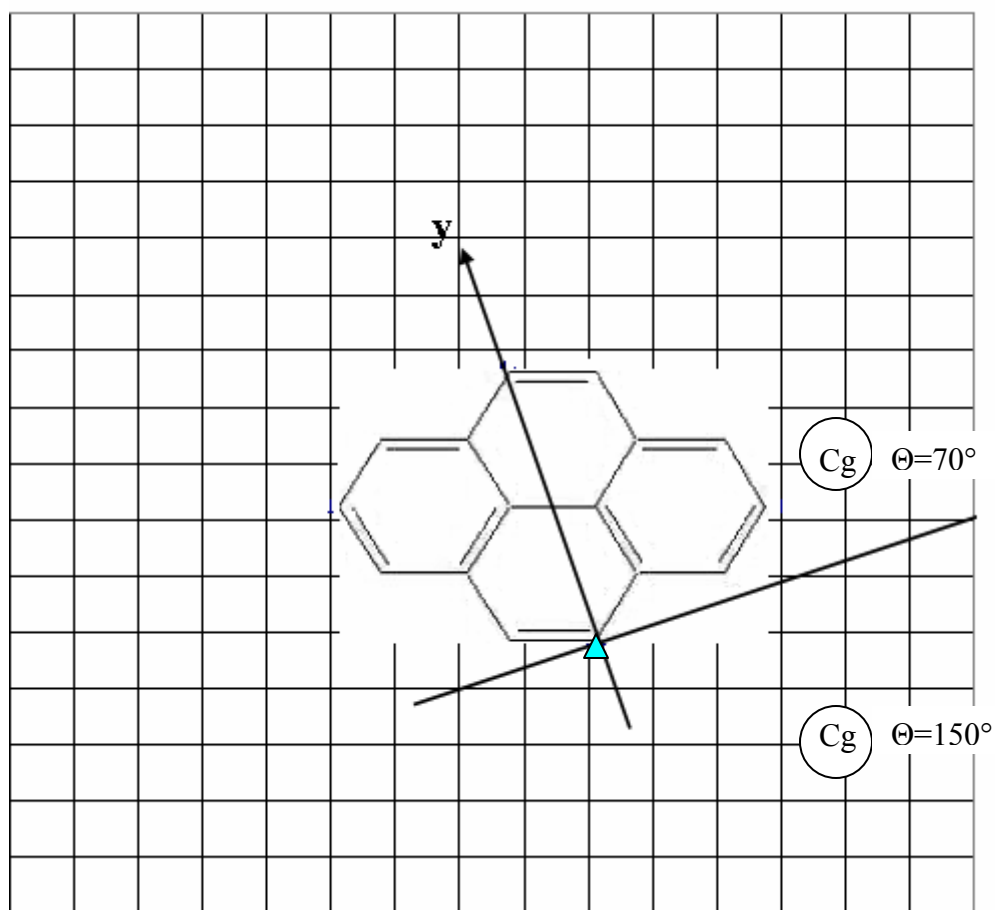


Figure 3-13. Most probable orientation of C_g atoms around the C_{4s} atoms of pyrene in the cybotactic region defined by a radius of 4.5 Angstroms. Positions based on Figure 3-12 and averaged over the ϕ angle around the y-axis; T=313 K.

3.5.3.2 Methanol-pyrene interactions

Methanol structure in the vicinity of pyrene is characterized in this work by the C4s-H_m radial distribution function. Figure 3-11 displays the radial distribution function or g(r) of C4s-H_m interactions in CO₂-expanded methanol. The g(r) shows a peak of 1.1 at close to 10 Å. A much smaller peak can be observed at 4.5 Å with a peak height of 0.7. Again, the C4s-H_m interactions do not change significantly with CO₂ addition. Figure 3-12 is a contour plot of the C4s-O_m two-dimensional radial distribution function. The angle θ is defined as the angle between the C4s atom to the center of mass and the vector from the probe C4s atom to a given O_m atom in the cybotactic region. High probability density regions are at around 5 Å and $\theta < 70^\circ$.

Figure 3-13 is a schematic of the most probable orientation of O_m atoms around the C4s carbons of pyrene based on the C4s-O_m orientational distribution function shown in Figure 3-12. This cartoon is very approximate, and shows the structure around only one of the C4s atoms. First, the coordinate axis is redefined. The y-axis is the vector from the chosen C4s atom to the center of mass of pyrene, and the x-axis is perpendicular to the y-axis. The angle θ is the angle beginning from the y-axis, and this angle can attain a maximum of 180°. As detailed in Section 2.5, the positions are averaged over the ϕ angle around the y-axis. It is important to mention here that the figure is plotted on a two-dimensional surface; the actual positions of the C_g atoms are not necessarily in the same plane of the pyrene molecule. For simplicity, $\theta = 20^\circ$ and $\theta = 50^\circ$ are displayed as representatives of the locus of angles less than 70°. It is important to mention here that the figure is plotted on a two-dimensional surface; the actual positions of the C_g atoms

are not necessarily in the same plane of the pyrene molecule. As shown in Figure 3-13, O_m atoms are placed at $\theta = 20^\circ$ and $\theta = 50^\circ$ with respect to the coordinate system.

Figure 3-14 attempts to combine the schematic plots of Figure 3-10 and 3-13 to show half of the cybotactic region around pyrene. Figure 3-14 does not represent the local composition, *but the relative placement of C_g and O_m atoms with respect to a specified coordinate system*. It is important to note that the C4s atoms on the other side of the fixed pyrene molecules also form a coordinate system that shares the same y-axis and is parallel to the plotted x-axis. The orientational distribution functions shown in Figure 3-9 and 3-12 are averaged over all four C4s carbons, so in fact, all of these four carbons are identical. This new coordinate system will fill in the second half of the cybotactic region around pyrene. Again, it is important to mention here that the figure is plotted on a two-dimensional surface; the actual positions of the C_g atoms are not necessarily in the same plane of the pyrene molecule.

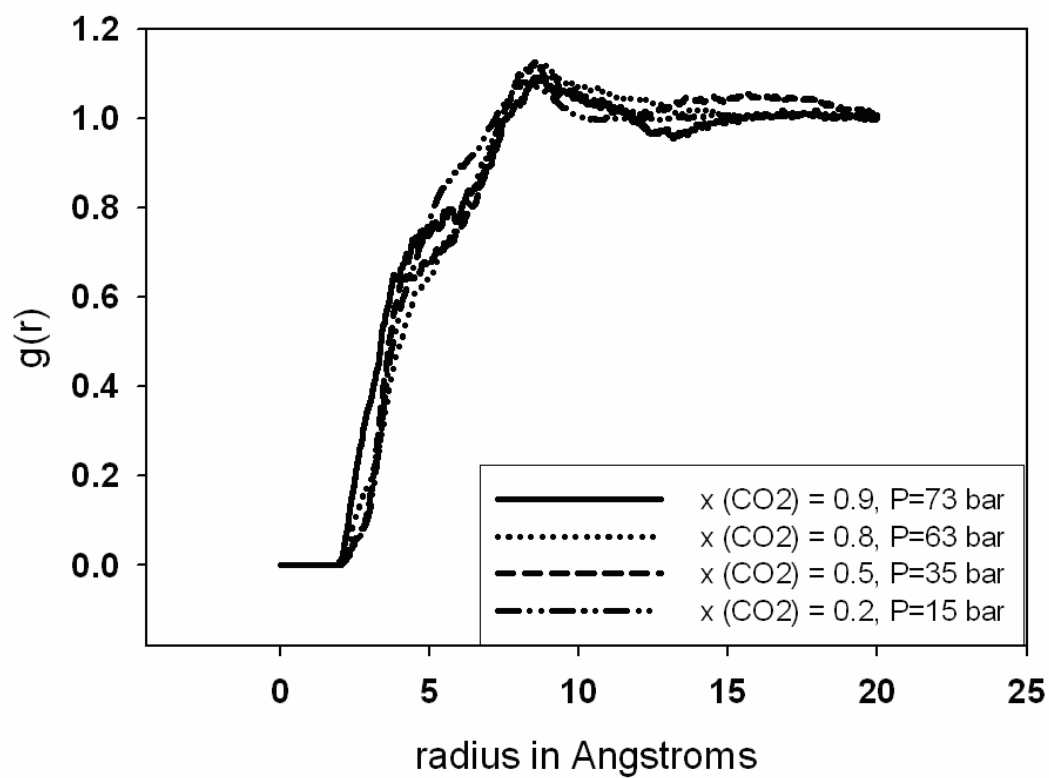


Figure 3-11. Radial distribution functions for C4s-H_m interactions in CO₂-expanded methanol; T=313 K.

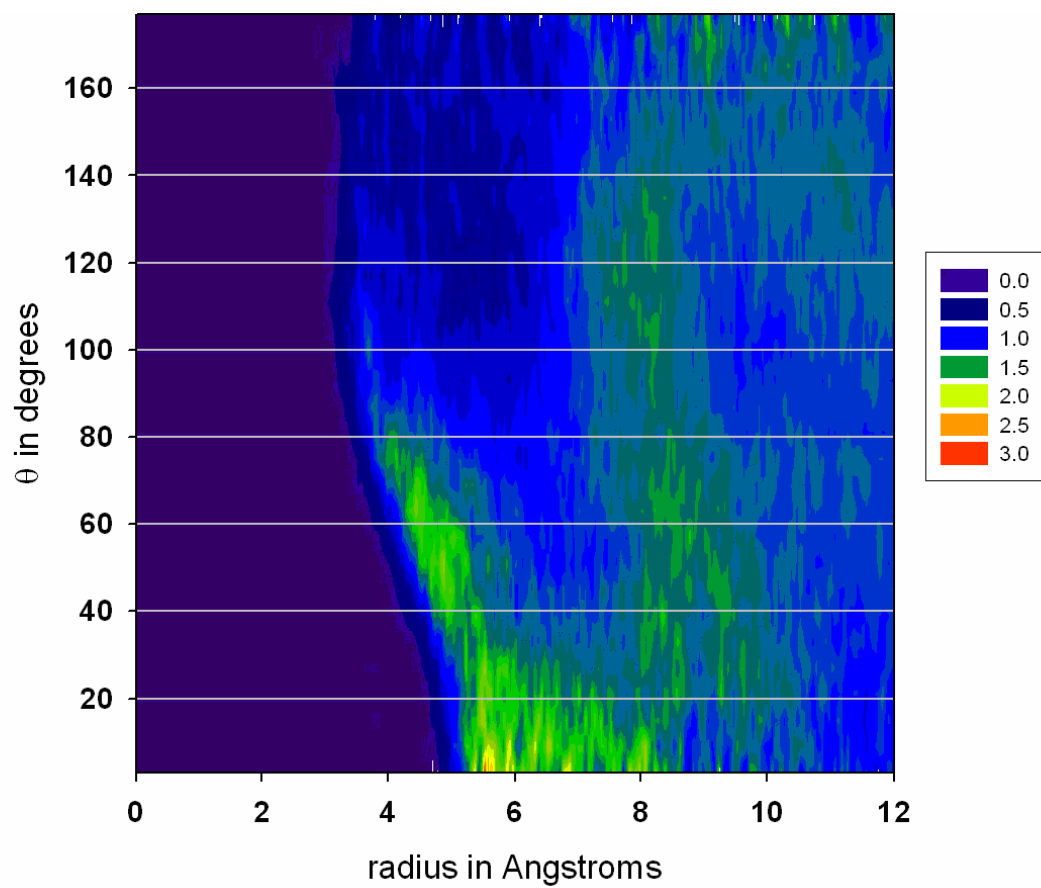


Figure 3-12. Contour plot of C4s-O_m two-dimensional radial distribution function or $g(r, \theta)$ in CO₂-expanded methanol at $x(\text{CO}_2)=0.8$ and $P=63$ bar. The legend shows gradations of $g(r, \theta)$. $T=313$ K.

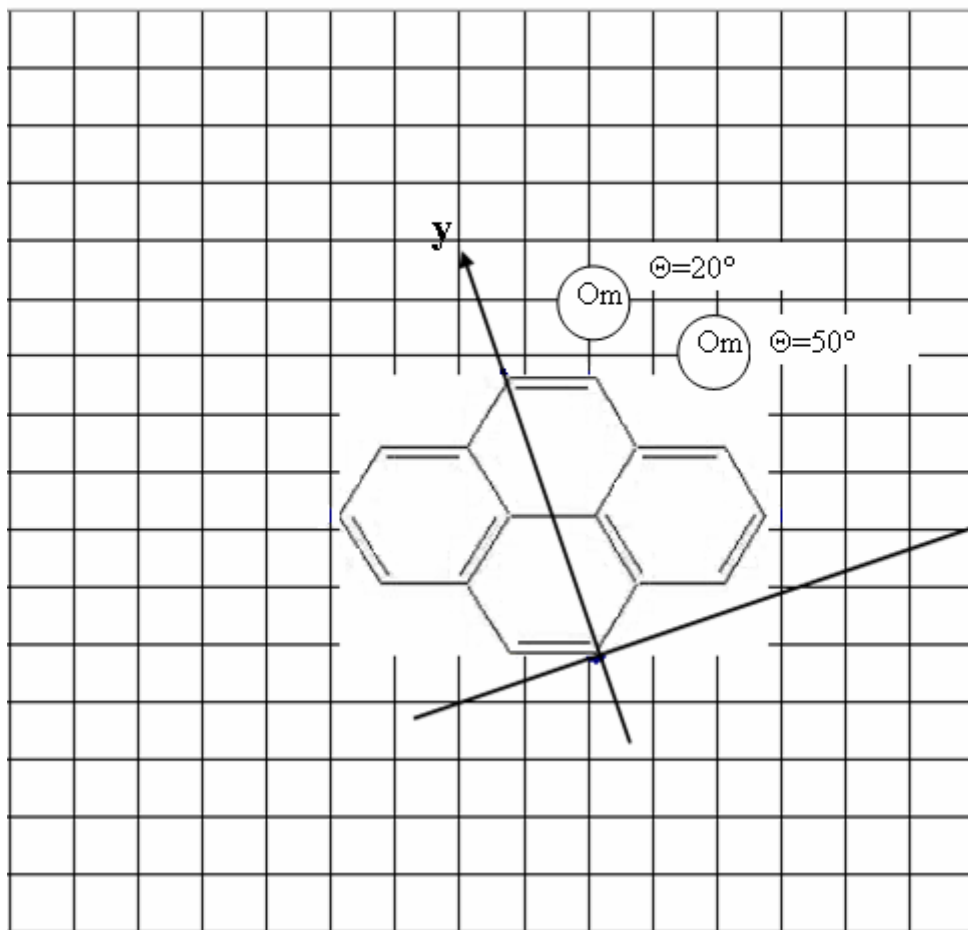


Figure 3-13. Most probable orientation of O_m atoms around the C_{4s} atoms of pyrene in the cybotactic region defined by a radius of 5 Angstroms. Positions based on Figure 3-12 and averaged over the ϕ angle around the y -axis; $T=313$ K.

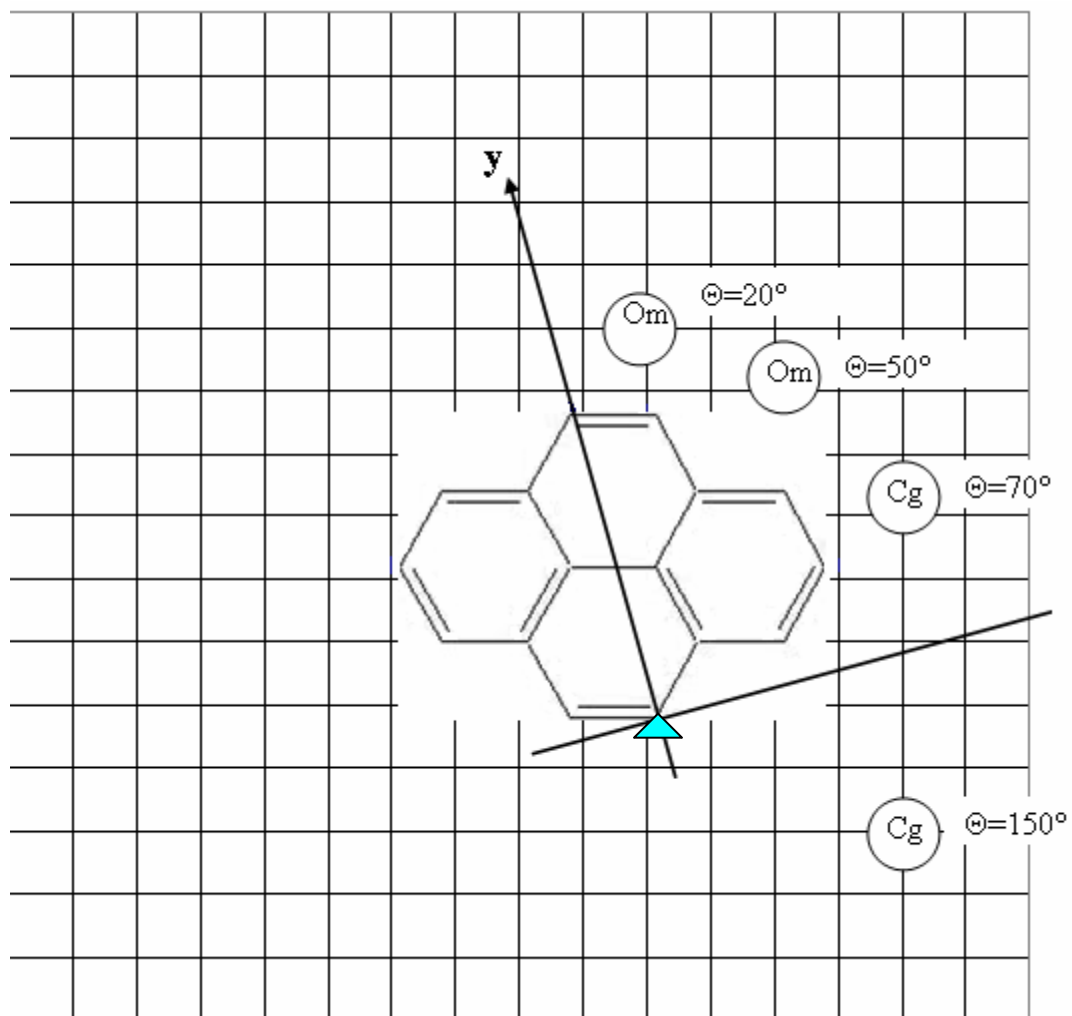


Figure 3-14. Most probable orientation of O_m and C_g atoms around the C_{4s} carbons of pyrene based on a combination of Figures 3-10 and 3-13; $T=313$ K.

3.5.4. Simulation results in pyrene-CO₂-Acetone

The acetone structure in the vicinity of pyrene is characterized in this work by the C4s-C_a radial distribution function. Figure 3-15 displays the C4s-C_a radial distribution function or $g(r)$ in CO₂-expanded acetone at 15, 35, 63, and 75 bar. Two broad peaks are observed at 5 Å and 9 Å. The first peak at 5 Å increases from around 1.1 at 15 bars to around 1.8 at 73 bars. This suggests significant increase in local structure of acetone around pyrene. Unlike the pyrene-methanol radial distribution function from CO₂-expanded methanol simulations shown in Figure 3-11, the $g(r)$ s in Figure 3-15 increase with added CO₂ pressure. Because acetone molecules do not cluster significantly in CO₂-expanded acetone (as presented in Chapter 2), the acetone molecules are more “free” to interact with CO₂ and pyrene. UV-vis data of pyrene in CO₂-expanded acetone are not available, because it is very difficult to solubilize pyrene in CO₂-expanded acetone. Figure 3-15, however, shows the change in the cybotactic region around pyrene in an aprotic solvent.

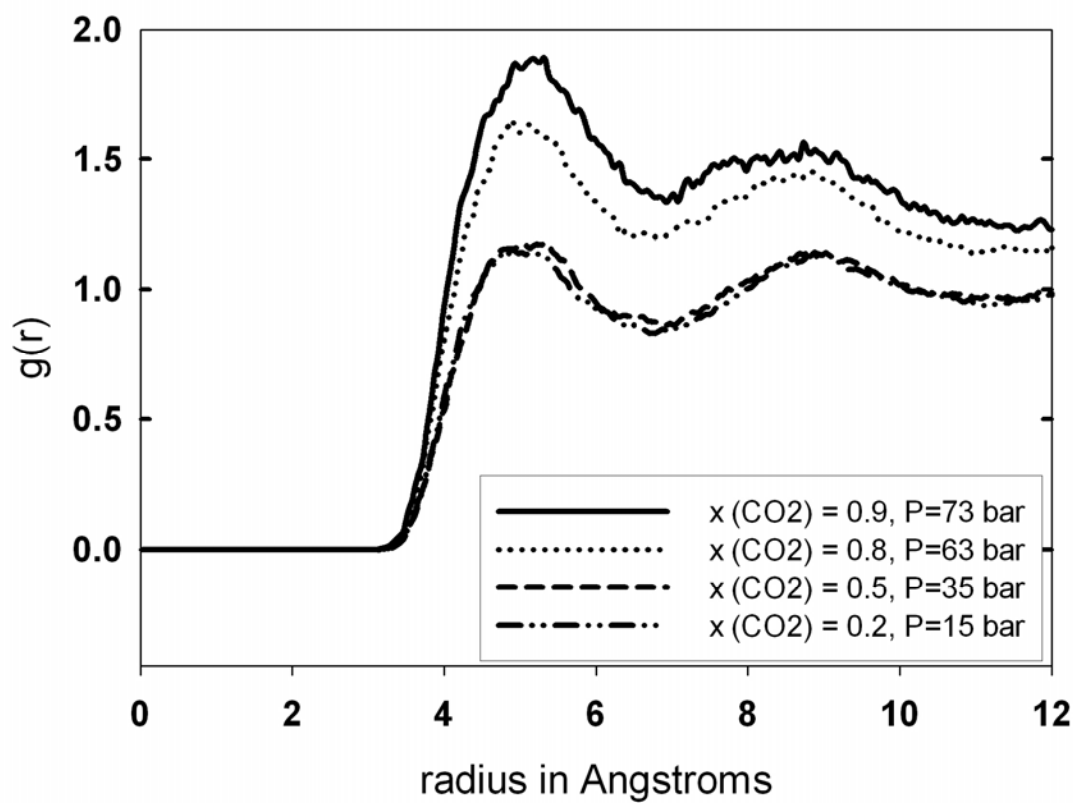


Figure 3-15. Radial distribution functions for C4s-C_a interactions in CO₂-expanded acetone; T=313 K.

3.5.5. Local Compositions in CO₂-expanded methanol and CO₂-expanded acetone

The local composition, or x_{loc} , of the organic component (methanol or acetone) around pyrene may be defined as the following²⁹:

$$x_{loc}^{methanol}(R_{cut}) = \frac{\bar{N}_{methanol}(R_{cut})}{\bar{N}_{TOT}(R_{cut})} \quad \text{Equation 3-2}$$

where $\bar{N}_{methanol}(R_{cut})$ is the average number of particles of methanol within pyrene's solvent sphere of radius R_{cut} . R_{cut} is chosen as the minimum after the first peak in the radial distribution function, as suggested by Tucker and coworkers.³⁰ $\bar{N}_{TOT}(R_{cut})$ is the total number of carbon dioxide and methanol molecules within R_{cut} . $\bar{N}_{methanol}(R_{cut})$ is defined by the following equation:

$$\bar{N}_{methanol}(R_{cut}) = 4\pi \frac{N_{bulk}}{V} \int_{\sigma_{exc}}^{R_{cut}} g(r) r^2 dr . \quad \text{Equation 3-3}$$

Here N_{bulk} is the total number of bulk particles and V is the volume of the simulation box. The excluded radius, denoted by σ_{exc} , is that radius where $g(r)$ first acquires a non-zero value in the simulation output.

Figure 3-16 displays the local composition of methanol around pyrene in CO₂-expanded methanol, and Figure 3-17 displays the local composition of acetone around pyrene in CO₂-expanded acetone at 313 K. The local composition of the organic decreases with added CO₂ pressure for both systems, which suggests that CO₂ is penetrating the cybotactic region of pyrene with added CO₂ pressure. In other words, the cybotactic region looks more and more like CO₂ as CO₂ is added, a result consistent with UV-vis absorption experiments shown in Figure 3-4.

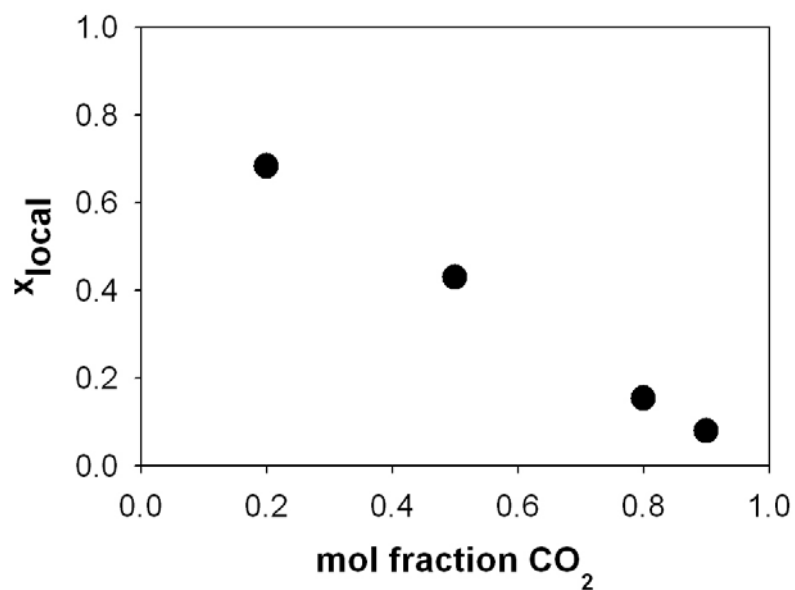


Figure 3-16. Simulated local composition of methanol around pyrene vs. bulk CO_2 mole fraction in CO_2 -expanded methanol. $T=313\text{ K}$

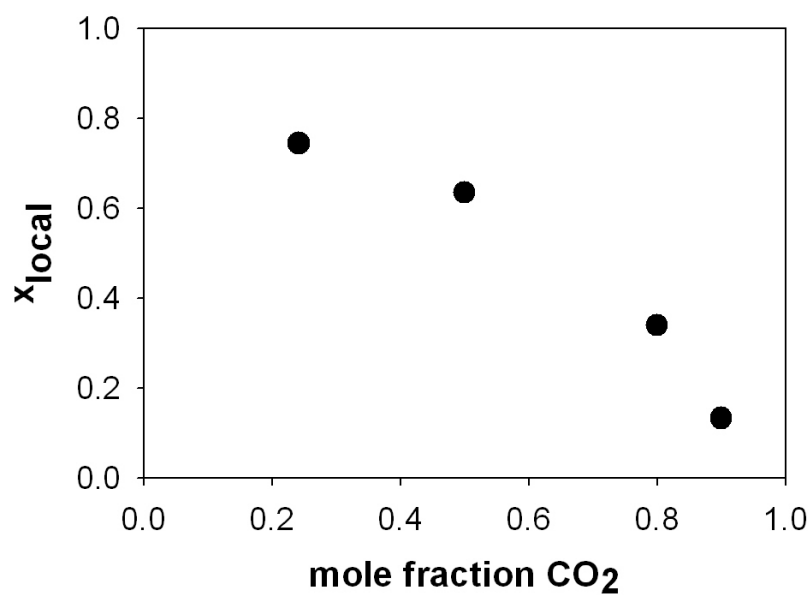


Figure 3-17. Simulated local composition of acetone around pyrene vs. bulk CO_2 mole fraction in CO_2 -expanded acetone. $T=313\text{ K}$

Figure 3-18 displays the simulated local composition of methanol around pyrene versus the bulk composition of methanol in CO₂-expanded methanol, whereas Figure 3-19 displays the simulated local composition of acetone around pyrene versus the bulk composition of acetone in CO₂-expanded acetone. The $y=x$ line is plotted as a baseline. As shown in Figure 3-18, the simulated local composition of methanol around pyrene falls below the bulk value. The local composition of acetone around pyrene, however, is greater than the bulk composition as shown in Figure 3-19. Thus, the simulation results show local density enhancements around pyrene in CO₂-expanded acetone, but not in CO₂-expanded methanol.

Figures 3-18 and 3-19 show the significance of solute-solvent interactions in local composition enhancements. Because the acetone molecules do not cluster in CO₂-expanded acetone, they are more available to interact with pyrene. Methanol molecules, however, prefer to cluster in CO₂-expanded methanol. The potential used in this work consists of Lennard-Jones and Coulombic terms. The data suggests that the current force field for ground-state pyrene may not be enough to attract methanol molecules in CO₂-expanded methanol. As discussed in the next section, a polarization component is needed to better represent the interactions between methanol and pyrene.

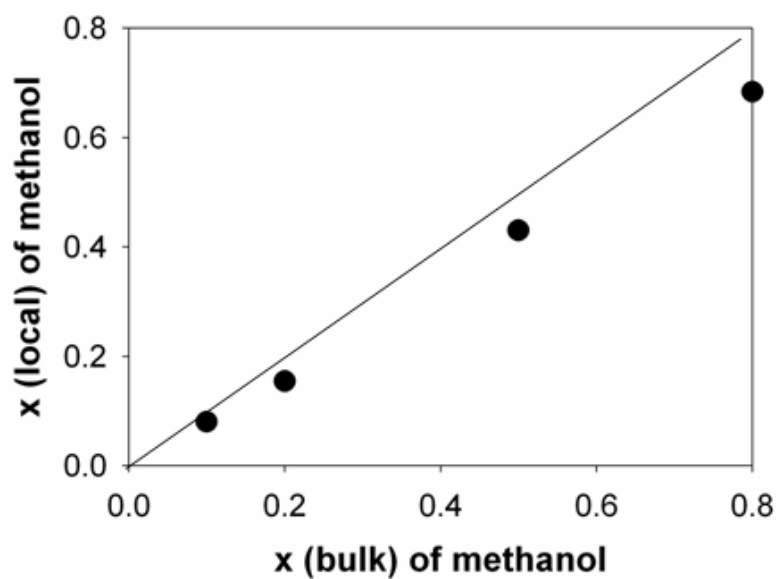


Figure 3-18. Simulated local composition of methanol around pyrene vs. bulk composition of methanol in CO₂-expanded methanol. T=313 K

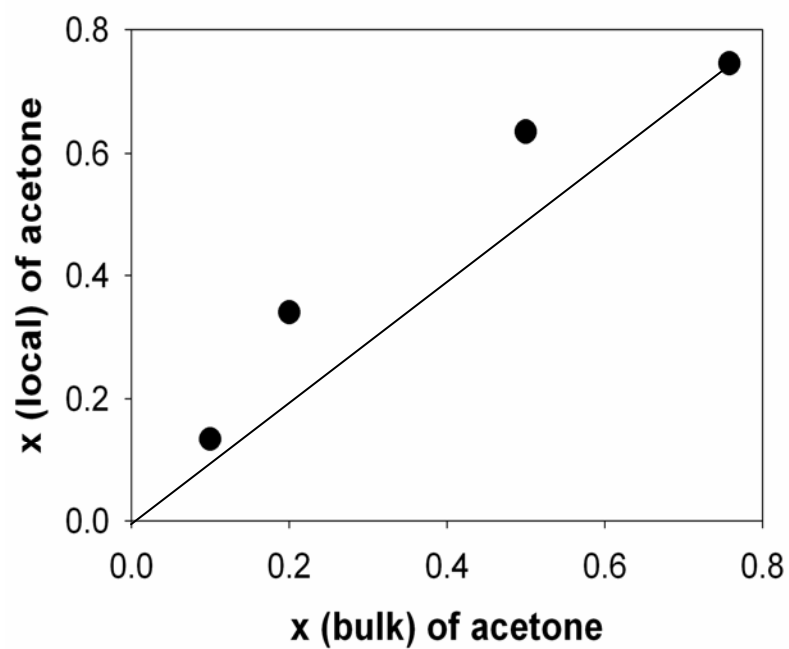


Figure 3-19. Simulated local composition of acetone around pyrene vs. bulk composition of acetone in CO₂-expanded acetone. T=313 K

3.6 Discussion

Figure 3-11 shows very little structure of methanol molecules around pyrene in CO₂-expanded methanol. In the real system, the pi electrons of pyrene may attract a lone, protic hydrogen in a methanol cluster. However, the simulations in this work do not treat the pi electrons explicitly. In other words, there is no polarizability component to the force field. As methanol approaches pyrene, the simulations in this work provide no treatment of reorganization of the pi electrons in pyrene. This induced dipole (and not the electrostatic interactions between methanol and pyrene) will be the salient force of interaction between methanol and pyrene. This is because the partial charge of a carbon atom in pyrene is -0.115, while the partial charge of the protic hydrogen in methanol is 0.435. This is a relatively strong electrostatic interaction. However, the partial charge of the oxygen in methanol is -0.7, about seven times more basic than the carbon in pyrene. Thus, the electrostatic interaction between the protic hydrogen of methanol and the oxygen in methanol is stronger, and the methanol molecules will cluster. In conclusion, a polarizability component to the pyrene simulations in gas-expanded methanol may be necessary to fully capture the interactions in the cybotactic region. Section 5.3 in Chapter 5 proposes a method to incorporate the polarizability term into the force field.

Figure 3-16 displays the simulated local composition of methanol in CO₂-expanded methanol, and Figure 3-17 displays the simulated local composition of acetone in CO₂-expanded acetone. The local compositions of both organics decrease with added CO₂ mole fraction. In other words the local mole fraction of CO₂ increases as CO₂ increases. This finding is consistent with UV-vis absorption results of ground state

pyrene in CO₂-expanded methanol shown in Figure 3-4. However, the local composition of methanol decreases linearly, while the local composition of methanol decreases more parabolically. The reason for this can also be due to an inaccurate force. Lack of a polarizability term cannot keep the methanol molecules in the cybotactic region of pyrene due to weak pyrene-methanol interactions.

Figure 3-15 shows an *increase* in the C4s-C_a radial distribution function with added CO₂ pressure, but the local composition of acetone in CO₂-expanded acetone *decreases* with added CO₂ pressure. Table 3-3 attempts to explain the increase in the radial distribution function and the reason for this trend. As detailed in section 2.5.5 of Chapter 2, the radial distribution function can be integrated to obtain a local number density or ρ_{local} . The local number density in this case is the number of C_a atoms in a given sphere around pyrene (or the C4s atoms). The sphere is defined by R_{cut} . The bulk density or ρ_{bulk} is obtained by the ratio of the total number of C_a atoms in the simulation to the volume of the simulation box. The Local Number Density Enhancement or LNDE is the ratio of the local density to the bulk density. As seen in Table 3-3, ρ_{local} of acetone decreases with CO₂ mole fraction. But the ratio of the local density with respect to the bulk density increases, and this is what causes the increase in the radial distribution function. This suggests that acetone does form significant structure around pyrene with added CO₂ pressure. However, addition of CO₂ dilutes the structure of acetone around pyrene. This dilution causes a local composition decrease.

To summarize, the radial distribution function is normalized with respect to the bulk density (of the species in question). The $g(r)$ gives some measure of the significance of a certain interaction, which creates a local structure. On the other hand, the local

composition is with respect to the solvation sphere defined by a critical radius or R_{cut} .

This is why the trends in $g(r)$ and local composition can be different.

Table 3-3. Local Number Density Enhancements (LNDE) for C4s-Ca interactions from pyrene-CO₂-acetone simulations.

Interaction	x (CO ₂)	$R_{\text{cut}}(\text{\AA})$	ρ_{local} (Molecules/ \AA^3)	ρ_{bulk} (Molecules/ \AA^3)	LNDE ($\rho_{\text{local}}/\rho_{\text{bulk}}$)
C4s-Ca	0.242	6.775	0.01615	0.00621	2.6
C4s-Ca	0.5	7.025	0.0133	0.00422	3.1
C4s-Ca	0.8	7.075	0.0069	0.00172	4.0
C4s-Ca	0.9	6.775	0.0031	0.0007	4.4

Conclusions

Pyrene is a widely used chromophore for probing the cybotactic region. In this work, molecular dynamics simulations of pyrene in CO₂-expanded methanol and CO₂-expanded acetone were performed at 313 K and pressures between 15-75 bars. Carbon dioxide shows structure around pyrene in CO₂-expanded methanol, and this structure does not change with added CO₂. Methanol molecules show much less structure around pyrene than carbon dioxide molecules in CO₂-expanded methanol, and this structure does not change with CO₂ addition. Acetone molecules in CO₂-expanded acetone, however, showed significant structure around pyrene and the radial distribution function increased with added CO₂.

By combining the pyrene-carbon dioxide and pyrene-methanol $g(r)$ and $g(r,\theta)$ results from CO₂-expanded methanol, a proposed structure of half of the cybotactic region about pyrene is drawn. Furthermore, local compositions of methanol around pyrene in CO₂-expanded methanol and acetone around pyrene in CO₂-expanded acetone decrease with CO₂ mole fraction. This suggests that the cybotactic region looks more and more like CO₂ as CO₂ is added, consistent with UV-vis absorption results.

The author expected to see much more actual structure of methanol around pyrene in CO₂-expanded methanol, shown by more than one prominent peak in the radial distribution function. Also, the local compositions of methanol around pyrene in CO₂-expanded methanol were less than the bulk mole fractions of methanol, also an unexpected result. As recommended in Section 5.2 of Chapter 5, a polarizability component should be added to pyrene's force field in order to better represent the bulky

cloud of pi electrons. In other words, with additive site-site point-charges and Lennard-Jones terms, the forces are not strong enough to attract methanol molecules to pyrene. Methanol molecules in the simulated system would rather cluster amongst themselves.

3.7 References

- (1) Wyatt, V., Bush, D., Lu, J; Hallett, J., Liotta, C., Eckert, C. *J. Supercrit Fluid* **2005**, *36*, 16.
- (2) Kelley, S., Lemert, R. *AIChE J.* **1996**, *42*, 2047.
- (3) Niemeyer, E., Bright, F. *Appl. Spect.* **1997**, *51*, 1547.
- (4) Baker, S., Baker, G., Kane, M., Bright, F. *J. Phys. Chem. B.* **2001**, *105*, 9663.
- (5) Prado, E., Yamaki, S., Atvars, T., Zimmerman, O., Weiss, R. *J. Phys. Chem. B.*, *104*, 5905.
- (6) Honda, C., Katsumata, Y., Yasutome, R., Yamazaki, S., Ishii, S., Matsuoka, K., Endo, K. **2006**, *182*, 151.
- (7) Offen, H., Turley, W. *J. Phys. Chem.* **1982**, *86*, 3501.
- (8) Niemeyer, E., Bright, F. *Energy & Fuels* **1998**, *12*, 823.
- (9) Rice, J., Niemeyer, E., Dunbar, R., Bright, F. *J. Am. Chem. Soc.* **1995**, *117*, 5832.
- (10) Brennecke, J., Eckert, C.A. "Proc. Int. Symp. on Supercritical Fluids", 1988, Nice, France.
- (11) Chen, S., McGuffin, V. *Appl. Spect.* **1994**, *48*, 596.
- (12) Tanaka, Y., Ueda, K., Ebisuzaki, S., Akanuma, T., Kato, T., Nishino, N. *Peptide Science (2001)* **2000**, 355.
- (13) Liou, Y., Fuchs, F. *Biophys. J.* **1992**, *61*, 892.
- (14) Knutson, B., Tomasko, D., Eckert, C., Debenedetti, P., Chialvo, A. *ACS Symp. Ser.* **1992**, *488*, 60.
- (15) Chialvo, A., Debenedetti, P. *Ind. Eng. Chem. Res.* **1992**, *31*, 1391.
- (16) Potoff, J., Siepmann, I. *AIChE J.* **2001**, *47*, 167.
- (17) Jorgensen, W. *J. Phys. Chem.* **1986**, *90*, 1276.
- (18) Jorgensen, W., Briggs, J., Contreras, M. *J. Phys. Chem.* **1990**, *94*, 1683.
- (19) Sun, H. *J. Phys. Chem. B.* **1998**, *102*, 7338.

- (20) Hoff, B., Strandberg, E., Ulrich, A., Tieleman, D., Posten, C. *Biophys. J.* **2005**, 88, 1818.
- (21) Duffy, E., Kowalczyk, P., Jorgensen, W. *J. Am. Chem. Soc.* **1993**, 115, 9271.
- (22) Cinacchi, G., Colle, R., Tani, A. *J. Phys. Chem. B.* **2004**, 108, 7969.
- (23) Mac Spartan Pro. Wavefunction, Inc. Irvine, CA., 2000.
- (24) Kong, J., White, C., Krylov, A., Sherrill, C.D., Adamson, R.D., Furlani, T.R., Lee, M., Lee, A., Gwaltney, S., Adams, T., Daschel, H., Zhang, W., Korambath, P., Ochsenfeld, C., Gilbert, A., Kedziora, G., Maurice, D., Nair, N., Shao, Y., Besley, N., Maslen, P., Dombroski, J., Baker, J., Byrd, E., Van Voorhis, T., Oumi, H., Hirata, S., Hsu C., Ishikawa, N., Florian, J., Warshel, A., Johnson, B., Gill, P., Head-Gordon, M., Pople, J. *Journal of Computational Chemistry* **2000**, 21, 1532.
- (25) Smith, W., Forester, T.R., 1996.
- (26) Chiehming, C., Kou-Lung, C., Chang-Yih, D. *J. Supercrit Fluid* **1998**, 12, 223.
- (27) Span, R., Wagner, W. *J. Phys. Chem. Ref. Data* **1996**, 25, 1509.
- (28) Zagrobelny, J., Betts, T., Bright, F. *J. Am. Chem. Soc.* **1992**, 114, 5249.
- (29) Stubbs, J., Siepmann, I. *J. Chem. Phys.* **2004**, 121, 1525.
- (30) Tucker, S., Maddox, M. *J. Phys. Chem. B.* **1998**, 102, 2437.

CHAPTER 4

DIFFUSION COEFFICIENTS IN CO₂-EXPANDED METHANOL: SYNERGY OF SIMULATIONS AND EXPERIMENTS

4.1 Introduction

Investigation of diffusion coefficients is important for the design and optimization of gas-expanded liquids. The transport properties of a system govern, among other factors, the rate of a reaction. In a heterogeneous reaction system, knowledge of the transport in the media is critical for reducing mass-transfer limitations. The goal of this chapter is two-fold: 1) to assess whether the local structure in the cybotactic region of a solute affects its diffusivity. This chapter, in a sense, touches on the topic of structure/property relationships. In other words, properties in the microenvironment can be manipulated to control bulk attributes. 2) to establish the predictive capability of computer simulations for GXL systems.

In this work, molecular dynamics simulations are combined with experimental techniques to determine the diffusion coefficients of heterocyclic solutes in CO₂-expanded methanol. Figure 4-1 shows the molecular structures of the five solutes: benzene, pyridine, pyrimidine, pyrazine, and 1,3,5-triazine. These solutes were chosen for their potential to interact with GXL components as well as their range of dipole moments. Furthermore, the binary diffusion coefficient of benzene had been previously studied in CO₂-expanded methanol for the entire composition range², thus providing one data point for comparison.

The next section describes the Taylor-Aris dispersion experiment used to determine the diffusion coefficients.

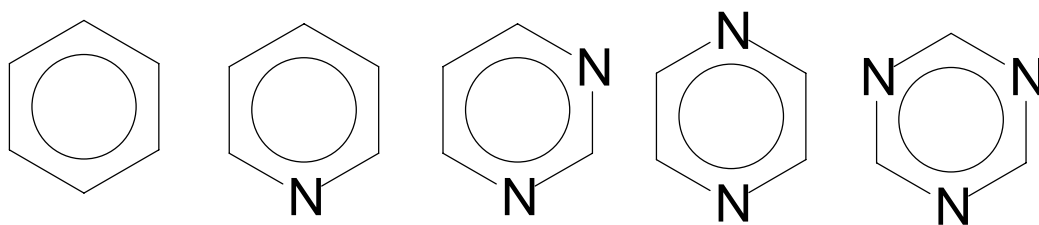


Figure 4-1. Solutes under investigation. From left to right: benzene, pyridine, pyrimidine, pyrazine, 1,3,5-triazine.

4.2 Description of the Taylor-Aris Dispersion Technique

The Taylor-Aris Dispersion³⁻⁵ technique is one method of measuring diffusion coefficients. Figure 4-2 is a schematic of the Taylor-Aris technique. A sharp pulse is injected into a long, thin tube filled with a mobile gas-expanded liquid. The gas-expanded liquid is in laminar flow. As the mobile phase is carried through the tube, the solute pulse disperses, forming a concentration profile. This resulting concentration profile is then used to determine the diffusion coefficient of the solute in the solvent. The initial solute pulse results in both axial and radial dispersion. If the diffusion is fast, then the velocity current of the mobile phase will carry the pulse axially, minimizing the radial dispersion to a minimum. Thus, fast diffusion produces less radial dispersion as shown in Figure 5-1, while slow diffusion produces a broader radial dispersion .

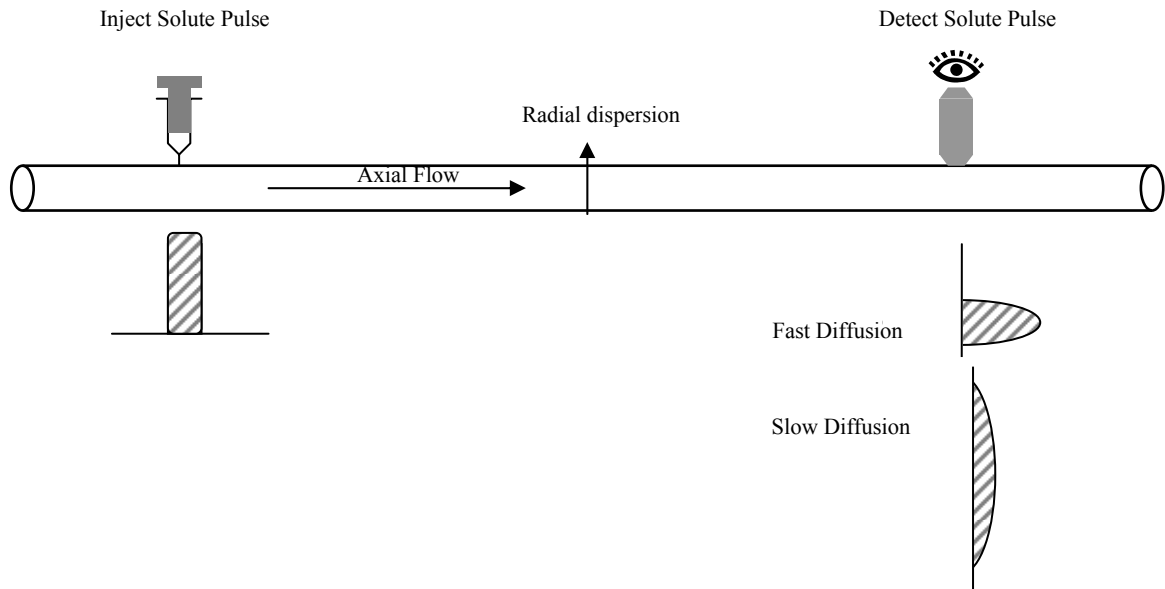


Figure 4-2. Schematic of the Taylor-Aris dispersion technique.

The diffusion coefficient D_{12} is then determined by the following equation⁶:

$$D_{12} = \left(\frac{\bar{u}_0}{4} \right) \left\{ H - \left[H^2 - \left(\frac{r_0}{3} \right)^2 \right]^{1/2} \right\} \quad \text{Equation 4-1}$$

where \bar{u}_0 is the average velocity of the mobile phase, r_0 is the inner radius of the tube, and H is given by the following:

$$H = \frac{1}{2.354^2 W_{1/2}^2 L} \quad \text{Equation 4-2}$$

where L is the length of the tube, and $W_{1/2}$ is the width of the peak at half the peak height. The software package connected to the detector does not exactly calculate a dispersion term, but rather the $W_{1/2}$. For this system, \bar{u}_0 was set to 0.2 mL/min. The tube is coiled, and its length is 100 feet. The next section details the simulation details used to model these solutes in CO₂-expanded methanol.

4.3 Simulation Details

In what follows, representative conditions from each of these regimes have been selected from experiments and used to conduct detailed and extensive MD simulations of the heterocyclic solutes in CO₂-expanded methanol. The mole fractions, densities, and temperature for the methanol-CO₂ GXL systems investigated here are reported in Table 4-1. The simulation system represents a single liquid phase with the compositions and pressure determined by these experiments and the density determined by the Peng-Robinson equation of state⁷.

Carbon dioxide and methanol have been modeled as rigid collections of atomic sites with specified fixed charges interacting through pairwise-additive, site-site Lennard Jones and Coulomb forces. Equation 4-3 presents the force field in the CO₂-methanol and CO₂-acetone systems. The first term represents the van der Waals potential, while the second term represents the electrostatic or Coulombic potential.

$$u_{ij} = \sum_i \sum_{j>i} \left[4\epsilon_{ij} \left\{ \left(\frac{\sigma_{ij}}{r_{ij}} \right)^{12} - \left(\frac{\sigma_{ij}}{r_{ij}} \right)^6 \right\} + \frac{q_i q_j}{r_{ij}} \right] \quad \text{Equation 4-3}$$

Carbon dioxide pair interactions have been modeled using the Transferrable Potential for Phase Equilibria or TrAPPE potential.⁸ The J2⁹ potential, a subset of the Optimized Potentials for Liquid Simulations (OPLS), has been used for methanol pair interactions. Section 2.2 of Chapter 2 presents detailed information about these two potentials. The potentials for pyridine, pyrimidine, pyrazine, and benzene are all-atom potentials and also OPLS-derived.^{10,11} To the best of the author's knowledge, there exists no force field for 1,3,5-triazine, so this molecule could not be simulated. Each of the pairwise potentials

specifies a representation for the fixed point charges and these are assumed to remain fixed in the heterogeneous pairwise Coulomb interactions.

Molecular dynamics (MD) simulations were carried out using the DL_POLY Software package¹². Regardless of the relative composition, each simulated system box is populated by a total of 1001 molecules: one solute molecule and 1000 solvent/cosolvent molecules. Cubic periodic boundary conditions (PBCs) are used throughout, but the length of the system box is scaled to preserve the specified density as per Table 4-1. Typical box lengths are on the order of 20-50 Å, and more specifically 40-50 Å for the GXL systems simulated. Because of the PBC, the potential interactions must necessarily be cut off to less than or equal to half the box length. Coulombic interactions are handled by the Ewald summation method with automatic parameter optimization (by DL_POLY). The equations of motion were integrated using the Velocity verlet algorithm as implemented by DL_POLY using a time step of 1.0 femtosecond. Structural information (at equilibrium) has been obtained using the NVT (constant moles, constant volume, constant temperature) ensemble with a Nose-Hoover thermostat in which the relaxation constant is set to 0.3. Initial configurations of the system box are generated using a random packing of the molecules in the periodic box followed by a 50 picoseconds MD simulation at NVT conditions.

When performing preliminary simulations, initial configurations in which CO₂ molecules were placed separately from methanol molecules are created, occupying different parts of the simulation box. This two-phase structure was stable during the simulation time and didn't show mixing. The initial conditions for subsequent simulations, however, placed all the molecules in random positions, assuming that the

CO₂ and methanol molecules were in a mixed, near-equilibrium state. Again, the bulk structure did not change substantially during the simulation. Thus, within the time and length scales of the simulations, the system remains at least in a metastable state.

Statistics are collected during a 300 picoseconds MD simulation at NVT conditions. The final equilibrium statistics are averaged over seven trajectories derived from seven different initial configuration files. The final configurations of each of the NVT runs are subsequently used as initial configurations for 1 nanosecond MD simulation runs under NVE conditions for collecting time-dependent statistics. These time-dependent statistics are used to calculate the diffusion coefficients of the solutes in CO₂-expanded methanol. The binary diffusion coefficients are calculated using the Einstein relation¹³:

$$D = \lim_{t \rightarrow \infty} \frac{1}{6t} \langle [\vec{r}(t) - \vec{r}(0)]^2 \rangle \quad \text{Equation 4-4}$$

In the experiments, a solute in CO₂-expanded methanol was infinitely dilute. Thus, only one solute was placed in a simulation box, amongst 1000 CO₂/methanol molecules.

Table 4-1. Solvent conditions used for simulations; T=313 K.

x (CO ₂)	P ¹⁴	ρ ^L (kg/m ³)
0	150	820
0.195	150	860
0.686	150	940

4.4 Results

4.4.1. Diffusion Coefficients

Figure 4-3 displays the diffusion coefficients at 313 K of all five heterocyclic solutes for 0%, 25%, 50%, 75%, and 100% CO₂ volume fraction. The diffusion coefficients of all solutes increase with added CO₂. This finding is consistent with both previous work on benzene diffusion in CO₂-methanol² as well as Figure 2-10 in Chapter 2. Figure 2-10 of this thesis shows an increase in the simulated self-diffusion coefficients of methanol in CO₂-expanded methanol with added CO₂ pressure. Furthermore, it appears that the value of the diffusion coefficient for each solute in Figure 4-3 is the same for a given volume fraction. For example, the diffusion coefficient at 50% volume fraction is 5×10^{-9} m²/s for benzene, pyrimidine, pyrazine, and 1,3,5-triazine. The diffusion coefficient of pyridine is 4×10^{-9} m²/s, a value very close to the other four solutes. This general trend (for all of the volume fractions) suggests that inhomogeneities in the cybotactic region due to the differences in polarity of the solutes do not influence the diffusivity. In other words, the local environment does not impact the bulk diffusivity of these solutes in CO₂-expanded methanol.

Tables 4-2 through 4-5 tabulate the experimental¹⁵ and simulated diffusion coefficients of pyridine, pyrimidine, pyrazine, and benzene, uniformly. The first column in each table is the CO₂ volume fraction, and the last column presents the error in the simulated diffusion coefficient.

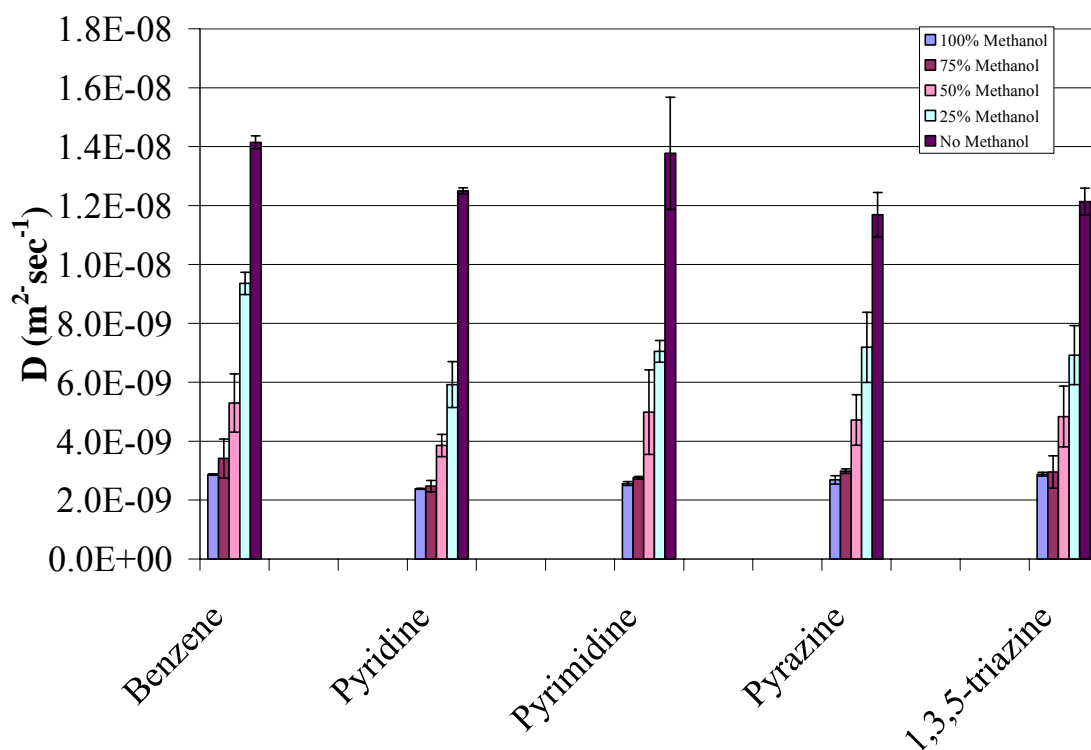


Figure 4-3. Experimental diffusion coefficients of benzene, pyridine, pyrimidine, pyrazine and 1,3,5-triazine in CO₂-expanded methanol as a function of volume fraction of methanol, 313 K, 150 bar. Data taken from Ref. 15.

Table 4-2. Experimental and simulated diffusion coefficients of pyridine in CO₂-expanded methanol; T=313 K.

Volume fraction CO ₂	D x 10 ⁹ m ² /s (experiment)	D x 10 ⁹ m ² /s (simulation)
0	2.2	0.913 ± 0.5
0.25	2.3	2.2 ± 1
0.75	6	6.2 ± 2

Table 4-3. Experimental and simulated diffusion coefficients of pyrimidine in CO₂-expanded methanol; T=313 K.

Volume fraction CO ₂	D x 10 ⁹ m ² /s (experiment)	D x 10 ⁹ m ² /s (simulation)
0	2.2	2.83 ± 1.5
0.25	2.7	2.9 ± 1.5
0.75	7	6 ± 2.4

Table 4-4. Experimental and simulated diffusion coefficients of pyrazine in CO₂-expanded methanol; T=313 K.

Volume fraction CO ₂	D x 10 ⁹ m ² /s (experiment)	D x 10 ⁹ m ² /s (simulation)
0	2.8	1.54 ± 1.5
0.25	3.1	2.5 ± 1.5
0.75	7.2	5.8 ± 2.4

Table 4-5. Experimental and simulated diffusion coefficients of benzene in CO₂-expanded methanol; T=313 K.

Volume fraction CO ₂	D x 10 ⁹ m ² /s (experiment)	D x 10 ⁹ m ² /s (simulation)
0	2.9	2.1 ± 0.5
0.25	3.4	3.2 ± 0.3
0.75	9.2	6 ± 1.7

The simulated diffusion coefficients of all four solutes increase with added CO₂ pressure, a finding consistent with the experimental results. The average simulated diffusion coefficients shown in these tables agree reasonably well with the experimental value. However, the error bars increase as CO₂ is added. The scatter in the simulation could be a result of several causes. Only one solute molecule is simulated in each GXL system. In section 2-6 of chapter 2, the root-mean squared deviation of each methanol molecule was averaged over at least 100 methanol molecules in the system. This, too, was averaged over 10 different initial trajectories. A sufficient amount of statistics was collected, and thus led to small error bars in Chapter 2. Thus, to obtain the level of accuracy as in Chapter 2, at least 100 trajectories need to be carried out for the solute molecule in CO₂-expanded methanol. This may not be very profitable in an industrial setting.

The simulation results cannot categorically conclude whether local heterogeneities in the cybotactic region of the solutes effect the diffusivity or not. However, the simulations are successful once again in reproducing the general trend that addition of CO₂ enhances the transport in the media. In the next section, structural results in the cybotactic region of the four solutes are presented.

4.4.2. Local Structure results

Molecular dynamics simulations can yield structural results not attainable by the Taylor-Aris technique. Figures 4-4 to 4-6 are plotted to ascertain the degree of hydrogen bonding between the nitrogen of each solute (N_s) and the protic hydrogen of methanol ¹. Figure 4-4 shows the N_s - H_m radial distribution function of pyridine in CO_2 -methanol. A sharp peak is immediately noticed at 2 Angstroms, the length of a hydrogen bond. Furthermore, with added CO_2 pressure, the $g(r)$ increases and obtains a maximum value of around 2.8 at 0.686 mole fraction CO_2 . This means that the probability of finding an H_m atom a distance 2 Angstroms from the N_s atom is 2.8 times greater than random. Figure 4-4 shows that methanol interactions with pyridine increase with added CO_2 pressure.

Figure 4-5 shows the N_s - H_m radial distribution function of pyrimidine in CO_2 -methanol. Again, a sharp peak is immediately noticed at 2 Angstroms, the length of a hydrogen bond. Furthermore, with added CO_2 pressure, the $g(r)$ increases and obtains a maximum value of around 2.9 at 0.686 mole fraction CO_2 . Figure 4-4 shows that methanol interactions with pyrimidine increase with added CO_2 pressure. The similar local structures around pyridine and pyrimidine can be explained by similar dipole moments. The dipole moments of pyridine and pyrimidine are 2.190 and 2.335, respectively. Although the dipole moment is not treated explicitly in these simulations, they are included in an averaged way in the Coulombic charges.

Figure 4-6 presents the radial distribution function of the N_s - H_m interactions of pyrazine in CO_2 -expanded methanol. At 2 Angstroms, the length of a hydrogen bond, a peak is observed with $g(r)$ around 0.4. This suggests that very minimal hydrogen bonding

occurs between pyrazine and methanol. A more prominent interaction between N_s and H_m occurs at around 5 Angstroms, with a $g(r)$ peaking at 1.2. However, with added CO_2 , this peak decreases. The CO_2 disrupts the structure at 5 Angstroms.

Finally, Figure 4-7 presents the radial distribution function between the carbon in benzene or C3s and the protic hydrogen of methanol or H_m . As expected, very little structure of H_m exists around C3s. A very broad peak at 6 Angstroms reaches a maximum $g(r)$ of around 1.2. This structure is probably due to the protic hydrogen interacting with the carbon atoms in benzene. The C3s atoms have a charge of -0.115, so there exists some electrostatic interaction between methanol and pyrene. However, addition of CO_2 breaks this structure also.

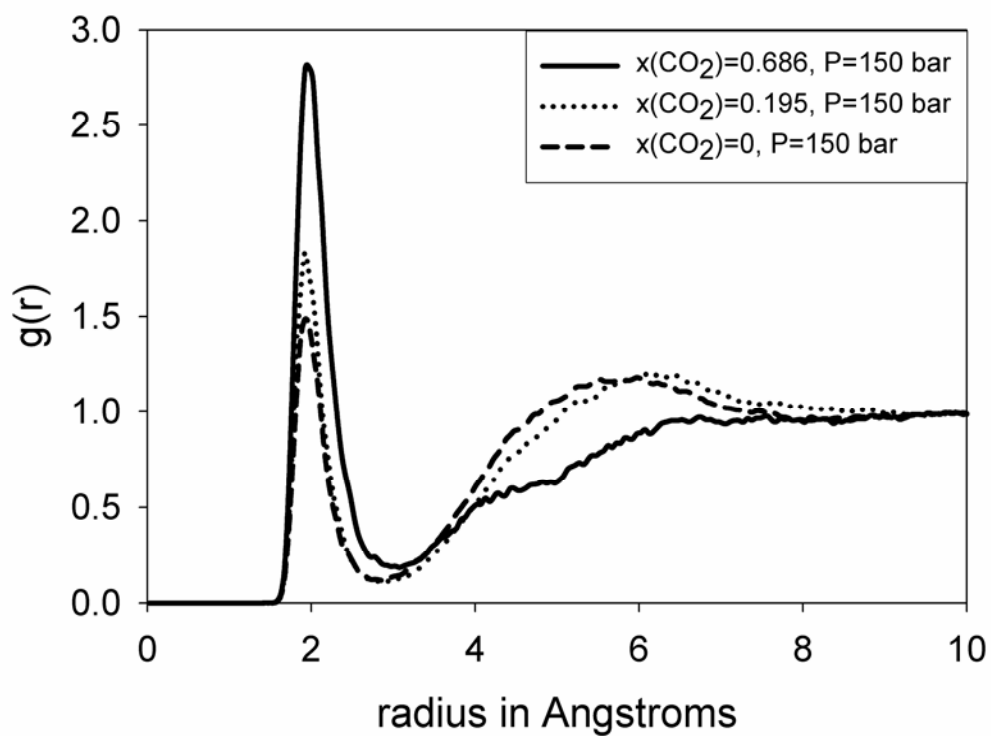


Figure 4-4. Radial distribution function between nitrogen of pyridine (N_s) and the protic hydrogen of methanol¹ versus radius in Angstroms at 0, 0.195, and 0.686 mole fraction CO_2 . $T=313\text{ K}$, $P=150\text{ bar}$.

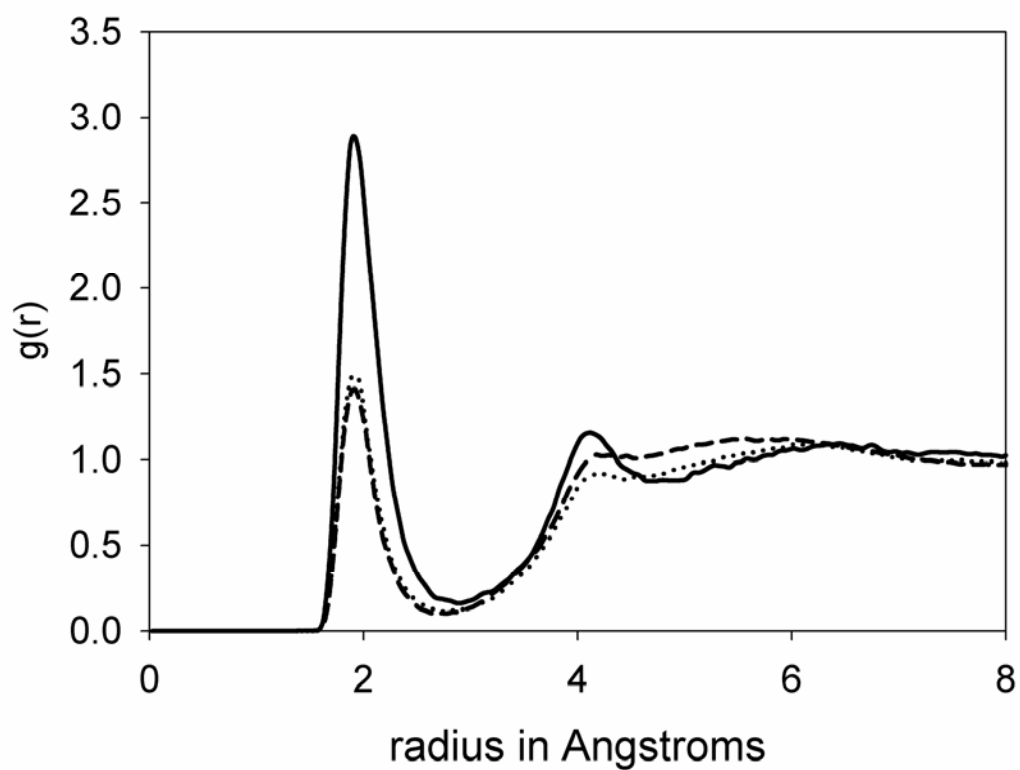


Figure 4-5. Radial distribution function between nitrogen of pyrimidine (N_3) and the protic hydrogen of methanol¹ versus radius in Angstroms at 0, 0.195, and 0.686 mole fraction CO_2 . $T=313$ K, $P=150$ bar.

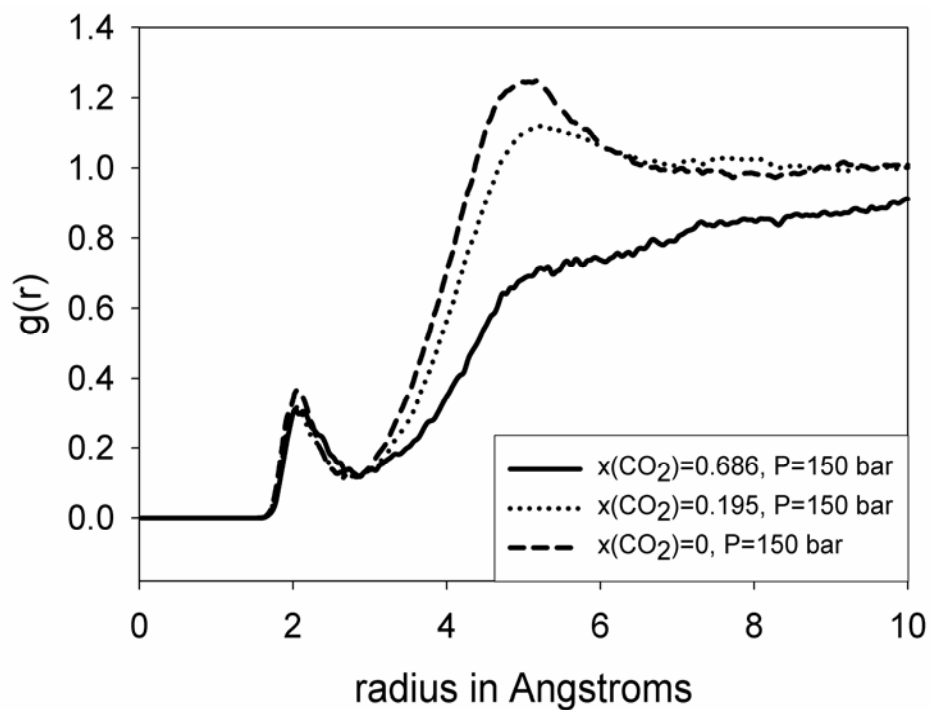


Figure 4-6. Radial distribution function between nitrogen of pyrazine (N_s) and the protic hydrogen of methanol¹ versus radius in Angstroms at 0, 0.195, and 0.686 mole fraction CO_2 . $T=313\text{ K}$, $P=150\text{ bar}$.

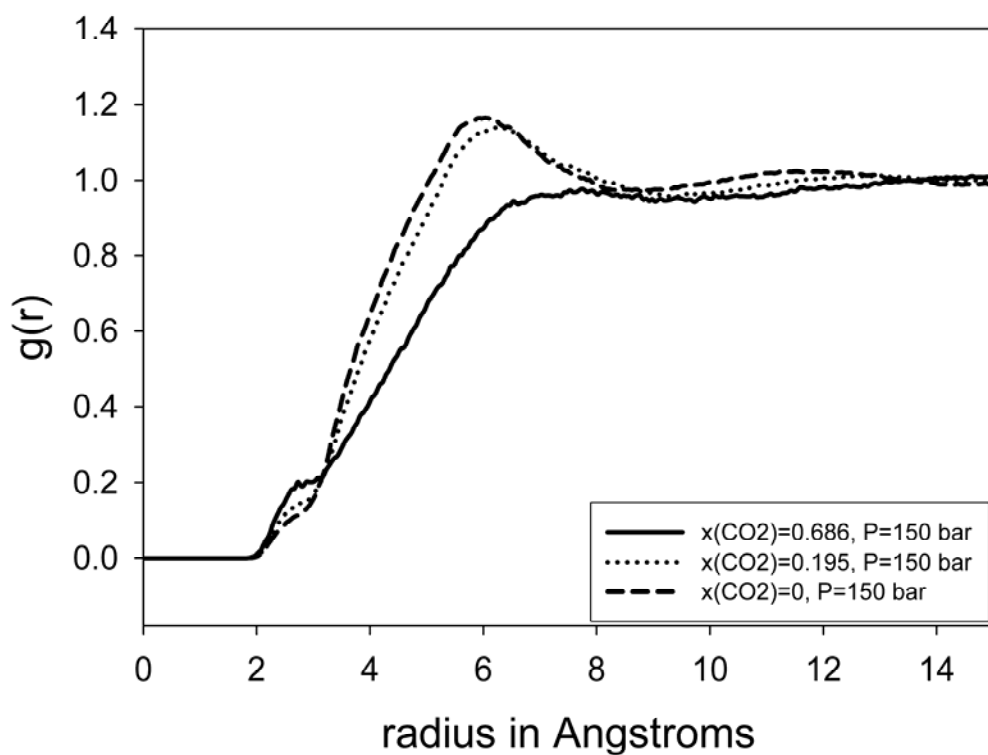


Figure 4-7. Radial distribution function between carbon in benzene (C_{3s}) and the protic hydrogen of methanol¹ versus radius in Angstroms at 0, 0.195, and 0.686 mole fraction CO_2 . $T=313\text{ K}$, $P=150\text{ bar}$.

Conclusions

Molecular dynamics simulations of benzene, pyridine, pyrimidine, and pyrazine in CO₂-expanded methanol were performed at 313 K and 150 bars. Binary diffusion coefficients of the solutes in CO₂-expanded methanol increased with added CO₂ pressure. This is consistent with experimental results obtained by the Taylor-Aris dispersion technique. While the experimental results suggest that the solute diffusivity is not dependent on the local polarity or local structure in the cybotactic region, the simulation results are inconclusive. The error in the diffusivity values are great enough to suggest either one of two things: 1) more trajectories are needed 2) local heterogeneities do affect the bulk transport. Hydrogen-bonding radial distribution functions show significant interaction between the nitrogen of the pyridine and pyrimidine and the protic hydrogen of methanol, and these interactions increase with added CO₂. Pyrazine and benzene, however, show very little interaction with the protic hydrogen of methanol, and any existing interaction decreases with added CO₂. The structural results conclude that the local environments about these probes are indeed different from each other.

4.5 References

- (1) Chiehming, C., Kou-Lung, C., Chang-Yih, D. *J. Supercrit Fluid* **1998**, 12, 223.
- (2) Sassiati, P., Mourier, P., Caude, M., Rossiet, R. *Anal. Chem.* **1987**, 59, 1164.
- (3) Taylor, G. *Proceedings of the Royal Society of London. Series A, Mathematical and Physical Sciences* **1953**, 219, 186.
- (4) Aris, R. *Proceedings of the Royal Society of London. Series A, Mathematical and Physical Sciences* **1954**, 235, 67.
- (5) Aris, R. *Proceedings of the Royal Society of London. Series A, Mathematical and Physical Sciences* **1956**, 235, 67.
- (6) Bueno, J., Saurez, J., Dizy, J., Medina, I. *J. Chem. Eng. Data* **1993**, 38, 344.
- (7) Peng, D., Robinson, D. *Industrial and Engineering Chemistry: Fundamentals* **1976**, 15, 59.
- (8) Potoff, J., Siepmann, I. *AIChE J.* **2001**, 47, 167.
- (9) Jorgensen, W. *J. Phys. Chem.* **1986**, 90, 1276.
- (10) Jorgensen, W., McDonald, N. *Journal of Molecular Structure (Theochem)* **1998**, 424, 145.
- (11) Duffy, E., Kowalczyk, P., Jorgensen, W. *J. Am. Chem. Soc.* **1993**, 115, 9271.
- (12) Smith, W., Forester, T.R., 1996.
- (13) Frenkel, D., Smit, B. *Understanding Molecular Simulation: From Algorithms to Applications*; Academic Press: San Diego, California, 2002; Vol. 1.
- (14) Shishikura, A., Kanamori, K., Kinbara, H. T. *J. Agr. Food Chem.* **1994**, 42, 1993.

- (15) Janakat, M. Synergistic Approach to Exploration of the Microstructure of Novel, Tunable Solvents for Reactions, Separations and Catalyst Recycle, Georgia Institute of Technology, 2005.

CHAPTER 5

CONCLUSIONS AND RECOMMENDATIONS

5.1 Conclusions

Computer simulations are valuable in designing and optimizing more environmentally-benign and cost-effective solvent systems useful in reactions and separations. Knowledge of the local chemistry can be effective in manipulating bulk reaction rates. For example, local chemistry in the cybotactic region affects the solubility of reactants and catalysts, the angle of approach of reactant to the catalytic site, and the local transport, all of which influence a reaction rate. Computer simulations can provide local structural information not easily attainable by experiments. Furthermore computer simulations can offer explanations of experimental results and assist in experimental design.

In this work, molecular dynamics (MD) simulations are used as a novel probe to elucidate the local environment in gas-expanded liquids. Chapter 2 commences the investigation by simulating CO₂-organic (the liquid phase) without solute at 298 K and pressures between 10-70 bar. The significant results are that methanol molecules cluster in CO₂-expanded methanol with added CO₂ pressure while acetone molecules in CO₂-expanded acetone do not. Furthermore, carbon dioxide addition increases the self-diffusion coefficient of methanol in CO₂-expanded methanol, thereby improving transport ability.

Chapter 3 adds a well-known chromophore, pyrene, into the GXL simulations to elucidate the local environment in conjunction with experiments at 313 K and 10-80 bars. The significant results are that the local composition of methanol around pyrene in CO₂-expanded methanol decreases with CO₂ addition. Likewise, the local composition of acetone in CO₂-expanded acetone decreases with CO₂ addition. These results are consistent with UV-vis spectroscopy data, which indicate that the cybotactic region of pyrene looks more and more like CO₂ with CO₂ addition. However, the local compositions of methanol around pyrene versus the bulk composition of methanol in CO₂-expanded methanol are less than the bulk values. The local compositions of acetone, however, are greater than the bulk values in CO₂-expanded acetone. This illustrates the role of solute-solvent interactions in local composition enhancements. Furthermore, acetone in CO₂-expanded acetone exhibited more structure around pyrene than methanol in CO₂-expanded methanol as revealed by radial distribution functions. Based on information extracted from radial distribution functions and orientational distribution functions, the author has attempted to map the cybotactic region around pyrene in CO₂-expanded methanol, a cartoon not easily obtainable by NMR results.

Chapter 4 concludes the investigation by demonstrating the capability of MD simulations in predicting diffusion coefficients of azocompound-solutes at 313 K and 150 bars. Simulated solute diffusion coefficients increase with added CO₂ pressure, and the values correspond reasonably well with results obtained by Taylor-Aris dispersion techniques. Furthermore, the simulations elucidate the local structure around the solutes, a result not obtainable by the Taylor-Aris dispersion technique.

The author proposes the following tasks for future work: 1) simulating excited state pyrene 2) addition of a polarizability term to the force field 3) a synergy of computation and experiment for elucidating the cybotactic region around three more solvatochromic dyes in CO₂-expanded methanol and 4) a hybrid method for simulating the cis-trans isomerization of azobenzenes. These propositions will be discussed in detail next.

5.2 Force field for Excited State Pyrene

A force field for excited state pyrene is unavailable in the literature. In this work, the charge distribution of excited state pyrene was attempted by density functional theory calculations with B3LYP functional and 6.31 G* basis set. These calculations were performed by the SPARTAN software package¹. SPARTAN successfully produced the charge distribution for the ground state as shown in Table 3-2 of Chapter 3. However, SPARTAN does not provide the charge distributions of excited state calculations. Density functional theory with B3LYP functional and cc-pVDZ was again attempted by Q-Chem² software package. Q-Chem was able to produce both the ground state and excited state charge distribution of pyrene as shown in Figure A1 and A2 in Appendix A. However, both the ground state and excited state charges are close to zero for all atomic sites. This finding cannot be accurate, because pyrene contains a bulky cloud of pi electrons. Therefore, the excited state yielded by the Q-Chem calculation was not used.

The author proposes a semi-empirical quantum chemistry method for the quantum calculation of pyrene's electronic structure. These semi-empirical methods are derived from the basic Hartree-Fock framework, but make several approximations and acquire some parameters from empirical data. The first semi-empirical method was MNDO or Modified Neglect of Differential Overlap³, which was later replaced by PM3 or Parametrized Model number 3⁴ and AM1 or Austin Model 1⁵. Kumar and Maroncelli⁶ performed MNDO calculations to obtain the geometries and charges of excited state Coumarin 153, a molecule with four rings and pi electrons. The Lennard Jones parameters of the ground state were used in the excited state as well.

After obtaining the partial charges of the pyrene excited state through semi-empirical methods, molecular dynamics simulations of excited-state pyrene can be performed in CO₂-expanded methanol and CO₂-expanded acetone. It is proposed that the simulated local structure and local compositions be compared to results obtained by fluorescence experiments.

5.3 Adding Polarizability

Polarizability is the induced dipole moment in an atom or molecule caused by an electric field. This electric field can be externally applied, or it could be caused by the charged dipoles of the surrounding molecules. In this work, the polarizability is included within the point-charge parameterization in an averaged way. This assumption is reasonable for lower-polarizable molecules like methanol and carbon dioxide, whose polarizabilities are $3.29 \times 10^{-24} \text{cm}^3$ and $2.11 \times 10^{-24} \text{cm}^3$, respectively.⁷ However, with its bulky cloud of pi-electrons, pyrene's polarizability is $28.2 \times 10^{-24} \text{cm}^3$, about 8.5 times greater than that of methanol. Therefore, a polarizability term in the force field becomes essential for a more accurate simulation of pyrene in GXLs.

The author expected to see much more structure of methanol around pyrene in CO₂-expanded methanol indicated by more than one prominent peak in the radial distribution function. This suggests that a simple pairwise-additive point-charge plus Coulombic term may not be sufficient, because the low point charges in pyrene would not be enough to attract the methanol molecules. In the proposed system the total energy would be the following:

$$E_{TOT} = E_{pair} + E_{pol} \quad \text{Equation 5-1}$$

where E_{pair} is the pairwise-additive Coulombic plus Lennard-Jones terms used in this work:

$$E_{pair} = \sum_i^N \sum_j \sum 4\epsilon_{ij} \left\{ \left(\frac{\sigma_{ij}}{r_{ij}} \right)^{12} - \left(\frac{\sigma_{ij}}{r_{ij}} \right)^6 \right\} + \frac{q_i q_j}{r_{ij}} \quad \text{Equation 5-2}$$

where N is the total number of pair interactions. E_{pol} - the polarization energy - is given by the following⁸:

$$E_{pol} = -\frac{1}{2} \sum_i^N \mu_i \cdot E_i^o = -\frac{1}{2} \sum_i^N \left[\alpha_i \left(E_i^o - \sum_j T_{ij} \cdot \mu_j \right) \right] \cdot E_i^o \quad \text{Equation 5-3}$$

where μ_i is the induced dipole of atom i obtained through a matrix inversion method⁹; E_i^o is the electrostatic field at the position of atom i due to the permanent charges of all other atoms belonging to different molecules and is given by the following:

$$E_i^o = \sum_j \frac{q_j}{r_j^2} \hat{r} \quad \text{Equation 5-4}$$

α_i is the polarizability of atom i , and T_{ij} is the dipole tensor.⁸

Polarizability may be necessary to fully capture the solvent interactions with aromatic dyes. It is proposed to calculate the local composition and local structure of methanol around pyrene in CO₂-expanded methanol as well as acetone around pyrene in CO₂-expanded acetone.

5.4 MD of solvatochromic probes

Figure 5-1 displays the bulk mole fraction vs. local mole fraction of methanol around five solvatochromic dyes in CO₂-expanded methanol at 40°C. Figure 5-1 was determined from UV-vis spectroscopy data performed by Wyatt, et. al.¹⁰ and shows the dependence of solute-solvent interactions on local composition enhancements. For example, the local composition of methanol around 4-nitroaniline is greater than that around N-N dimethyl 4-nitroaniline and 4-nitroanisole for any given bulk composition. This is probably due to the stronger hydrogen bonding between methanol and the amine group of 4-nitroaniline.

Simulations of N-N dimethyl 4-nitroaniline^{11,12}, 4-nitroanisole¹³, and 4-nitroaniline^{14,15} in CO₂-expanded methanol are proposed to elucidate the local structure about these dyes. Figure 5-2 presents the molecular structure of the solvatochromic probes. These three probes are chosen because the force fields are available in the literature. Unlike pyrene, these probes contain functional groups, and it would be relevant to see the effect of solute functional group-solvent interactions on the local structure and local composition around pyrene. Because the hydrogen-bonding is strongest in nitroaniline, one would expect to see different local structures around the functional group in nitroaniline than in the other probes. Furthermore, local compositions can be simulated and compared to those in Figure 5-1.

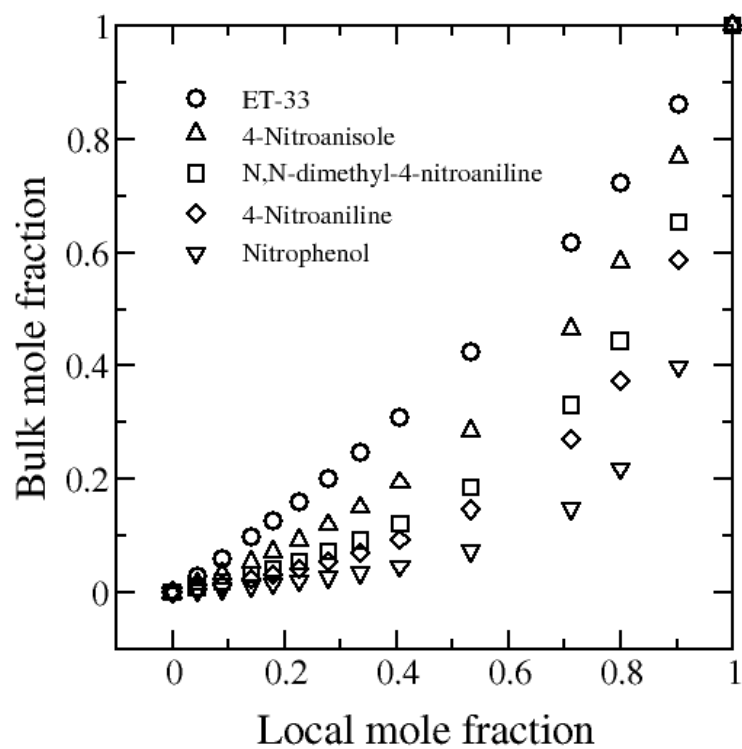


Figure 5-1. Bulk mole fraction vs. local mole fraction of methanol around five different solvatochromic dyes at 40°C: (○) ET-33 (△) 4-Nitroanisole (□) N,N-dimethyl-4-nitroaniline (◇) 4-Nitroaniline (▽) Nitrophenol. Data extracted from ref. 13.

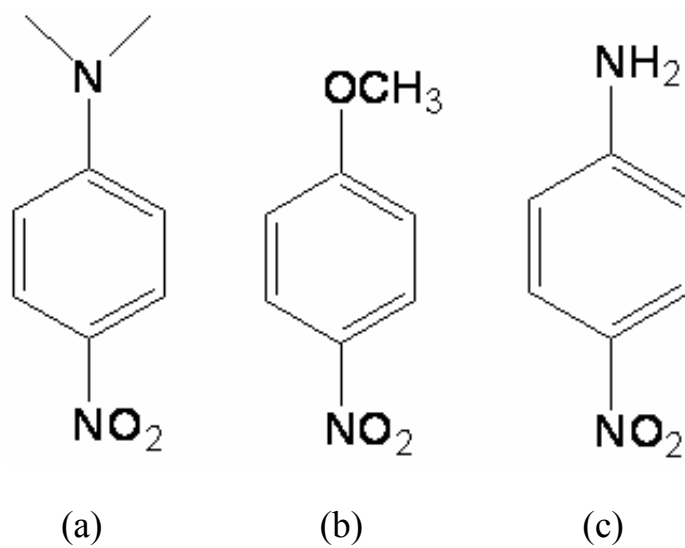


Figure 5-2. Solvatochromic indicators for Kamlet-Taft solvent parameters: (a) N,N -dimethyl p -nitroaniline (b) p -nitroanisole (c) p -nitroaniline

5.5 Hybrid QM/MM simulations of the Cis-trans Isomerization of Azobenzenes

The cis-trans isomerization of azobenzenes shown in Figure 5-3 is strongly dependent on the local environment around the transition state. Thus, the reaction can actually be used as a probe of local solvent polarity.¹⁶ However, molecular dynamics alone cannot treat the formation and breaking of bonds or electronic structure. Thus, a hybrid Quantum Mechanical/Molecular Mechanics (QM/MM) molecular orbital calculation is a proposed method of simulating the isomerization in gas-expanded liquids. This approach divides the system into two regions: Region I and Region II. Region I is the inner region and contains the reacting molecules which are represented quantum mechanically. Examples of quantum mechanical treatments include MNDO³, PM3⁴, AM1⁵, Hartree-Fock, and Density Functional Theory. Region II is the surrounding region and is represented by the molecular mechanics force fields such as Monte Carlo or MD.

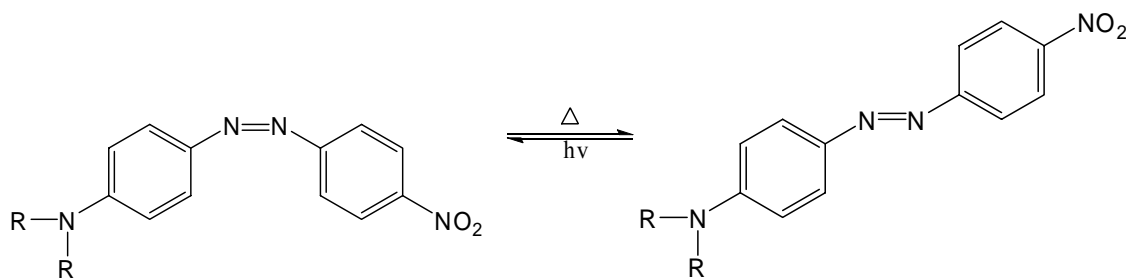


Figure 5-3. Cis-trans isomerization of azobenzenes.

Acevedo and Jorgensen¹⁷ simulated the Kemp decarboxylation reaction of benzisoxazole-3-carboxylic in water, acetonitrile, methanol, and THF using the hybrid

QM/MM approach. After computing the minimum-energy geometry, the simulation was run and a snapshot of the cybotactic region around the transition state was illustrated. Activation energies of the reaction were calculated and demonstrated excellent agreement with experimental values. Furthermore, local structure around the transition state was also shown through radial distribution functions.

The powerful hybrid QM/MM simulation approach can be used to elucidate the cybotactic region around the transition state of a reaction, such as the cis-trans isomerization of azobenzenes. The cybotactic region can then be altered computationally with CO₂ pressure to manipulate or predict different reaction pathways. Ab initio methods as detailed in Section 5.1 can be used to obtain a force field for the reactant and product.

5.6 References

- (1) Mac Spartan Pro. Wavefunction, Inc. Irvine, CA., 2000.
- (2) Kong, J., White, C., Krylov, A., Sherrill, C.D., Adamson, R.D., Furlani, T.R., Lee, M., Lee, A., Gwaltney, S., Adams, T., Daschel, H., Zhang, W., Korambath, P., Ochsenfeld, C., Gilbert, A., Kedziora, G., Maurice, D., Nair, N., Shao, Y., Besley, N., Maslen, P., Dombroski, J., Baker, J., Byrd, E., Van Voorhis, T., Oumi, H., Hirata, S., Hsu C., Ishikawa, N., Florian, J., Warshel, A., Johnson, B., Gill, P., Head-Gordon, M., Pople, J. *Journal of Computational Chemistry* **2000**, *21*, 1532.
- (3) Dewar, M., Thiel, W. *JACS* **1977**, *99*, 4899.
- (4) Stewart, J. *J. Comput. Chem.* **1989**, *10*, 209.
- (5) Dewar, M., Zoebisch, E., Healy, E., Stewart, J. *JACS* **1985**, *107*, 3902.
- (6) Kumar, P., Maroncelli, M. *J. Chem. Phys.* **1995**, *103*, 3038.
- (7) *CRC Handbook of Chemistry & Physics*; 76th ed.; Lide, D., Ed.; Chemical Rubber Publishing Co., 1995.
- (8) Gao, J., Habibollazadeh, D., Shao, L. *J. Phys. Chem.* **1995**, *99*, 16460.
- (9) Bernardo, D., Ding, Y. Krogh-Jespersen, K., Levy, R. *J. Phys. Chem.* **1994**, *98*, 4180.
- (10) Wyatt, V., Bush, D., Lu, J; Hallett, J., Liotta, C., Eckert, C. *J. Supercrit Fluid* **2005**, *36*, 16.
- (11) Makowska-Janusik, M., Reis, H., Papadopoulos, M., Economou, I., Zacharopoulos, N. *J. Phys. Chem. B.* **2004**, *108*, 588.
- (12) Michael, D., Benjamin, I. *J. Phys. Chem. B.* **1998**, *102*, 5145.
- (13) Klein, H., Fuess, H., Schrimpf, G. *J. Phys. Chem.* **1996**, *100*, 11101.
- (14) Reis, H., Papadopoulos, M., Grzybowski, A. *J. Phys. Chem. B.* **2006**, *110*, 18537.
- (15) Ghorai, P., Matyushov, D. *JACS* **2005**, *127*, 16390.

- (16) Dillow, A., Brown, J., Liotta, C., Eckert, C. *J. Phys. Chem. A.* **1998**, *102*, 7609.
- (17) Acevedo, O., Jorgensen, W. *JACS* **2005**, *127*, 8829.

APPENDIX A

Section I. EPM2 vs. TrAPPE Potential of CO₂

The TrAPPE potential¹ has been tested relative to both vapor-liquid coexistence curve and vapor pressure.

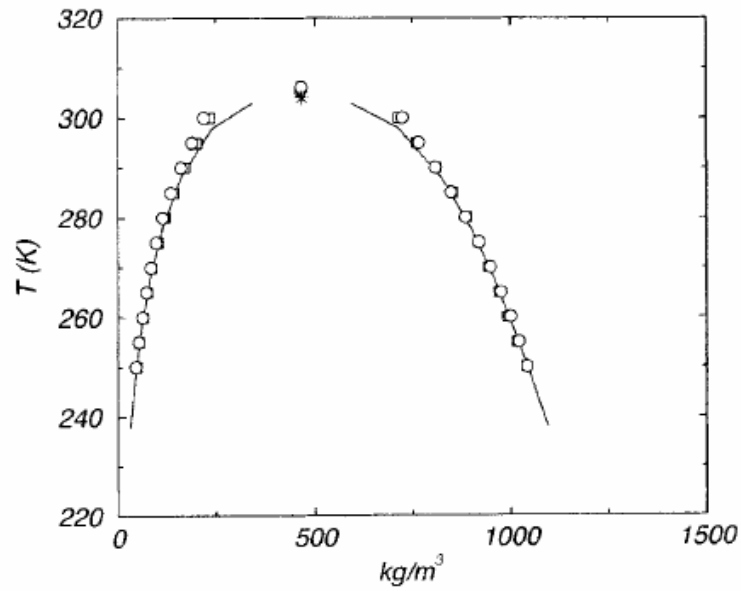


Figure A1. Vapor-liquid coexistence curve for carbon dioxide. Experimental data represented by solid line. Circles (○) are from TrAPPE potential, and squares (□) are from the EPM2 potential for CO₂. The Asterisk is the critical point. From Ref. 11 of Chapter 2.

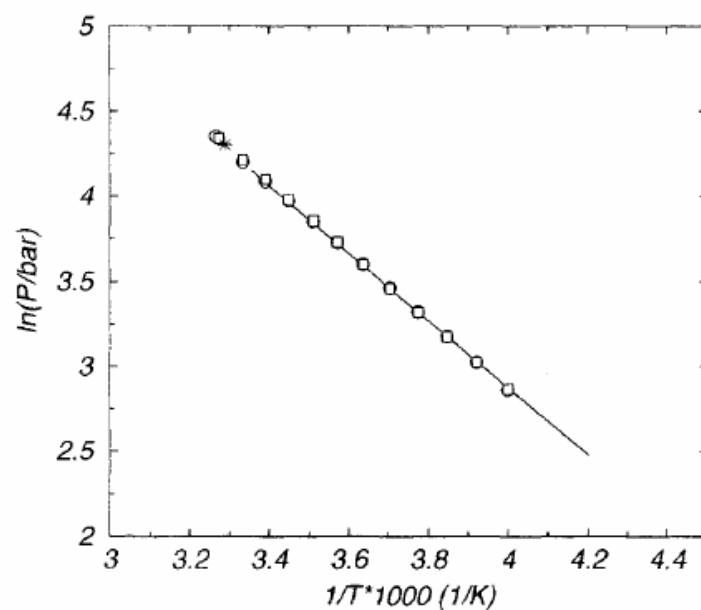


Figure A2. Vapor-liquid coexistence curve for carbon dioxide. Experimental data represented by solid line. Circles (○) are from TrAPPE potential, and squares (□) are from the EPM2 potential for CO_2 . Asterick is the critical point. From Ref. 11 of Chapter 2.

Section II. Lennard-Jones parameters

Table A1. Lennard-Jones interaction parameters for CO₂-MeOH simulations. Both the geometric mean (Lorentz) and the arithmetic mean (Lorentz-Berthelot) for the cross-term distance parameter are shown. Values actually used in the simulations are shown in bold font.

	σ in Å (directly from references)	σ in Å (geometric mean)	σ in Å (arithmetic mean)	e_{12} kJ/mol
Cg-Cg	2.8000			0.2244
Og-Og	3.0500			0.6565
Cg-Og		2.9223	2.9250	0.3838
Om-Om	3.0710			0.7110
CH ₃ -CH ₃	3.7750			0.8660
Om-CH ₃		3.4049	3.423	0.7847
Cg-Om		2.9324	2.9355	0.3994
Cg-CH ₃		3.2511	3.2875	0.4408
Og-Om		3.0605	3.0605	0.6832
Og-CH ₃		3.3932	3.4125	0.7540

Table A2. Lennard-Jones interaction parameters for CO₂-acetone simulations. Both the geometric mean (Lorentz) and the arithmetic mean (Lorentz-Bethelot) for the cross-term distance parameter are shown. Values actually used in the simulations are shown in bold font.

	σ in Å (directly from references)	σ in Å (geometric mean)	σ in Å (arithmetic mean)	e_{12} kJ/mol
Cg-Cg	2.8000			0.2244
Og-Og	3.0500			0.6565
Cg-Og		2.9223	2.9250	0.3838
Ca-Ca	3.7500			0.4393
Oa-Oa	2.9600			0.8786
CH3-CH3	3.9100			0.6694
Ca-Oa		3.3316	3.3550	0.6213
Ca-CH3		3.8292	3.8300	0.5423
Oa-CH3		3.4020	3.4350	0.7669
Cg-Oa		2.8789	2.8800	0.4441
Cg-Ca		3.2404	3.2750	0.3139
Cg-CH3		3.3088	3.3550	0.3876
Og-Oa		3.0047	3.0050	0.7595
Og-CH3		3.4533	3.4800	0.6629
Ca-Og		3.3819	3.4000	0.5370

Section III. Convergence of volume from NPT studies

Table A3. Outputted lengths of simulation box from NPT simulations for both CO₂-expanded methanol and pure methanol ; T=298 K ; Total # of molecules = 1000; Total simulation time = 400 ps

System	Ensemble	Mole fraction CO ₂	Inputted length of box (Å)	Inputted pressure from NVT studies in atm	Outputted length of box in Å from NPT studies
CO ₂ -methanol	NPT	0.13	41.00	174	41.024
				170	41.005
				174	41.002
Pure methanol	NPT	N/A	41	122	41.025
				136	40.99
				149	40.975

Section IV. Wilke-Chang ratio

This section explains how the Wilke-Chang ratio was used to approximate diffusion coefficients of methanol in CO₂-expanded methanol from available experimental data. The diffusion coefficient of benzene in CO₂-expanded methanol was measured at 313 K by a chromatographic broadening technique. These benzene diffusion coefficients were then used to obtain approximate diffusion coefficients of methanol in CO₂-expanded methanol at 313 K through the Wilke-Chang ratio.

The Wilke-Chang equation calculates the solute diffusion coefficient in a given solvent:

$$D = \frac{(7.4 \times 10^{-15}) T M_s^{1/2}}{\eta V^{0.6}}$$

T = temperature in K

M_s = molecular weight of the solvent in g

η = solvent viscosity in (Pa · s)

V = molar volume of solute at ambient temperature in cc/mol

The following ratio can be derived from the Wilke-Chang equation, and the authors call this ratio the Wilke-Chang ratio:

$$\frac{D_{meth}}{D_{benz}} = \frac{V_{benz}^{0.6}}{V_{meth}^{0.6}}$$

where a methanol molecule is treated as a solute molecule. By using the measured diffusion coefficient of benzene in CO₂-expanded methanol, one can obtain a reasonable estimate of the diffusion coefficient of methanol in CO₂-expanded methanol through this ratio. These values are plotted in Figure 2-9a of the main paper. The molar volume of methanol and benzene are 40 cc/mol and 88.6 cc/mol, respectively.

Section V. Calculation of diffusion coefficients in CO₂-expanded methanol

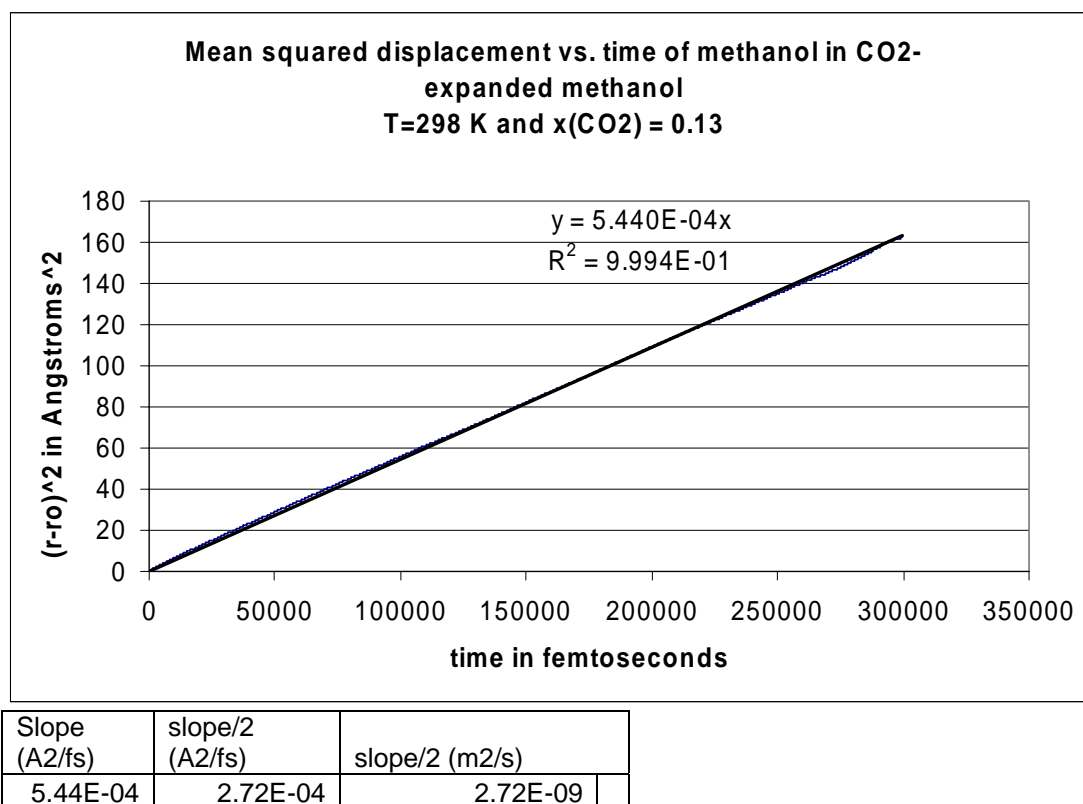
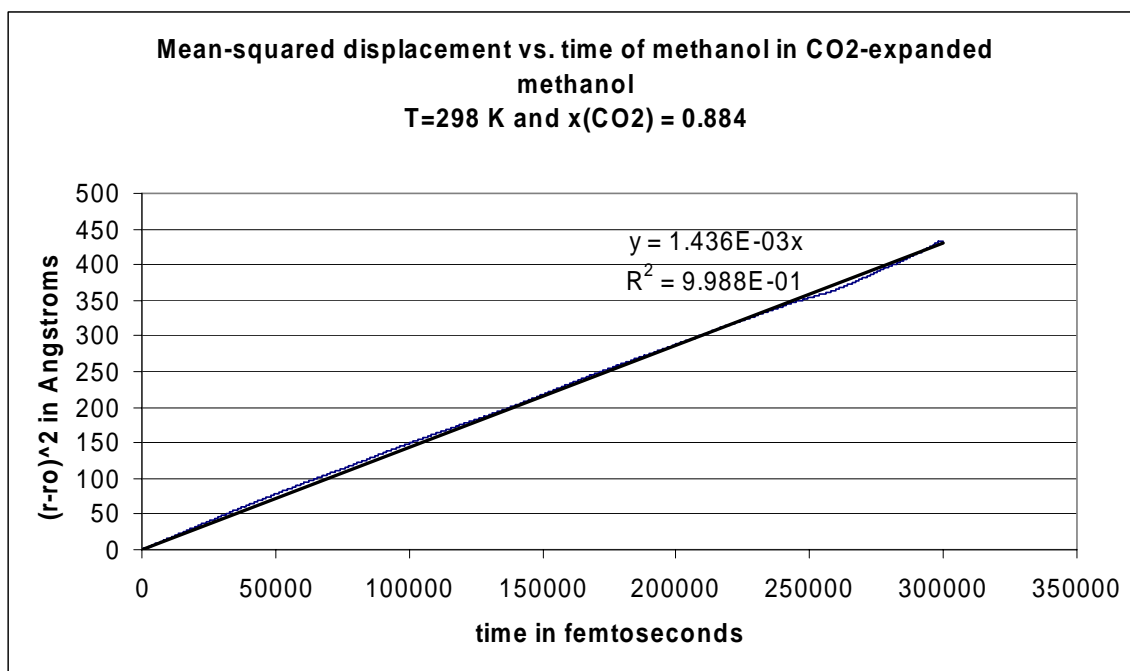


Figure A3. Sample mean squared displacements vs. time of methanol in CO₂-expanded methanol; T=298 K, x(CO₂)=0.13



Slope (Å ² /fs)	Slope/2 (Å ² /fs)	Slope/2 (m ² /s)
1.44E-03	7.18E-04	7.18E-09

Figure A4. Sample mean squared displacements vs. time of methanol in CO₂-expanded methanol; T=298 K, x(CO₂)=0.884

Section 5. Semilog plots of local density autocorrelation functions (LDAC)

This section presents the semilog plots vs. time of the local density autocorrelation (LDAC) function shown in Figure 2-10 of Chapter 2. Assuming that the correlation functions decay exponentially:

$$y = e^{-\frac{t}{\tau}}$$

where y is the LDAC, t is time in picoseconds, and τ is the decay constant or time constant in picoseconds. Time constants give information on the persistence of correlations over time in the simulations.

We have reported two time constants in our paper: the instantaneous time (τ_i) and the steady state time (τ_s). The instantaneous time is within the ballistic regime and is nonlinear. The steady state time is the time constant of the intermediate regime and displays linear behavior.

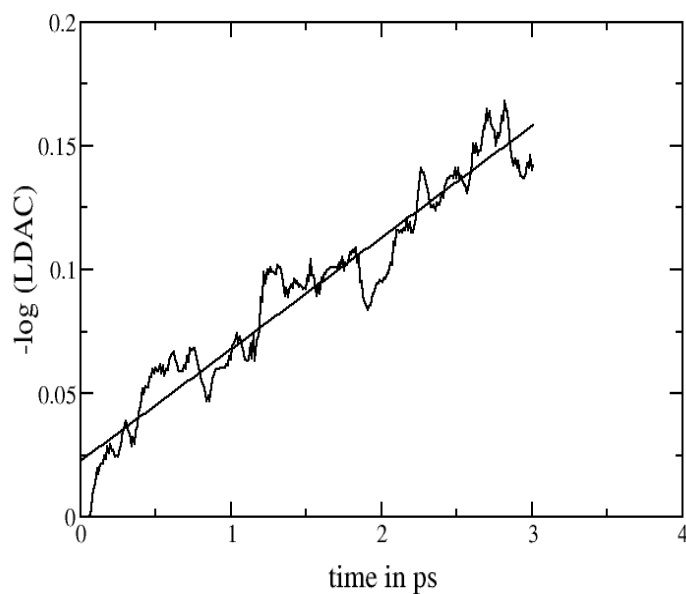


Figure A5. Semilog plot of the instantaneous regime of O_m-H_m local density autocorrelation function (LDAC) from CO_2 -expanded methanol simulations: $x(CO_2) = 0.884$, $\rho=861.8 \text{ kg/m}^3$ (dilated liquid region). Equation of fitted line: $v=0.04511x+0.02247$

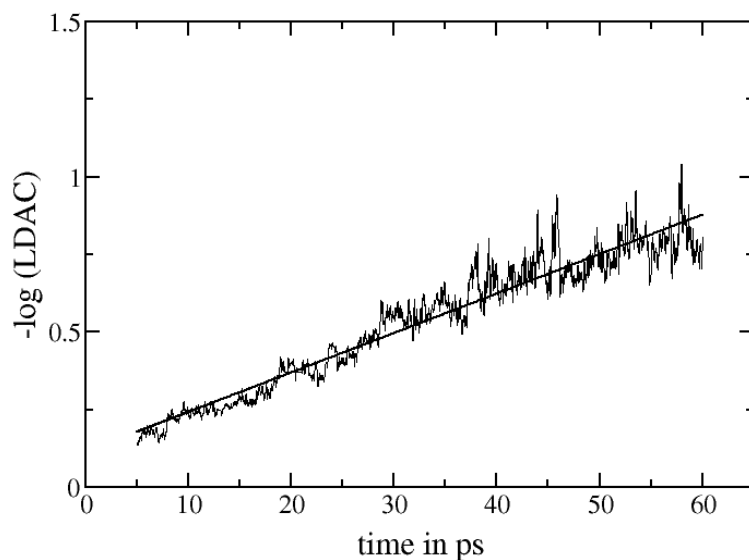


Figure A6. Semilog plot of the steady state regime of O_m-H_m local density autocorrelation function from CO_2 -expanded methanol simulations.

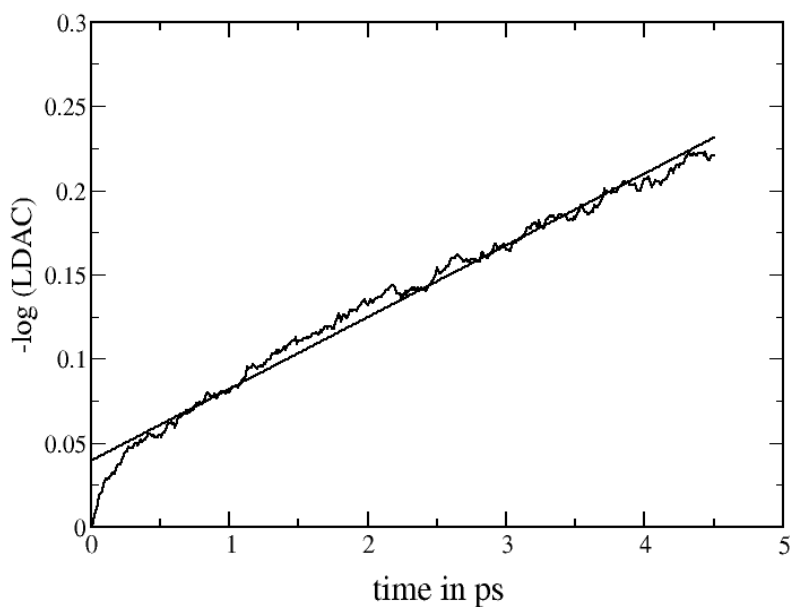


Figure A7. Semilog plot of the instantaneous regime of O_m-H_m local density autocorrelation function (LDAC) from CO_2 -expanded methanol simulations: $x(CO_2) = 0.130$, $\rho=810.3 \text{ kg/m}^3$ (normal liquid region). Equation of fitted line:

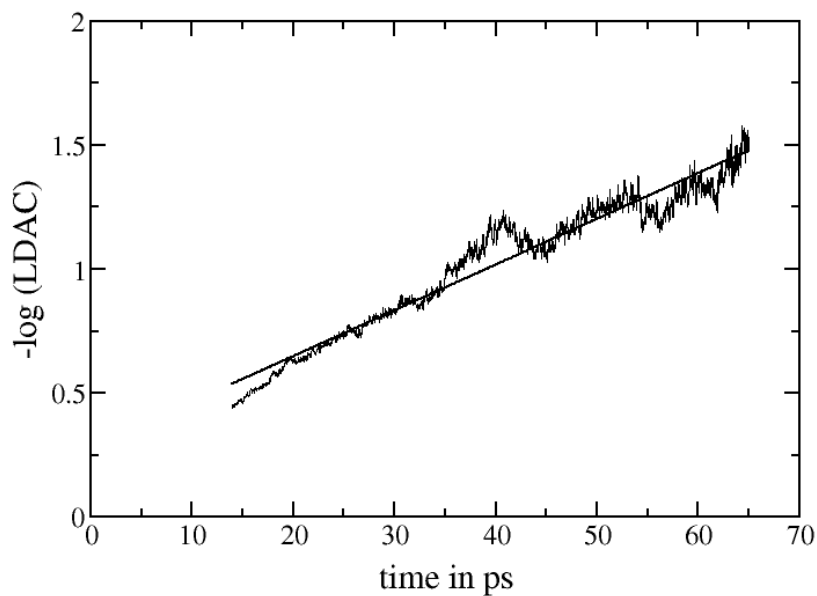


Figure A8. Semilog plot of the steady state regime of O_m-H_m LDAC from CO_2 -expanded methanol simulations: $x(CO_2) = 0.130$, $\rho=810.3 \text{ kg/m}^3$ (normal liquid region). Equation of fitted line:

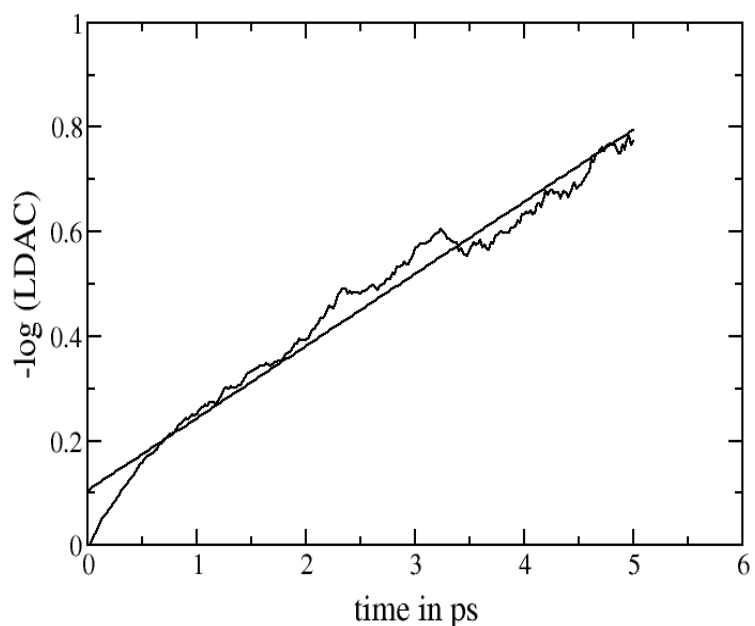


Figure A9. Semilog plot of the instantaneous regime of C_g - C_g local density autocorrelation function (LDAC) from CO_2 -expanded methanol simulations: $x(\text{CO}_2) = 0.884$, $\rho = 861.8 \text{ kg/m}^3$ (dilated liquid region). Equation of fitted line $y = 0.1381x + 0.1037$

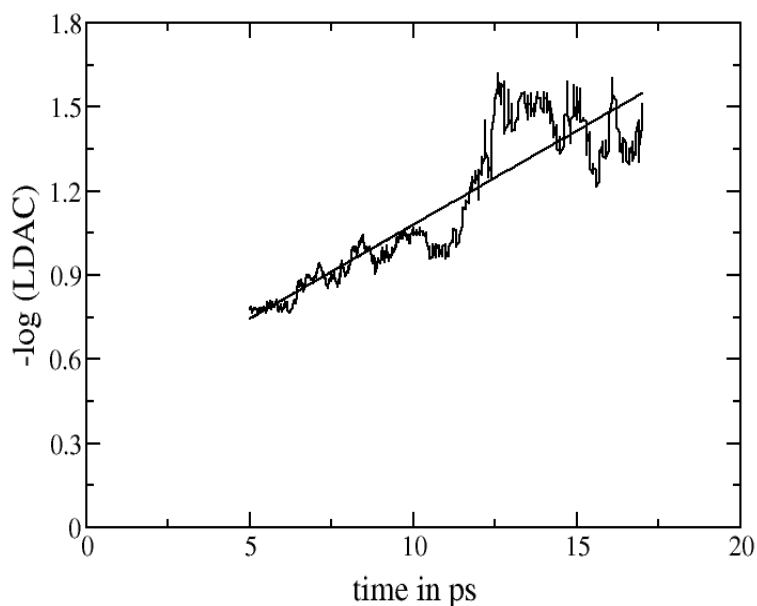


Figure A10. Semilog plot of the steady state regime of C_g - C_g local density autocorrelation function (LDAC) from CO_2 -expanded methanol simulations: $x(\text{CO}_2) = 0.884$, $\rho = 861.8 \text{ kg/m}^3$ (dilated liquid region). Equation of fitted line $y = 0.1381x + 0.1037$

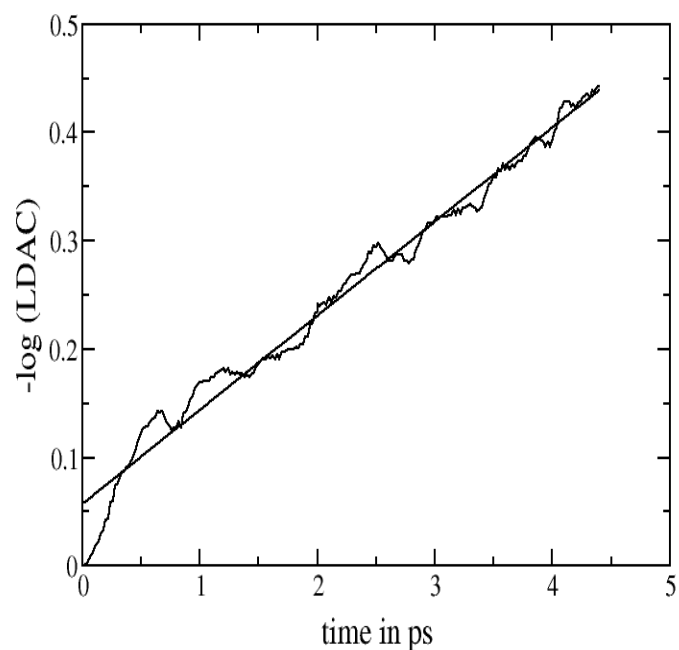


Figure A11. Semilog plot of the instantaneous regime of C_g - C_g local density autocorrelation function (LDAC) from CO_2 -expanded methanol simulations: $x(CO_2) = 0.130$, $\rho=810.3 \text{ kg/m}^3$ (normal liquid region).

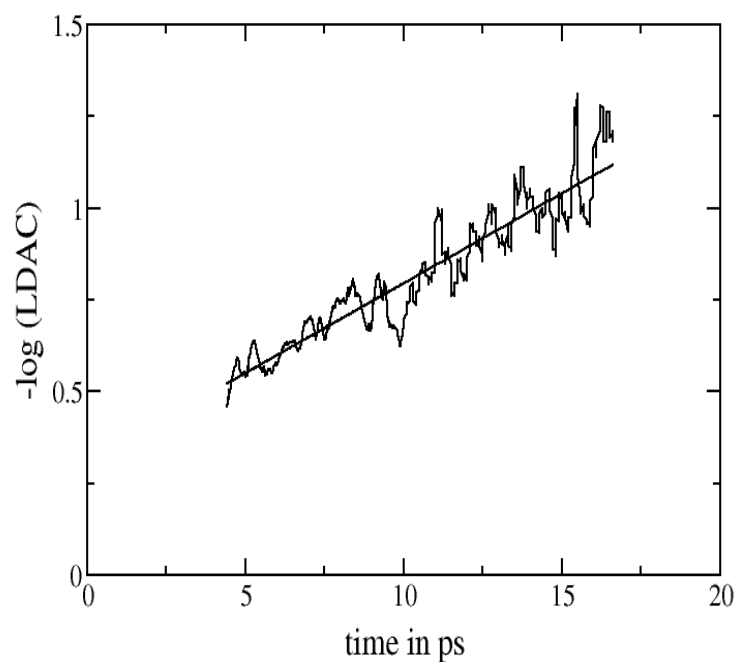


Figure A12. Semilog plot of the steady state regime of C_g - C_g local density autocorrelation function (LDAC) from CO_2 -expanded methanol simulations: $x(CO_2) = 0.130$, $\rho=810.3 \text{ kg/m}^3$ (normal liquid region). Equation of fitted line $y=0.04890x+0.3053$

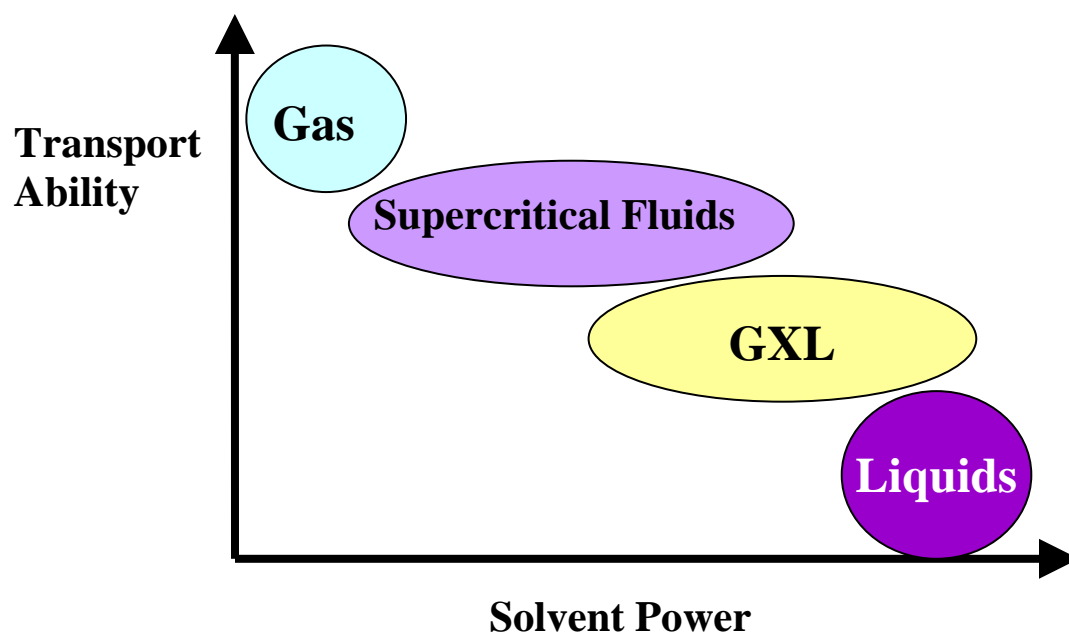


Figure A13. Gas-expanded liquids have intermediate properties between supercritical fluids and liquids.

APPENDIX B

Section I. This section presents a table of the CO₂-methanol-pyrene interactions with a subsequent explanation of the mixing rules.

Table B1. Lennard-Jones parameters of pyrene in CO₂-expanded methanol.

	σ in Å (directly from references)	σ in Å (geometric mean)	σ in Å (arithmetic mean)	ϵ_{12} kJ/mol
Cg-Cg	2.8000			0.2244
Og-Og	3.0500			0.6565
Cg-Og		2.9223	2.9250	0.3838
Om-Om	3.0710			0.7110
CH ₃ -CH ₃	3.7750			0.8660
Om-CH ₃		3.4049	3.423	0.7847
Cg-Om		2.9324	2.9355	0.3994
Cg-CH ₃		3.2511	3.2875	0.4408
Og-Om		3.0605	3.0605	0.6832
Og-CH ₃		3.3932	3.4125	0.7540
C2s-Cg		3.1528	3.175	0.2565
C2s-Og		3.2905	3.3000	0.4386
C2s-Om		3.3018	3.3105	0.4564
C2s-CH ₃		3.6607	3.6625	0.5037
C3s-Cg		3.1528	3.1750	0.2565
C3s-Og		3.2905	3.3000	0.4386
C3s-Om		3.3018	3.3105	0.4564
C3s-CH ₃		3.6607	3.6625	0.5037
C1s-Cg		3.1528	3.1750	0.2565
C1s-Og		3.2905	3.3000	0.4386
C1s-Om		3.3018	3.3105	0.4564
C1s-CH ₃		3.6607	3.6625	0.5037
C4s-Cg		3.1528	3.1750	0.2565
C4s-Og		3.2905	3.3000	0.4386
C4s-Om		3.3018	3.3105	0.4564
C4s-CH ₃		3.6607	3.6625	0.5037
H2s-Cg		2.6031	2.6100	0.1675
H2s-Og		2.7168	2.7350	0.2864
H2s-Om		2.7261	2.7455	0.2981

H3s-Cg		2.6031	2.6100	0.1675
H3s-Og		2.7168	2.7350	0.2864
H3s-Om		2.7261	2.7455	0.2981
H3s-CH ₃		3.0225	3.0975	0.3290
H1s-Cg		2.6031	2.6100	0.1675
H1s-Og		2.7168	2.7350	0.2864
H1s-Om		2.7261	2.7455	0.2981
H1s-CH ₃		3.02249	3.0975	0.3290

- The Lorentz-Berthelot mixing rule: the cross-term energy parameter is calculated by a geometric mean, and the cross-term distance parameter is calculated by an arithmetic mean,

$$\varepsilon_{12} = \sqrt{\varepsilon_1 \varepsilon_2}$$

$$\sigma_{12} = \frac{\sigma_1 + \sigma_2}{2}$$

- The Lorentz mixing rule: both the cross-term energy and distance parameters are calculated by a geometric mean,

$$\varepsilon_{12} = \sqrt{\varepsilon_1 \varepsilon_2}$$

$$\sigma_{12} = \sqrt{\sigma_1 \sigma_2}$$

- The TrAPPE potential for CO₂ stipulates that the CO₂-CO₂ cross terms (i.e. Cg-Og) should be calculated using the Lorentz-Berthelot mixing rules.
- The J2 potential for methanol states that the methanol-methanol cross terms (i.e. Om-CH₃) be calculated using the Lorentz rule.
- The OPLS potential for aromatics states that cross-term interactions be calculated using the Lorentz rule. Because only one solute exists, however, no pyrene-pyrene cross terms were inputted. Both pyrene-CO₂ and pyrene-methanol cross terms were calculated using the Lorentz mixing rule.

Table B2. Lennard-Jones parameters of aromatics from OPLS potential.

	σ (Angstroms)	ϵ (kJ/mol)
Cs-Cs	3.55	0.293
Hs-Hs	2.42	0.125

Table B3. Charges from OPLS potential.

	q(in e)
Cs	-0.115
Hs	0.115

Table B4. Lennard-Jones parameters of pyrene in CO₂-expanded acetone.

	σ in Å (directly from references)	σ in Å (geometric mean)	σ in Å (arithmetic mean)	e_{12} kJ/mol
Cg-Cg	2.8000^a			0.2244
Og-Og	3.0500^a			0.6565
Cg-Og		2.9223	2.9250	0.3838
Ca-Ca	3.7500^b			0.4393
Oa-Oa	2.9600^b			0.8786
CH3-CH3	3.9100^b			0.6694
Ca-Oa		3.3316	3.3550	0.6213
Ca-CH3		3.8292	3.8300	0.5423
Oa-CH3		3.4020	3.4350	0.7669
Cg-Oa		2.8789	2.8800	0.4441
Cg-Ca		3.2404	3.2750	0.3139
Cg-CH3		3.3088	3.3550	0.3876
Og-Ca		3.3819	3.4000	0.5370
Og-Oa		3.0047	3.0050	0.7595
Og-CH3		3.4533	3.4800	0.6629
C3s-Cg		3.1527	3.1750	0.2564
C3s-Og		3.2905	3.3000	0.4386
C3s-Ca		3.6486	3.6500	0.3588
C3s-Oa		3.2416	3.2550	0.5074
C3s-CH3		3.7256	3.7300	0.4429
C4s-Cg		3.1527	3.1750	0.2564
C4s-Og		3.2905	3.3000	0.4386
C4s-Ca		3.6486	3.6500	0.3588
C4s-Oa		3.2416	3.2550	0.5074
C4s-CH3		3.7256	3.7300	0.4429
C2s-Cg		3.1527	3.1750	0.2564
C2s-Og		3.2905	3.3000	0.4386
C2s-Ca		3.6486	3.6500	0.3588
C2s-Oa		3.2416	3.2550	0.5074
C2s-CH3		3.7256	3.7300	0.4429
C1s-Cg		3.1527	3.1750	0.2564
C1s-Og		3.2905	3.3000	0.4386

C1s-Ca		3.6486	3.6500	0.3588
C1s-Oa		3.2416	3.2550	0.5074
C1s-CH3		3.7256	3.7300	0.4429
H4s-Cg		2.6031	2.6100	0.1675
H4s-Og		2.7168	2.735	0.2865
H4s-Ca		3.0125	3.085	0.2343
H4s-Oa		2.6764	2.690	0.3314
H4s-CH3		3.0761	3.165	0.2829
H2s-Cg		2.6031	2.6100	0.1675
H2s-Og		2.7168	2.735	0.2865
H2s-Ca		3.0125	3.085	0.2343
H2s-Oa		2.6764	2.690	0.3314
H2s-CH3		3.0761	3.165	0.2829
H1s-Cg		2.6031	2.6100	0.1675
H1s-Og		2.7168	2.735	0.2865
H1s-Ca		3.0125	3.085	0.2343
H1s-Oa		2.6764	2.690	0.3314
H1s-CH3		3.0761	3.165	0.2829

Section II. Excited state calculations of pyrene

The partial charges of excited-state pyrene were calculated by density functional theory with B3LYP functional and cc-pVDZ basis set using the Q-Chem software package. Table B5 presents the partial charges of ground-state pyrene calculated by Q-Chem. Figure B1 is a cartoon of the different types of carbons, corresponding to the symbols in Table B5. Subsequently, Table B6 presents the partial charges of excited-state pyrene calculated by Q-Chem. Figure B2 is a cartoon of the different types of carbons, corresponding to the symbols in Table B6. Q-Chem yielded dipole moments of zero for both ground-state and excited-state pyrene.

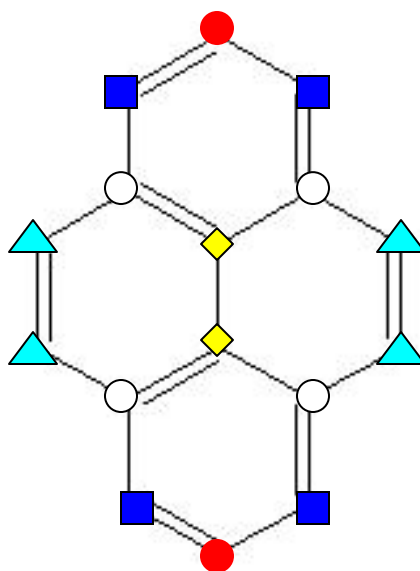







Figure B1. Ground-state pyrene partial charges and number of carbon types from Q-Chem calculations.

Table B5. Results of Q-Chem calculations performed on ground-state pyrene. The first column displays the symbol of the specific carbon atom. The symbols in this table correspond to the symbols in Figure 3-3. The second column presents the name of the specific carbon atom. The third column displays the charges produced by the Q-Chem calculations, while the fourth column presents the charges of the corresponding hydrogen bonded to the specific carbon type.

Symbol	Carbon name	q (e) from Q-Chem	q (e) of the corresponding hydrogen bonded to carbon
	C1s	0.05277	-0.3030
	C2s	-0.000286	-0.04685
	C3s	0.0284	
	C4s	0.0020	-0.04512
	C5s	0.1010	

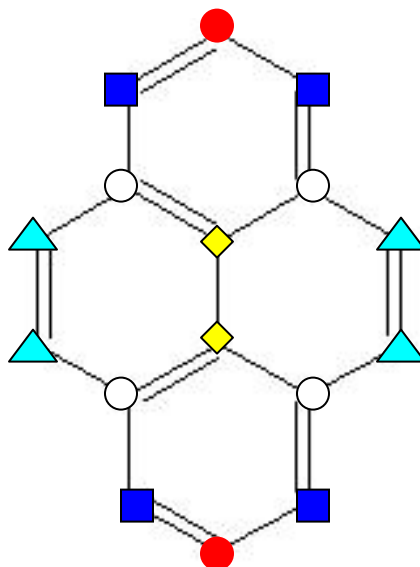


Figure B2. Excited-state pyrene partial charges and number of carbon types from Q-Chem calculations.

Table B6. Results of Q-Chem calculations performed on excited-state pyrene. The first column displays the symbol of the specific carbon atom. The symbols in this table correspond to the symbols in Figure 3-3. The second column presents the name of the specific carbon atom. The third column displays the charges produced by the Q-Chem calculations, while the fourth column presents the charges of the corresponding hydrogen bonded to the specific carbon type.







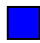



Symbol	Carbon name	q (e) from Q-Chem	q (e) of the corresponding hydrogen bonded to carbon
	C1s	0.05235	-0.3059
	C2s	0.00566	-0.0469
	C3s	0.0247	
	C4s	0.000657	-0.04614
	C5s	0.1021	

Table B7. Partial charges of the carbons in pyrene from Q-Chem calculations, SPARTAN calculations, and OPLS potential.

Symbol	Carbon name	q (e) from Q-Chem	q (e) from SPARTAN	q (e) from OPLS Potential
	C1s	0.05277	-0.122	-0.115
	C2s	-0.000286	-0.226	-0.115
	C3s	0.0284	0.164	0
	C4s	0.0020	-0.195	-0.115
	C5s	0.1010	-0.012	0

VITA

Charu Lata Shukla was born to Vinod and Vindhya-Vasini Pandey in Kitchener-Waterloo, Canada on July 17th, 1979. She grew up in Boca Raton, Florida and graduated from Atlantic High School in May 1997, ranked in the top 10 of her class. She attended the University of Florida on an academic scholarship, where she earned a Bachelors degree in Chemical Engineering with High Honors in December 2001. In May 2002, Charu married Pavan Shukla, her college sweetheart. In August 2002, she proudly joined the Eckert/Liotta research group at the Georgia Institute of Technology with a Georgia Tech Presidential Fellowship.

SELECTED PUBLICATIONS AND PRESENTATIONS

C. L. Shukla, J. P. Hallet, A. V. Popov, R. Hernandez, C. L. Liotta, and C. A. Eckert; "Molecular Dynamics Simulation of the Cybotactic Region in Gas-Expanded Methanol-Carbon Dioxide and Acetone-Carbon Dioxide Mixtures," *J. Phys. Chem. B.* **110**, 24101-24111 (2006).

Charu L. Shukla (speaker), Rigoberto Hernandez, Charles L. Liotta, Charles A. Eckert "Gas-Expanded Liquids: A Synergy of Theory and Experiment." Properties and Phase Equilibria for Product and Process Design Conference Snowbird, UT May 2004.

Charu L. Shukla (speaker), Jason Hallett, Alexander Popov, Rigoberto Hernandez, Charles L. Liotta, Charles A. Eckert. "Computationally Probing the Cybotactic Region in Gas-Expanded Liquids." International Symposium on Supercritical Fluids, Orlando, FL, May 2005.

Charu L. Shukla (speaker), Jason Hallett, Alexander Popov, Rigoberto Hernandez, Charles L. Liotta, Charles A. Eckert. "Molecular Dynamics Simulation of the Cybotactic Region in Gas-expanded Methanol-carbon dioxide and Acetone-carbon dioxide Mixtures." American Chemical Society. Atlanta, GA March 2006.